UNIVERSITÀ DEGLI STUDI DI NAPOLI
FEDERICO II

Dipartimento di Ingegneria Civile, Edile ed Ambientale

A laboratory and field study on cyclic liquefaction of a pyroclastic soil

Valeria Licata

A thesis submitted for the degree of

Ph.D. in Geotechnical Engineering

Napoli, 2015

Supervisors:

Prof. Francesco Silvestri

Prof. Anna d'Onofrio

Prof. Lucio Olivares

Ph.D. Coordinator:

Prof. Claudio Mancuso

To my family...

Acknowledgements

I would like to thank Prof. Francesco Silvestri, who has been more than a mentor during the last years, teaching me the basics of being a researcher and giving me the chance to express my skills and aptitudes autonomously.

A thanks is needed to Prof. Anna d'Onofrio, who, because of her high pragmatism has always been fundamental reference for the resolution of many difficulties who faced with patient and high competence.

I would also like to express my gratitude to Prof. Lucio Olivares who thought me all the secrets of laboratory experimentation, supporting me in any case.

A heartfelt thanks is addressed to Alfredo and Antonio, laboratory technicians and my friends, who have always helped me with all their extreme willingness.

A last, but not least, a special thanks is for all my friends, Filomena de Silva, Silvia Autuori, Mariapia Raucci, Stefania Fabozzi, Ferdinando Aloi, Anna Chiaradonna, Rosario Michele Costigliola, Alfredo Reder, Raffaele Papa, Marianna Pirone, for Francesco because of his lovely presence, for my patient family, for all those laughs and for all the support that have relieved my hardest days. Thank you all.

Table of contents

Introduction

The main objective of the thesis is the analysis of the liquefaction potential of a typical pyroclastic soil, under both cyclic laboratory tests and seismic actions expected during strong-motion earthquakes.

The particular choice of volcanic soils was addressed by the peculiar interest for such soils in the Campania region, widely covered by this kind of materials, which affect significantly the stability of the territory versus both seismic and hydrologic extreme events.

In accordance with previous research studies conducted on the undrained strength of pyroclastic soils under static loads, it was also intended to assess the performance of the analysis tools more commonly used in the engineering practice. The final objective was to evaluate their reliability to predict the liquefaction potential under seismic loads of such soils, taking into account their peculiar lithological features, such as the fragility of the pumice sand particles and the non-plastic ash fine content.

The influence of the above aspects on the liquefaction resistance of such soils was examined by studying both the mechanical behavior of the soil element, by means of an extensive laboratory investigation, and the full-scale problem, tackled with semi-empirical approaches and dynamic analyses applied to a representative case study.

In Chapter II a synthetic review of literature is presented. It is highlighted that, despite the wide availability in literature of studies on cyclic liquefaction of hard-grained sands, the behavior of pyroclastic soil has been seldom studied in the recent years. For such a reason, the Chapter discusses the main constitutive and experimental factors affecting the cyclic resistance of these soils reported in literature insofar. A summary of the analytical procedures traditionally used for the liquefaction assessment in the field is also reported.

Chapter III introduces the 'Riviera di Chiaia' site, which was selected for this study on the basis of a preliminary screening of the potential liquefaction characteristics (according to the Italian Building Code, 2008), and because different kinds of in-situ tests were available for a reliable characterization of the mechanical properties of the soil; this consideration, together with the availability of an open excavation front, suggested to take from this site the undisturbed material used for the laboratory investigation.

Chapter IV describes the intact and reconstituted materials adopted for the laboratory tests, as well as the experimental devices and procedures. In particular, it is described an original technique, especially conceived to assemble frozen reconstituted specimens of different mixtures of coarse-fine fractions, in saturated conditions, on the triaxial device.

Chapter V presents the results of the experimental activity. Preliminarily, the static compressibility and strength of the natural material were characterized by isotropic compression and monotonic triaxial tests. Thereafter, the behavior under cyclic loads was studied by cyclic undrained stress-.controlled triaxial tests. The first test series were carried out to define and compare the cyclic resistance of pumice-ash natural (PAN) and reconstituted (PAR) samples, in order to evaluate the effects of fabric, relative density and effective confining stress. Then, the cyclic resistance of the reconstituted pumice+ash soil (PAR) was compared to that of a material with the same grain size distribution, but prepared with hard-grained silica sand and the same ashy fine content (SAR), in order to evaluate the effects of particle breakage. Finally, the effects of non-plastic ash content were evaluated by comparing the cyclic resistance of the reconstituted pumice+ash soil with that of a pumice-clay mixture (PCR), once again with the same grading, for which the ashy fine fraction was substituted by a low-plasticity clay.

In Chapter VI, the liquefaction assessment of the test site was evaluated on the basis of the well-known semi-empirical approaches proposed by literature. The main issues regarding the different possible choices of the reference magnitude and acceleration amplitude defining the seismic demand, as well as the evaluation of the cyclic

resistance of soils, are discussed; an up-to-date approach to define the probabilistic seismic hazard on-purpose for liquefaction assessment is also formulated and tested on the specific case study.

Chapter VII describes the results of one-dimensional seismic response analyses performed by means of both a decoupled and a coupled approaches, in the latter case by adopting a simplified model for predicting the pore pressure build-up. The cyclic stress ratios resulting from the dynamic analyses were used to assess the liquefaction potential of the site, by using both the semi-empirical charts and the laboratory cyclic resistance curve of the undisturbed samples. The different predictions are finally compared and critically discussed.

State of the art

II.1 Introduction

The study of saturated sandy soil under undrained condition is still a matter of controversy and embraces many aspects.

First of all, there is the difficulty to correctly understand the effects of the parameters ruling the undrained behavior of saturated sands, i. e.:

- 'State factors' (effective confining stress, void ratio, etc.);
- 'Constitutive factors' (fine content, plasticity of fine content, particles fragility, structure, etc.).

Moreover, the undrained behavior has always been studied separately under different kind of loads (i.e. as liquefaction is reached under monotonic or cyclic loads). Recent literature contributions (Hyodo et al., 1998; Baki et al., 2012) are trying to link cyclic and static instability.

In this framework, pyroclastic/volcanic sands occupy a transversal position because of their structural peculiarities, such as non plastic fine content and fragility particles, which leads to revisit the consolidated theories about liquefaction. Several issues arise about the applicability of instruments commonly used in the practice to assess the liquefaction potential.

The main literature findings about the undrained behavior of saturated sandy soils under cyclic loadings, more relevant for the pyroclastic/volcanic sands, and the commonly adopted instruments for the assessment of liquefaction potential are briefly introduced in the following sections

.

II.2 'State' factors

The early studies on clean saturated hard-grained sands provided a set of possible effective stress paths for undrained shear tests that describes the behavior of soil under different density conditions (see Figure II.1) in the frame of the Critical (Steady) State Theory.

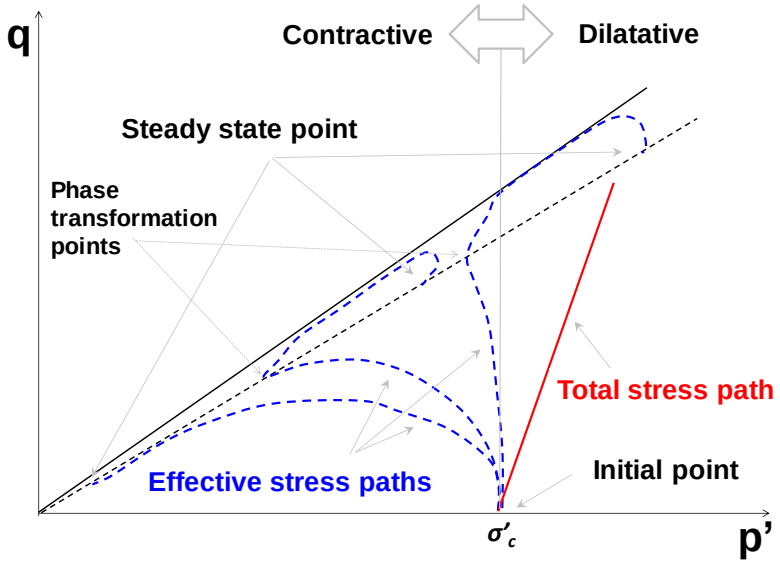

FIGURE II.1: IDEALIZED STRESS PATHS FOR UNDRAINED SHEAR TESTS (HYODO ET AL. 1998).

In the chart of Figure II.1, the behavior of loose sands, typically defined contractive (unstable), is shown by the lowest effective stress path which migrates to the far left of the diagram achieving the steady-state conditions (Castro, 1975; Castro & Poulos, 1977; Vaid & Chern, 1985; Poulos et al., 1985; Vaid et al., 1989). In this case, this softening path is justified by the tendency of soil to reduce its volume that, in undrained conditions, induces a positive increment of pore pressure and, after instability, a decreasing of the mean effective stress, p'.

The central effective stress path is associated to a partially unstable behavior with an initial contractive behavior (characterized by positive excess pore pressure). Then the path passes through a "phase transformation" (Ishihara et al., 1975) corresponding to a state of stress and dilates to a steady-state where pore pressure begins to

decrease as deviator stress increases. As shown by the effective stress paths, the behavior becomes hardening and dilatative as the soil is denser and denser.

Under cyclic loading the soil response (unstable or stable) is similar. In fact, loose sands develop positive excess pore pressure, triggering liquefaction while dense sands behave triggering cyclic mobility (Castro 1975, Castro & Poulos 1977).

Been & Jefferies (1986) put in light another aspect ruling the undrained behavior of sand that was related to the combination of void ratio, *e*, with the effective confining stress, *p'*. According to the Authors, effective confining stress may modify the behavior of soil so that dense sand may behave as loose sand. The combination of *e* and *p'* was taken into account by means of the so-called 'state parameter', ψ, defined as the difference, at a constant *p'*, between the current and the critical void ratio (*e**). In other words, ψ provides the current state of soil respect to the projection of critical (or steady) state line: a positive ψ describes an unstable behavior, otherwise, a dilatative and stable behavior.

Studies on pyroclastic soils approached by state parameters, ψ, under cyclic loading conditions are not exhaustive; the influence of relative density or/and the confining effective pressure are basically taken into account by separated interpretations.

Hyodo et al. (1998), firstly, studied the effect of density and effective confining pressure on a well-graded volcanic sand, Shirasu, by means of the results of undrained monotonic and cyclic triaxial tests. The elaboration of cyclic tests is shown in Figure II.2a and Figure II.2b in terms of cyclic stress ratio ($CSR=q/2\sigma'_c$) and number of cycles required to achieve liquefaction (N_{cyc}). The cyclic strength of loose Shirasu increases with increasing confining pressure (Figure II.2a). In the case of dense Shirasu, it was noticed an opposite trend for which the higher is the confining pressure, the greater is the reduction of cyclic resistance (Figure II.2b).

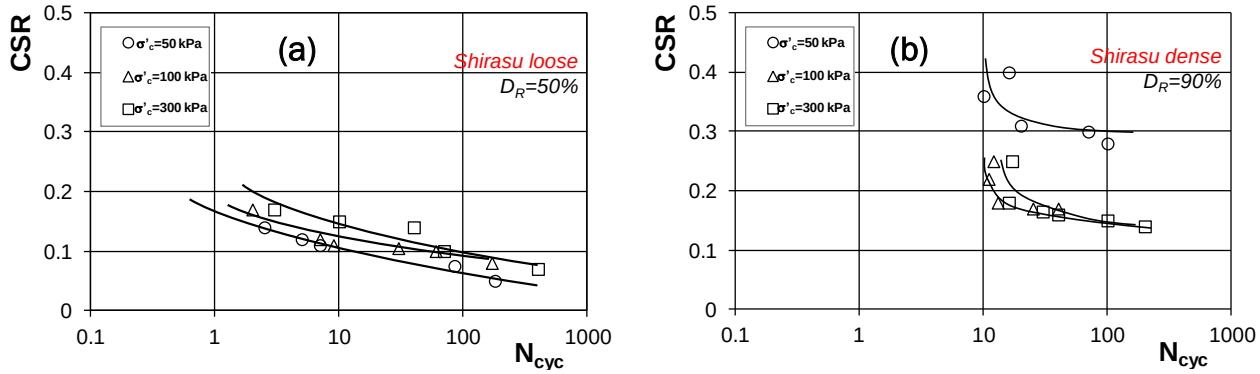

FIGURE II.2: CYCLIC STRENGTH CURVES FOR A DOUBLE-STRAIN AMPLITUDE ε_A= 5%, FOR SHIRASU SAND (HYODO ET AL. 1998).

Density and confining pressure were considered, more recently, by Orense & Pender (2013) performing cyclic triaxial tests on clean pumice sands. The results reported in terms of cyclic resistance curves are shown in Figure II.3a, for both loose (D_r=25%) and dense (D_r=70%) pumice specimens. Despite of the findings of Hyodo et al. (1998), relative density appears to be not as remarkable for clean pumices.

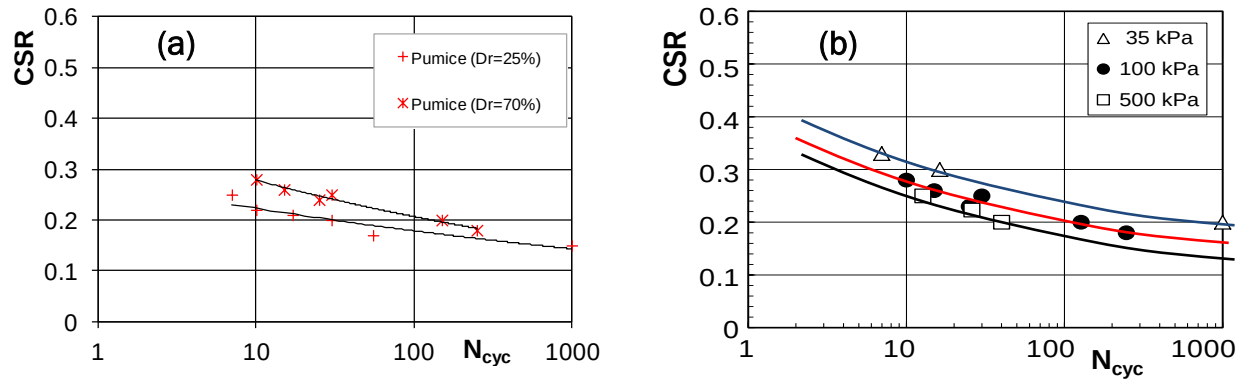

FIGURE II.3: CYCLIC STRENGTH CURVES FOR A DOUBLE-STRAIN AMPLITUDE ε_A= 5%, FOR PUMICE SAND (ORENSE & PENDER, 2013).

In Figure II.3b the influence of effective confining pressure on the liquefaction resistance was investigated by applying three different levels of effective confining pressure, σ_c'=35, 100 and 500kPa under different levels of cyclic shear stress ratio. The cyclic resistance curves in Figure II.3b highlight the confining pressure dependency of liquefaction resistance for reconstituted pumice; in fact, liquefaction resistance increases as the confining pressure decreases.

In conclusion, the liquefaction resistance of volcanic sands seems to show a markedly dependence on the effective confining pressure applied during the test. On the contrary, the role of density is still not so clear.

II.3 'Constitutive' factors

Though literature provides wide studies on the effect of non plastic fine content on liquefaction resistance, there is no clear consensus on the role of silt on the undrained behavior of sands. The results of these studies indicate that increasing the non-plastic fines content in a sand either increases the liquefaction resistance of the sand, decreases the liquefaction resistance of the sand, or decreases the liquefaction resistance until some limiting fines content is reached, and then increases its resistance (Polito, 1999).

Uncertainties related to role of non plastic fine content are partially justified by the adoption of different analysis approaches which were based on field studies as well as on laboratory experimentation.

According to field studies, on one side, soils with greater non plastic fines contents are less prone to liquefy during a seismic event (Fei, 1991; Okashi, 1970). On the other side, opposing findings were carried out by Verdugo (1985), Kaufman (1982) for which soils with higher silt contents are more likely to liquefy than sands with lower silt contents.

The contradictions associated to the field-based studies are also observed in findings based on laboratory tests for which, whether percentage of fine is considered, cyclic resistance may increase nearly linearly with silty fine content (Chang et al. 1982; Dezfulian, 1982), or may decrease as much as 60% from their clean sand values for an increase in silt content of 30% (Tronsco and Verdugo, 1985).

For pyroclastic sand, the silt content seems to affect, in conjunction with the effective confining pressure applied, the occurrence of crushing of sandy particles which, in turn, may inhibit the effect of relative density on liquefaction resistance because the

cyclic shearing and the associated particle breakage resulted in stable soil structure for both dense and loose sands (Orense & Pender, 2013).

This latter aspect was encountered by Orense & Pender (2013) work in which it was noted that under the confining pressures considered in their study, clean pumices undergo remarkable particle crushing when subjected to the cyclic shear. The development of the particle crushing during a cyclic loading was elucidated by a series of tests ad hoc, performed on virgin pumices with a known grain size distribution, terminated after a specified number of cycles. In order to evaluate the particle crushing occurred, it was estimated the surface area, S_a, of the particles by a method originally proposed by Miura and Yamanouchi (1971), reported in Figure II.4, against the N_{cyc}. In Figure II.4, it was observed that the degree of particle crushing increased with the amplitude of applied CSR.

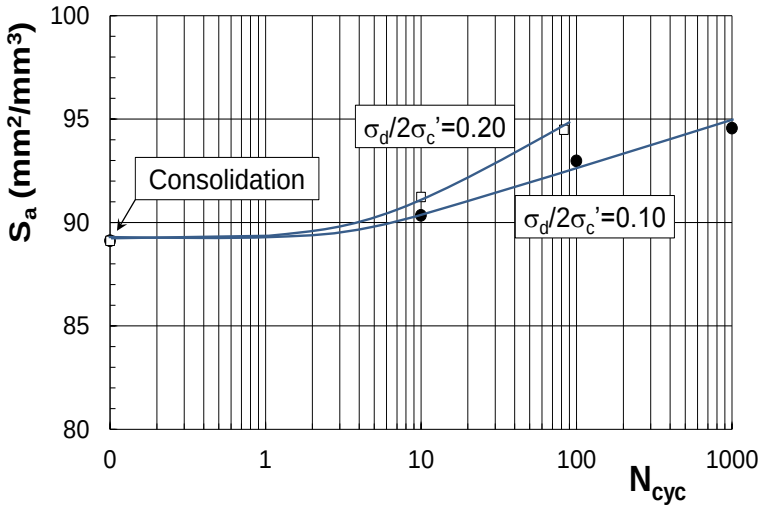

FIGURE II.4: RELATIONSHIPS BETWEEN SPECIFIC SURFACE AREA AND NUMBER OF CYCLES DURING CYCLIC UNDRAINED TESTS (ORENSE & PENDER, 2013).

Another case study, in which the effects of fragility particles and texture were taken over as a contributory cause to trigger liquefaction and to affect relative density and effective confining stress, was presented by Suzuki & Yamamoto (2004). The Authors performed a set of cyclic triaxial tests, once again, on undisturbed and disturbed volcanic sand Shirasu, that liquefied during Kagoshimen earthquake and

subsequently re-liquefied because of an aftershock, in order to analyze the liquefaction and 're-liquefaction' features of sand. Comparing cyclic resistance curves, the first liquefaction strength of the undisturbed shows a higher value than that of the disturbed sample, independently of the initial effective confining stress, but lower value of its re-liquefaction strength because of loss of bonding formed between soil particles. The authors also noted that both the change in void ratio of the undisturbed sample after the first liquefaction was bigger than that of the disturbed sample and, in addition, the change in fine content of both samples due to the crushability depending on the initial confining stress.

Shirasu sand was also studied in another work of Hyodo et al. (2002) to evaluate the combined effect of non-plastic fine and crushability on its liquefaction features. Cyclic triaxial tests were performed on reconstituted specimen of volcanic sand with and without 30% of non plastic fine, at the same relative density, in a range of confining effective pressure of σ'c=50-100-300kpa. The cyclic strength increases with increasing confining pressure for Shirasu containing fine while for the no fines material, the cyclic strength increased marginally as the confining pressure was increased from 50kPa to 100kPa and at 300kPa the cyclic resistance curves became much flatter. Crushing occurred in both cases, but it was not clear if it had affected the cyclic strength of sand with and without fine.

II.4 Methodologies for liquefaction assessment

The objective of analysis to assess liquefaction potential is to evaluate if the expected seismic action is compatible with the required performance level of the facility of interest which, in turn, is a function of its importance. In principle, the structures characterized by a higher performance grade should be studied using more sophisticated methods. Less sophisticated methods may be allowed for preliminary design, screening purposes or response analysis for low levels of excitation.

A variety of analysis methods are available for evaluating the liquefaction potential. These methods can be broadly classified on the basis of their level of sophistication and capability, into the three levels illustrated in Table II.1.

TABLE II.1: LEVELS OF ANALYSIS FOR LIQUEFACTION ASSESSMENT (MODIFIED BY SILVESTRI & D'ONOFRIO, 2014)

Level	*Analysis*	*Constitutive law*	*Computation*	*Assessment*
I	**Semi-empirical**	Basic (rigid-plastic)	Pseudo-static analysis	Action vs Strength
II	**Simplified dynamic**	Simplified (visco-elastic,elasto-plastic)	Dynamic analysis with simplified geometry	Stresses, strains, pore pressures
III	**Advanced dynamic**	Complex (elasto-plastic with hardening)	Dynamic analysis with complex geometry	Effective stress distributions, pore pressure, strains and residual displacements. Evaluation of failure mechanism of the system

Semi-empirical methods provide a simplified and expeditious tool to assess liquefaction potential, being founded on a pseudo static stress-based analysis, synthesizing the fundamental aspects of dynamic site response and soil resistance.

The forerunners Seed & Idriss (1971) built the basis of such simplified methods, by simply comparing the seismic demand with the soil capacity observed in liquefaction/no-liquefaction case histories.

In the original procedure, the seismic action was defined in terms of cyclic stress ratio (CSR), inferred from the equilibrium of inertial forces and shear stresses associated to the propagation of accelerograms in a deformable soil column (see Figure II.5).

The initial formulation of CSR pertained to the equivalent uniform shear stress generated by an earthquake having a moment magnitude M_w=7.5; this hypothesis was a restriction for the practical application so that, in the following updates of the

procedure, the expression of CSR was modified by means of the so-called 'magnitude scaling factor' (MSF), in order to apply it to any value of magnitude. The complete expression of CSR is the following:

$$CSR = 0.65 \frac{\sigma_v}{\sigma_v'} r_d \frac{1}{MSF} a_{max} \quad \text{(II.1)}$$

where:

- a_{max} is the maximum acceleration, expressed in g;
- r_d is a parameter describing the ratio of peak shear stress for a flexible soil column to that pertaining to a rigid soil column (as illustrated in Figure II.5); different analytical formulations were suggested by different Authors (Iwasaki et al., 1978; Liao e Whitman, 1986; Seed & Idriss, 1971; Idris and Boulanger, 2004) performing parametric site response analyses and expressing r_d as a function of depth and earthquake magnitude;
- 0.65 takes into account the irregularity of the earthquake motion, by taking a reduced peak amplitude as an equivalent static load.

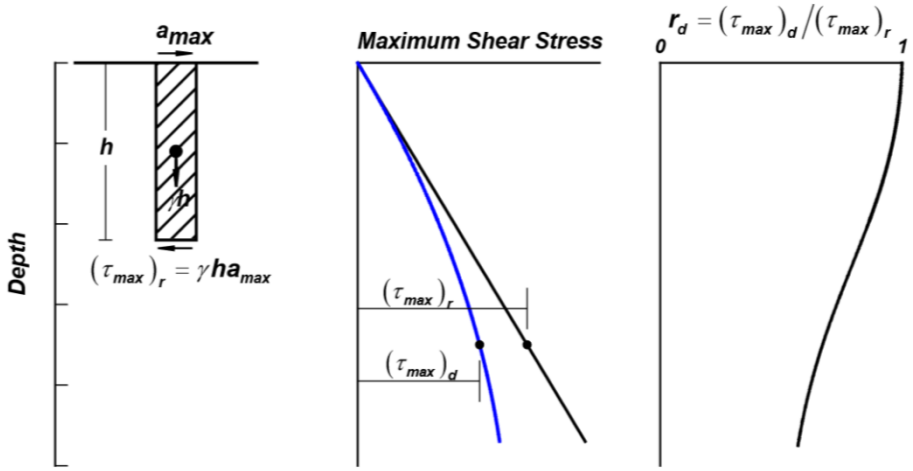

FIGURE II.5: SCHEMATIC REPRESENTATION FOR DETERMINING MAXIMUM SHEAR STRESS, τ_{MAX}, AND THE STRESS REDUCTION COEFFICIENT, R_D.

Capacity of soil was meant in terms of cyclic resistance ratio (CRR) and was inferred from the results of Standard Penetration Tests (SPT), inherently accounting for the effects of soil density and effective confining stress. Consequently, Seed et al (1975a) included the normalization of penetration resistances in sand to an

equivalent σ'_v of one atmosphere (98.1kPa), in order to obtain quantities that are independent of σ'_v and thus more univocally related to the sand relative density, D_R.

The disadvantages related of using SPT are that it provides a non-continuous record of the penetration resistance and is more vulnerable to operator error. That's why CRR was also obtained by Cone Penetration Test (CPT), which has proven to be a valuable tool in characterizing subsurface conditions and in assessing various soil properties, including estimating the potential for liquefaction at a particular site.

The first liquefaction correlation based directly on CPT case histories was proposed by Zhou (1980) using observations from the 1978 Tangshan earthquake. Recent years have seen a flowering of CPT-based correlations (e.g., Shibata and Teparaksa 1988; Stark and Olson 1995; Suzuki et al 1997; Robertson and Wride 1997; Olsen 1997; Seed et al 2003).

A further interpretation of resistance of soil, adopting shear wave velocity, V_s, was provided by Andrus & Stokoe (2000 and 2003) using case history data from 26 earthquakes and more than 70 measurements sites in soils ranging from fine sand to sandy gravel to profiles including silty clay layers. The main advantage of using V_s measurements is that it is inferred from non-destructive tests which do not affect the state of soil and can be particularly useful for sites underlain by difficulties to penetrate or sample soils (e.g., gravels, cobbles, boulders).

Time after time,the expanding data-base for field case histories has produced many updates to the original procedure by Seed & Idriss (1971). Such experiments lead to new proposals for the evaluation of both CRR and parameters for determining CSR, capturing the essential physics while being as simplified as possible. These updated relations were used in re-evaluations of the field case histories to derive mainly revised deterministic SPT-based and CPT-based liquefaction correlations. In the comprehensive state of the art by Idriss & Boulanger (2004), new formulations for r_d and MSF were provided. In addition, the determination of CRR by SPT and CPT was enriched by means of K_σ and K_α coefficients which consider, respectively, the combined effects of D_R, σ'_v and particle breakage, as well as the presence of static driving shear stresses such as those existing beneath slopes.

In conclusion, semi-empirical methods provide a reliable tool, especially when SPT, CPT and Vs based approaches are used in conjunction for liquefaction potential assessment. The question that arises, however, is which methodology should be given greater weight when parallel analyses by SPT, CPT, and/or V_s procedures produce contradictory results; the case study presented in this thesis will be paradigmatic in such sense, especially for the uncertainties related to the effects of partial breakage and fine content.

Approaches based on dynamic analysis use basically the entire time history of acceleration, taking into account the effect of frequency content, duration and variability of shaking amplitude. The differences between a simplified or an advanced dynamic analysis is related to the adoption, in the latter, of sophisticated models to correctly describe the multiphase nature of soil and the evolution of mechanical properties due to the pore pressure build-up. Such an aspect for pyroclastic soils, as described before, is ruled by numerous factors such as density, current mean principal effective stress, fabric, shearing mode and particle crushing, that, in principle, should be taken in conjunction into account in the implemented constitutive laws.

Two main ways can be adopted for studying the stability of saturated soil deposits subjected to earthquake loading, i.e. the total stress and the effective stress approaches. Several equivalent linear and non-linear numerical models have been proposed to predict the undrained cyclic behavior of soil and consequently the generation of the pore water pressure.

Since soils exhibit a wide range of complex responses when subjected to an arbitrary loading, the most completed method is non-linear stress-strain response analysis, where excess pore water pressure produced during shaking can be calculated from the corresponding volume change tendency of dry soils (e.g. Martin et al.1975).

For engineering practice, since complex approaches imply the correct definitions of a great number of parameters implemented in the plasticity-based models and a significant computational burden, simplified approaches for pore water pressure generation based on the results of cyclic laboratory tests are presented in literature

(Hardin and Drnevitch, 1970; Seed & Idriss, 1970; Seed et al. 1976; Sun et al. 1988; Vucetic and Dobry, 1991).

It was demonstrated that the aforementioned approaches provide results that are well compared with field measurements; on the other hand, the application of these simplified models for the prediction of pore pressures is not so expeditious. In fact, it is preliminarily needed to convert the irregular earthquake load history into an equivalent number of cycles of uniform shear stress amplitude in order to produce the same pore pressure build-up expected at the site.

In literature, a wide range of conversion procedures is provided (Seed et al., 1975; Annaki & Lee, 1977; Biondi, 2002; Green & Terri, 2005) but their application is rather complex and makes the results strictly dependent on the adopted conversion curve and on the techniques for choosing and counting the stress cycles that significantly affect the pore pressure build-up (Biondi et al., 2012).

To bypass such conversion procedures, recent works presented by Park et al. (2014) and Chiaradonna et al. (2015) provided a straightforward tool for the evaluation of generation of pore water pressure. This latter uses a stress-based method adopting a single variable, called 'damage parameter', κ, which can be computed for both cyclic test data and irregular stress histories with both total and effective stress approaches. This latter, in particular, was adopted in the dynamic analysis and reported in Chapter VII in the present work.

Case study: Riviera di Chiaia

III.1 Riviera di Chiaia site

The distribution of the liquefaction potential index, IL, reported in Figure III.1a, shows that the Neapolitan costal area is characterized by a medium-high susceptibility to liquefaction.

In this area the 6th subway line is under construction with the excavation of San Pasquale station shaft located along the 'Riviera di Chiaia' (Figure III.1b). This site was then selected to carry out a detailed liquefaction susceptibility analysis.

In following paragraphs, a brief description of the site geologic characteristics and a synthesis of the available geotechnical in situ tests results are presented.

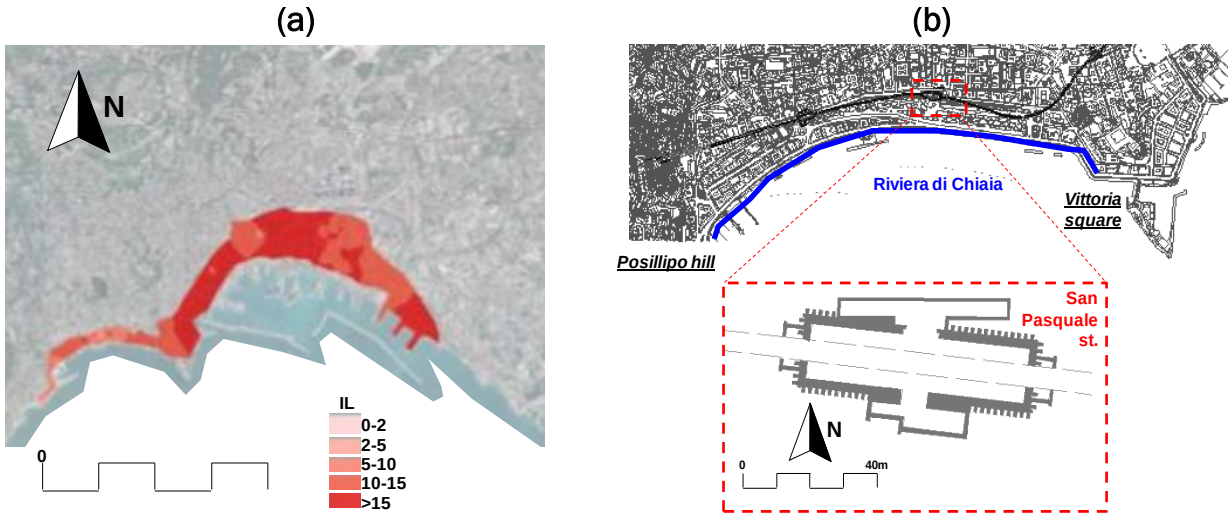

FIGURE III.1: (A) LIQUEFACTION INDEX OF URBAN AREA OF NAPLES (EVANGELISTA L., 2006); (B) SAN PASQUALE STATION AREA.

III.1.1 Geologic frame

Naples arises in the centre of a volcanic region composed by two volcanic districts: the Somma-Vesuvius crater and the Phlegraean fields. These two volcanic districts are the main responsible for the genesis of Neapolitan subsoil. In particular, the Neapolitan coast is covered by pyroclastic soils mainly produced by Phlegraean fields activity.

Phlegraean fields caldera, located in the west side of Naples, is the product of different collapses associated to explosive eruptions. The volcanism of Phlegraean fields started about 50000 years ago (Rosi & Sbrana, 1987). The study of stratigraphic data and literature allowed a detailed reconstruction of the volcanic activity of this crater characterized by two great reference events: 'Ignimbrite Campana' (39ky) and 'Neapolitan yellow tuff' (12ky) eruptions. The Ignimbrite Campana formed the external and biggest caldera fence while the more recent Neapolitan yellow tuff activity gave rise to the smaller caldera (Figure III.1).

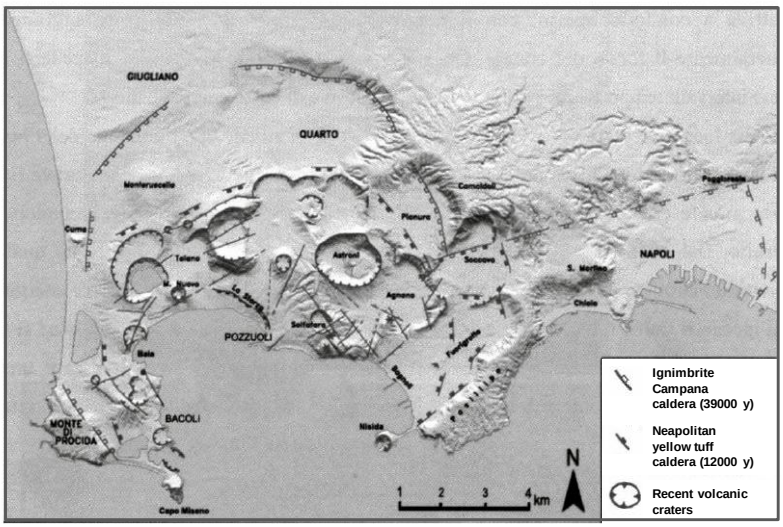

FIGURE. III.2: PHLEGRAEAN FIELDS CRATERS.

Therefore the geology originated from Phlegraean fields activity can be reconstructed in the following sequence:

- Deposits preceding the Ignimbrite Campana eruption;
- Deposits produced by the Ignimbrite Campana eruption;

- Deposits subsequent the Ignimbrite Campana and preceding the Neapolitan yellow tuff eruption;
- Deposits produced by the Neapolitan yellow tuff eruption;
- Deposits subsequent the Neapolitan yellow tuff eruption.

The volcanic activity subsequent the Ignimbrite eruption was essentially effusive; after the Neapolitan yellow tuff eruption the volcanism was mostly characterized by explosive events and by marine ingressions due to the uplift and lowering of the Phlegraean caldera.

The effusive activity between the two main eruptions mainly produced 'surge' and 'flow' deposits having a loose or lithified texture. The diagenesis of these pyroclastic materials is strictly connected to the type of volcanic activity; in particular, the lithified soils were not generated by environmental conditions (weight of overlying materials, effect of water, etc.), but by metamorphic phenomena due to the temperature and the gas content of materials during the depositional processes (Nicotera, 1998).

The Neapolitan yellow Tuff can be considered the main bedrock formation. It is somewhere outcropping within the urban area of Naples or it can be retrieved at different depth. The incoherent *facies* of the yellow tuff, named '*pozzolana*', cover the bedrock and is widely diffused in all the urban territory with thickness some tens of meters. It underlies alternating thin layers of a younger formation of sands, pumices and lapilli, covered by volcanic fly ashes and remoulded soils, together with manmade grounds, including masonry blocks often used as filling materials. Along the costal zones of Naples the stratigraphic sequences is characterized by a succession of volcanic and seashore products due to the uplift and the lowering of the Phlegrean caldera. In this area the pozzolanic soil appears as remoulded, removed and re-sedimented as alluvial soil, while in the hilly part of the city pyroclastic soil spread on site.

A schematic geologic section of the Riviera di Chiaia is reported in figure Figure III.3: the tufaceous bedrock produced by Neapolitan yellow tuff eruption underlies an incoherent layer of the same material (Pozzolana), above which pumiceus and ashy

soils alternate, seashore deposits due to the marine ingression related to the caldera movements lie above the pyroclastic sequence. Its maximum depth of about 20m under the sea level highlights that Chiaia coast underwent only few tens meters subsidence.

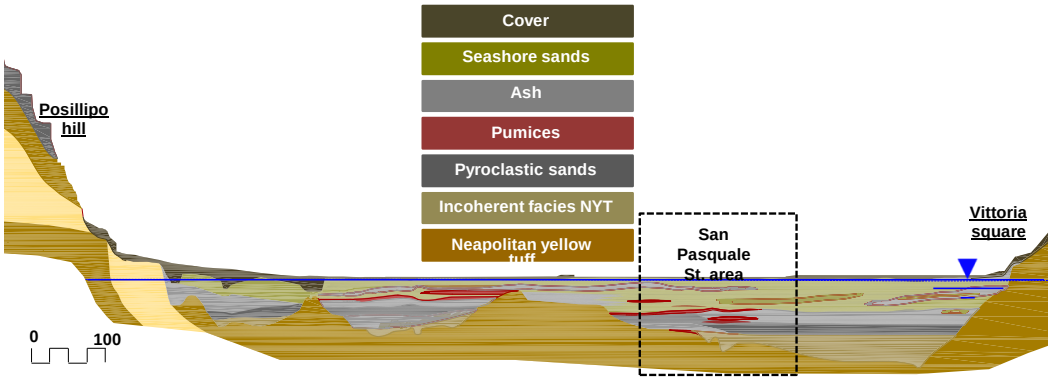

FIGURE III.3: 'RIVIERA DI CHIAIA' GEOLOGIC SECTION.

III.2 Available site characterization

Before the excavation of shaft station started, there were available in situ data coming from two surveys campaigns aimed at characterizing the bedrock morphology, the groundwater level and the geotechnical properties of the shallow deposits. The in situ tests carried out during the design of the station shaft are listed in Table III.1, while their location is reported in Figure III.4.

TABLE III.1: RIVIERA DI CHIAIA IN SITU TESTS.

Boreholes	# 1 – Continuous coring # 4 – Destructives drilling
Penetration tests	# 4 - Cone Penetration test (CPT) # 8 - Standard Penetration tests (SPT)
Vs measurement tests	# 2 - Seismic dilatometer (SDMT) # 1 - Cross hole (CH)
Permeability test	Lugeon test

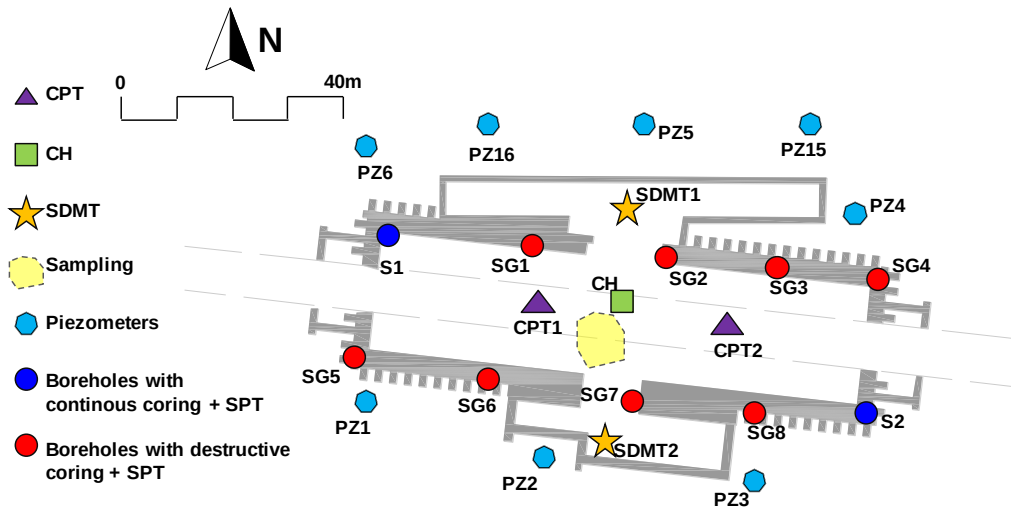

FIGURE.III.4: BOREHOLES AND SURVEYS.

III.2.1 Stratigraphy

Two boreholes with continuous coring (S1 and S2) and 8 destructive drillings (SG1-SG4, SG5-SG8) were executed. In particular, S1 and S2 boreholes were located in two corners of the station shaft, while the SG1-SG8 boreholes were drilled along two parallel lineups of the station in the SW/NE direction, with the aim of defining the bedrock depth in the area of the station shaft.

The stratigraphic sequence obtained from the boreholes is reported in Figure III.5 and it confirms the depositional sequence and the geologic history of the site described before: the deposit is characterized by sub-horizontal volcanic and seashore layers above a sub-horizontal tufaceous bedrock. In details, starting from the top surface, few negligible centimeters of man-made ground cover about 11m of seashore sands (SS) that lie upon 15m of volcanic products, divided into ashy silt sand (AS1-AS2) and pyroclastic sand (PYR). Beneath these latter, a layer of "pozzolana" (IF) about 15 m thick can be found, which is an incoherent *facies* of Neapolitan Yellow Tuff that is found at the depth of about 38m.

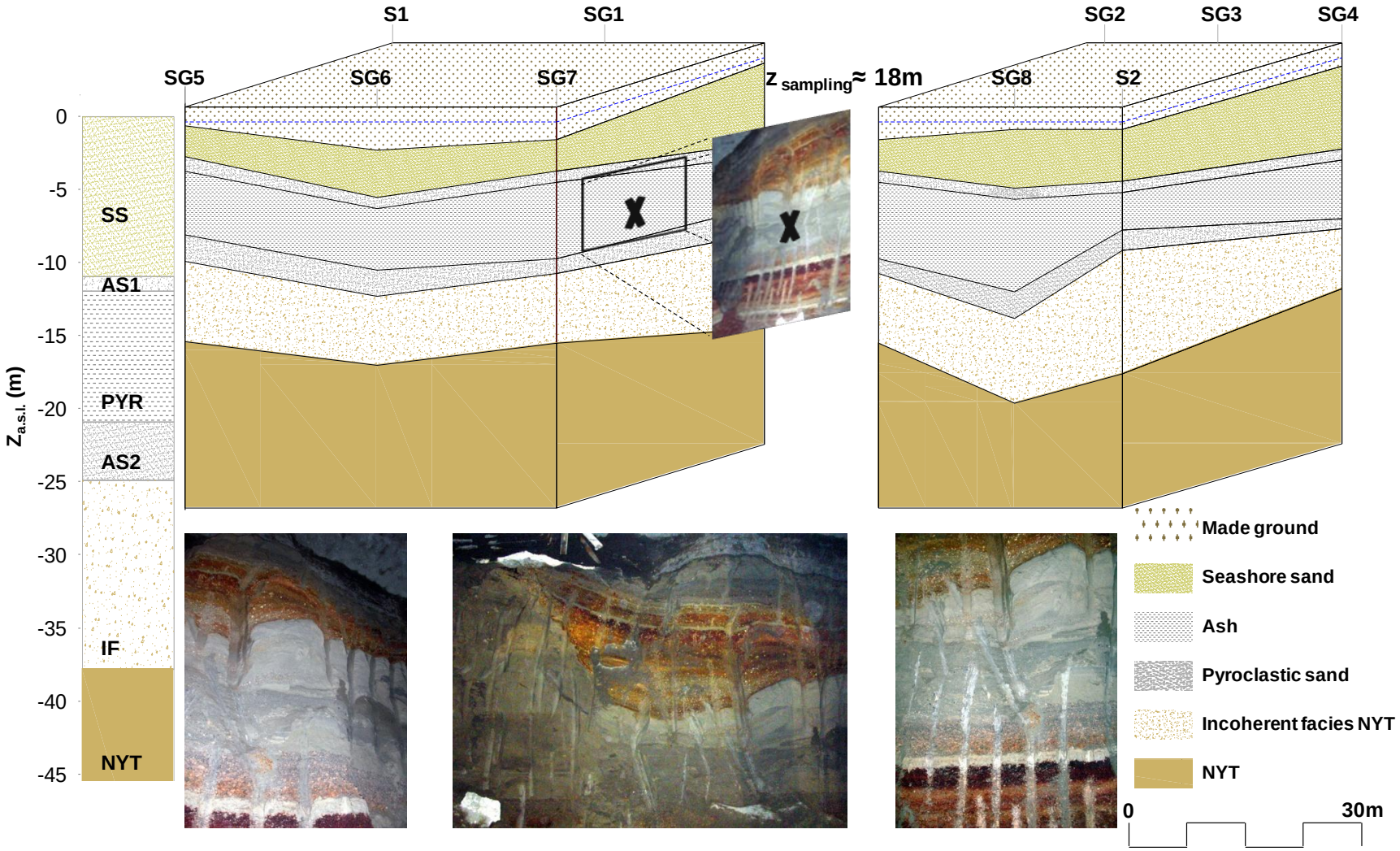

FIGURE III.5: STRATIGRAPHIC SECTION OF RIVIERA DI CHIAIA

III.2.2 Groundwater table

Before starting the excavation eight piezometers were installed to monitor the seasonal excursion of groundwater table and its variation during the excavation phase. Figure III.6 illustrates the collected data in terms of groundwater level varying with time, within a period of about four years. Neither appreciable variations, nor marked cyclicality, could be appreciated during monitoring, as the groundwater level remains stable approximately at the ground level.

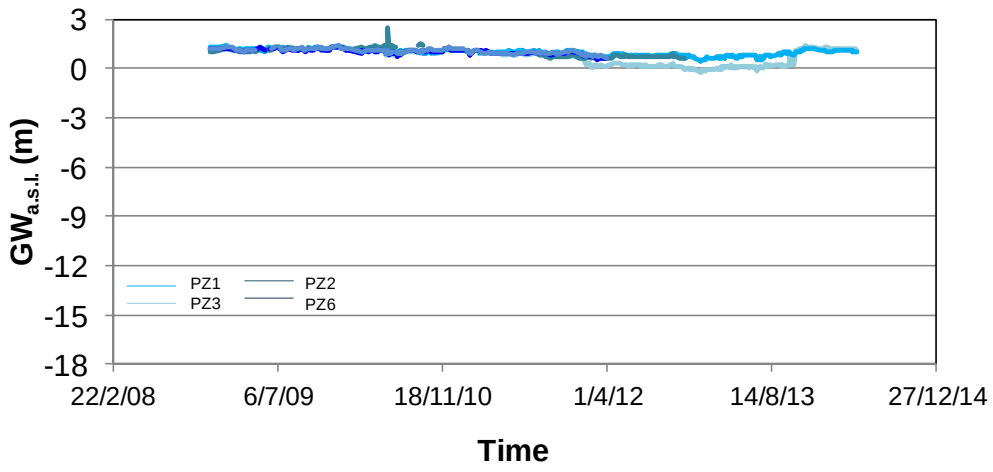

FIGURE. III.6: GROUNDWATER LEVEL EXCURSION

III.2.3 In situ tests

Standard penetration tests (SPT) were carried out at different depth in all the boreholes, together with two cone penetration tests (CPT). Shear wave velocity measurements, Vs, were also undertaken by a cross-hole test (CH) carried out within the area of the shaft. Furthermore, two seismic dilatometer test (SDMT), located outside the excavation area, were executed.

III.2.3.1 Penetrometric tests

The results of CPT and SPT tests are reported in Figure III.7 in terms of cone tip resistance, q_c, (Figure III.7a) and number of blow counts, N_{SPT}, (Figure III.7b) varying with depth, z.

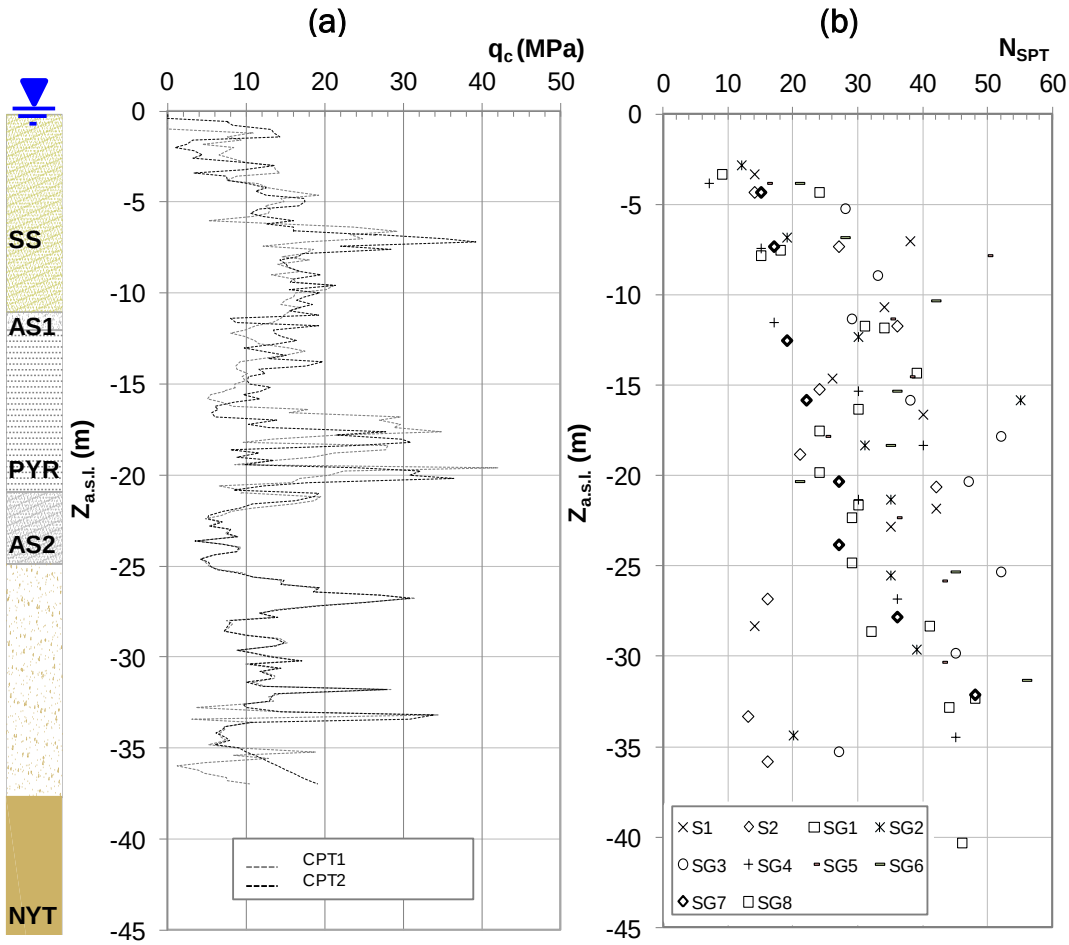

FIGURE. III.7: CONE PENETRATION TESTS (A) AND STANDARD PENETRATION TESTS (B) RESULTS.

There is a good agreement between the results of the two CPT tests: the cone resistance increases in the first 10m (seashore sandy layer) and remains approximately constant, independently from the confining pressure, in the pyroclastic layers (Figure III.7a). This trend may be related to the underestimation of cone resistance in the pyroclastic soil due to the soil particles breakage (Rippa & Vinale, 1983). Moreover, Figure III.7b shows the N_{SPT} profiles: a significant scatter can be observed, partially ascribable to the stratigraphic variability within the station shaft.

III.2.3.2 V_s measurements tests

Shear wave velocity, V_s, tests, measured by Cross Hole and Seismic dilatometer, are shown in Figure III.8a, while the corresponding initial shear modulus, G_0, profile is

plotted in Figure III8b. There is a quite good agreement between the different V_s profiles, even if in the first 15m the Vs values from SDMT are on average slightly higher than those obtained by the CH. The little difference may be referred to a local effect due to the different test execution: in fact, with SDMT, the soil is locally displaced (and compressed) by the dilatometer, while in the CH, the soil expands after drilling the holes.

The shear wave velocity is quite constant around 200 m/s in the first 15m depth, increasing in the following 5m in the pyroclastic layer up to 400 m/s. The CH profile shows a slight inversion of Vs in the ashy layer (ASH2) and the incoherent facies (IF) that keeps constant with depth at around 350 m/s and increases at the bottom of the deposit to reach almost 1000 m/s at the top of the underlying tuff.

The initial shear modulus, G_0, was obtained processing the shear wave velocity results. Because of the previously mentioned differences, the values of G_0 from SDMT are locally slightly higher than those obtained by cross-hole.

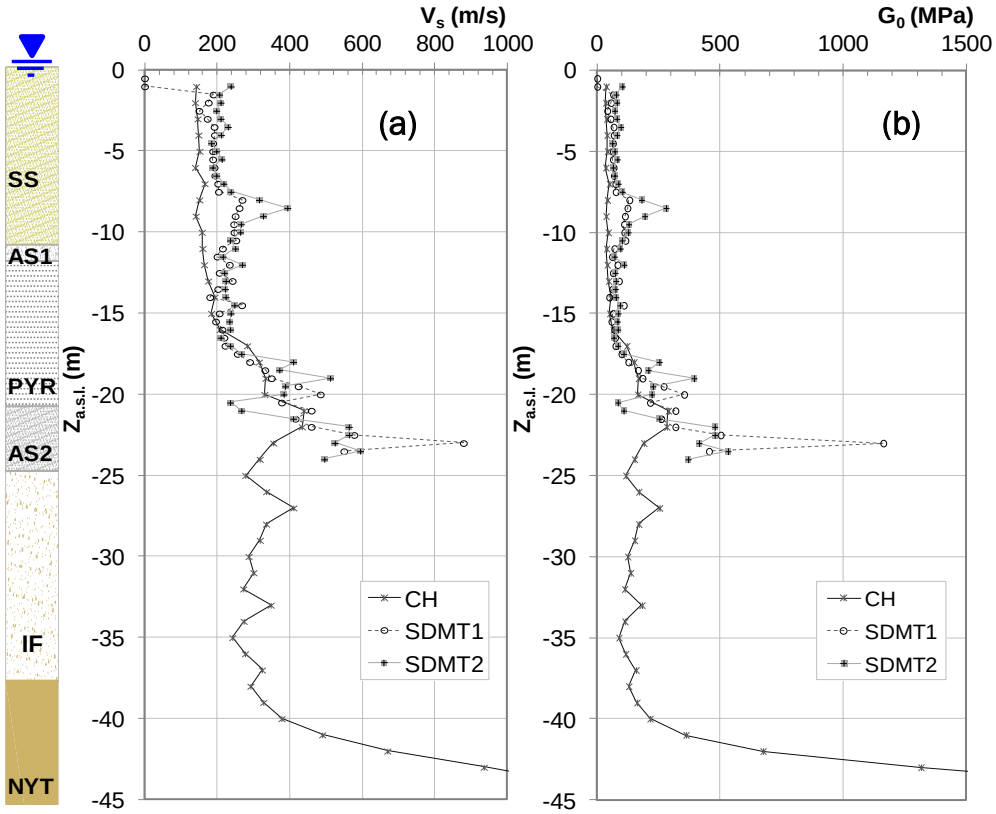

FIGURE III.8: CROSS HOLE (A) AND SEISMIC DILATOMETER (B) RESULTS.

III.2.4 In situ stress- state and strength soils properties

In situ tests results, reported in the previous paragraphs, were interpreted by L'amante et al. 2012 who provided a preliminary evaluation of some parameters of interest.

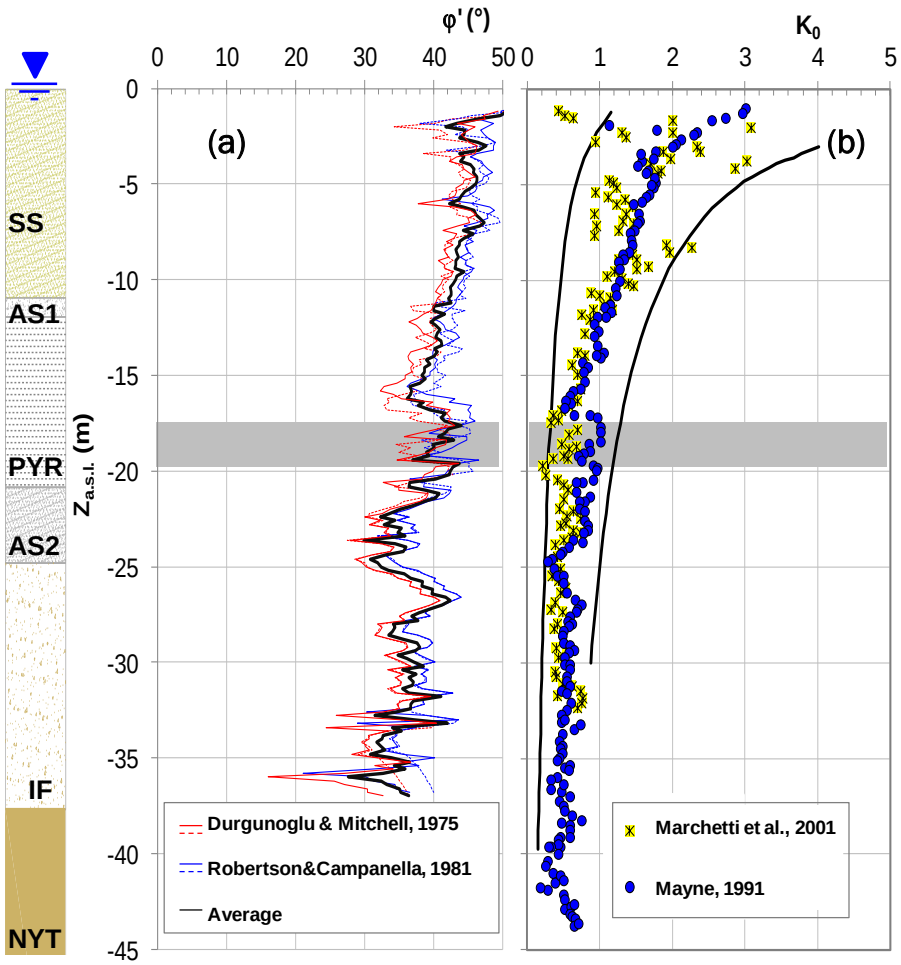

FIGURE III.9: EVALUATION OF SOIL PROPERTIES.

The results of CPT and SDMT were interpreted by L'amante et al (2012) to obtain the vertical profile of the coefficient of earth pressure at rest, k_0, that, in turn, allows the definition of the in situ stress state. To this aim they interpret the CPT data adopting the correlation suggested by Mayne, 1991. The OCR values requested in the expression was preliminary evaluated adopting the correlation suggested by Mayne and Kulhawy, 1982. The same data were also adopted for an alternative estimate of k_0 (Marchetti et al. 2001). The two determinations are reported in Figure III.9b: k_0

values deduced by CPT are on average slightly higher than those based on SDMT (L'amante et al., 2012).

Finally, in Figure III.9a the friction angle, φ', profiles, estimated through direct semi-empirical correlations based on CPT results (Durgunoglu & Mitchell, 1975; Robertson & Campanella, 1981) are compared to that obtained by L'amante et al. (2012) by interpreting the SPT results. The friction angle profiles estimated by CPT correlation show, on average, a decreasing trend in the first 15m depth that than keep constant around a value of 35° up to the yellow tuff. On the contrary, SPT-based φ' evidences a more constant trend around the value of 38°.

Material, devices and experimental procedures

IV.1 The investigated materials

The soil samples used in this study were taken from the front of an excavation cut. inside the shaft station of San Pasquale at a depth of about 18.5m. As shown in Figure III.5 the sampling was carried out in an ashy silty sand layer, between two red pumices layers included in the pyroclastic layer. The samples were taken in two ways:

1. undisturbed soil specimens directly sampled using molds of ϕ38 and ϕ36 mm diameters;
2. undisturbed block samples taken from the excavation front . Blocs were cut and immediately sealed with paraffin. Their size was large enough to consider that specimens carved from the center of the block can be considered as undisturbed.; furthermore about 50 kg of disturbed material were also taken to prepare the reconstituted soil samples.

The material taken at 18m, during the research, was subjected to several grain size analyses for the identification and the classification of the soil. The collected grain size distributions are plotted in Figure IV.1 and compared with the limit curves suggested by the NTC 2008 for a preliminary screening of the liquefaction potential for soil (Tsuchida, 1970).

All the tested samples can be classified as sandy soil characterized by a variable silty fraction ranging between 10% and 45% and a gravelly fraction not exceeding 35%; the entire fuse obtained fall within the limits characterizing the liquefiable soils with uniformity coefficient U_C>3.5.

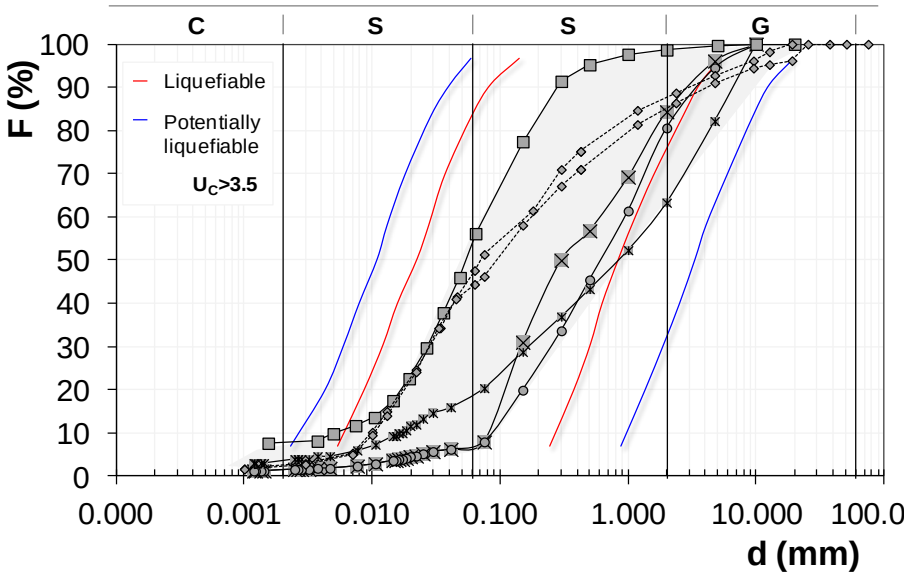

FIGURE. VI.1: GRAIN SIZE DISTRIBUTION OF 'RIVIERA DI CHIAIA' PYROCLASTIC SOILS

The gravelly fraction is made up of pumice lapillus and a small quantity of scoriaceous and lava lapillus, while the fine content is essentially constituted by ash composed by vitrified and blown tiny lava shreds mixed with fragments of crystals and rocks. Given this mineralogy the fine content resulted completely no plastic.

The experimental program included tests on undisturbed and reconstituted samples, since the laboratory investigation was aimed to evaluate the influence of structure and texture, on cyclic liquefaction resistance. In the following the undisturbed material is called (PAN) soil, to distinguish it from the reconstituted ones (PARa and PARb). Furthermore, in order to analyze how particles fragility and non plastic fine of pyroclastic soils could affect the cyclic resistance two more set of reconstituted samples were prepared modifying the mineralogy of either the fraction passing the sieve 200 or holding at the same sieve.

IV.2 Description of materials used

In order to evaluate the role of particles fragility, the mechanical and liquefaction features of PAR were compared to that of reconstituted soil samples having the same grain size distribution, but prepared replacing the pyroclastic sandy particles (% holds at 200 sieve) with hard-grained silica sand (SAR). Silica sand, used for the

sample preparation was taken from the embankment deposits liquefied during the 20/05/2012 earthquake in Emilia-Romagna (Italy).

On the other hand, the effects of non-plastic ashy content was evaluated by comparing the PAR features with that of a pumice-clay (PCR) mixture, again characterized by the same grain size distribution, but obtained substituting the ashy fine fraction with a low plasticity clay.

The reference grain size distribution defined to prepare the reconstituted specimens is illustrated in Figure IV.2. In particular, the reconstituted material (black line with black dots in Figure IV.2) is characterized by d_{max}=1mm, U_C> 3.5 and fine content, FC=30%. Such a features of the grain size curve were established taking into account both the availability of particles diameters of silica sand (d_{max}=2mm) and the typical grading of pyroclastic soils. Moreover, F_C=30% was defined on the basis of recent literature instructions regarding the liquefaction features of sand-silt mixtures. In fact, according to Mominul et al. (2013) percentage higher than 30% of non-plastic silt does not further modify the liquefaction resistance.

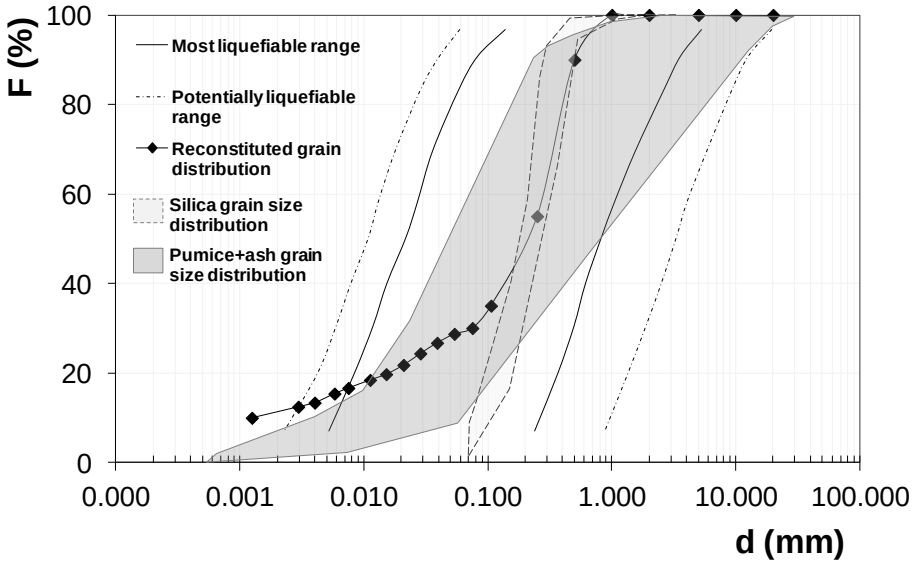

FIGURE. IV.2: GRAIN SIZE DISTRIBUTION OF PYROCLASTIC SOIL, SILICA SAND AND RECONSTITUTED SOIL.

The specific gravity of the different soil components and that of the mixtures are listed in Table IV.1.

TABLE IV.1: PHYSICAL PROPERTIES

Material	Pyroclastic sand	Silica sand	Clay
γ_s (kN/m^3)	24.62	26.39	26.59
Ip (%)	-	-	20
γ_s mixture (kN/m^3)	-	**S-A**	**P-C**
		25.99	25.01

IV.3 Preparation techniques of reconstituted specimens

The specimen preparation technique was chosen on the basis of the fulfillment of the following requirements: setting up homogeneous specimens with uniform distribution of void ratio and characterized by the lowest possible density.

Before reconstituting the specimens, the pyroclastic sand was preliminary sieved to separate each grains fraction. Every fraction was then gently washed in order to remove the fine content which would have affected the grain size distribution of reconstituted specimens (Figure IV.2).

It is well known that the preparation technique influences the mechanical response of a soil (Mulilis et al., 1977). In this experimental campaign, the choice of the most suitable reconstitution technique was the result of a compromise between the need to carry out tests on saturated specimens and the need to set up very loose samples. Two preparation procedures were considered: moist-tamping (MT) method and modified water pluviation + freezing (WPF) method.

MT method, widely described in literature (Mulilis et al., 1977; Tatsuoka et al., 1986), consisted of preparing specimens with a known void ratio, by tamping wet soil in 7 layers, 1cm thick. Since it has been demonstrated that the final porosity is a function of the water content with which the specimens are prepared (Olivares et al. 2009), during the reconstitution several water quantities were added to soil by trials, in order to make specimens with the maximum porosity possible.

The most critical aspects of MT preparation method was the saturation phase of the specimens and the triggering of liquefaction phenomena during the assembling of the specimen into the devices.

Since it resulted extremely difficult to avoid sample liquefaction during the set up phase after saturation, the WPF preparation technique was finally preferred. The preparation phases are synthesized as follow:

- Assembling a special mold, specifically designed during this investigation;
- Pouring into the mold an amount of water corresponding to the water content of saturation;
- Pouring by a funnel a known amount of dry soil into the mold;
- Freezing at -30°.

The mold was simply made with a transparent plastic sheet folded to make a cylinder having the required inner diameter. Such a sheet was graded to prepare the specimens of different height. At the basis, the plastic sheet was assembled on a solid cylinder surrounded by a gasket in order to ensure the watertight. Finally, the sheet was hold around the solid cylinder and the gasket by o-rings (Figure IV.3).

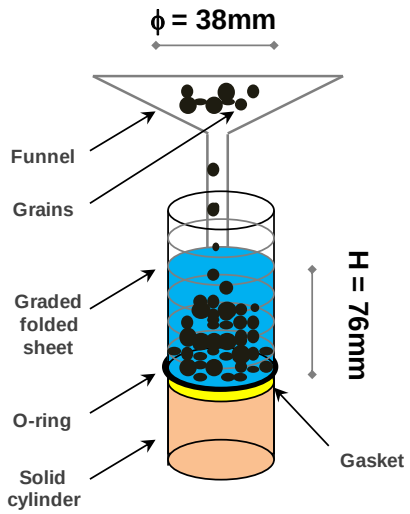

FIGURE IV.3: A SPECIAL MOLD REALIZED TO PREPARE AND FREEZE SATURATED SPECIMENS.

The mold was filled with distilled water and the soil has been poured with a funnel from the top water surface. The funnel had a little hole from which the soil was

poured grain by grain, in order to avoid turbulences which in turn could induce non uniformities within the specimen. Finally, the specimen was frozen.

IV.4 Devices and procedures

The laboratory investigation was conducted by means of conventional apparatuses (oedometer and standard triaxial cel) as well as by more sophisticated devices (stress path triaxial cell and cyclic and dynamic torsional shear device). The experimental program allowed identifying both the influence of structure and texture on compressibility and strength of the pyroclastic soil subjected to static loads and the material response under cyclic and dynamic loads. In the following a brief description of the less conventional devices will be provided.

IV.4.1 Controlled stress-path triaxial cell

Most of the experimentation was carried out by means of stress-path controlled triaxial cell which is presented in this paragraph. The cell is a modified version of Bishop & Wesley (1975) prototype which has been already described by Santucci de Magistris (1992) and Aversa & Vinale (1995) capable of working in both stress and strain controlled conditions.

The whole system can be divided into three parts: a hydraulic triaxial cell; a system to set the pressures; a calculator for the acquisition and the monitoring of the test.

The triaxial cell is an hydraulic apparatus designed to test samples of 38mm in diameter and 76mm in height, with a moving piston located in the bottom part of the device that pushes the soil sample against an internal load cell. The piston is moved up and down by an hydraulic ram.

Three electro-pneumatic pressure converters (Watson-Smith Ltd type) let to independently apply and control cell, pore and axial pressures. A stepping motor driven screw pump let performing tests in strain-controlled condition (Atkinson, 1984).

The triaxial system is equipped with several transducers in order to measure the current state of the sample. The load cell (Wykeham Farrance type) is located inside the triaxial cell in order to avoid any kind of frictions (Tatsuoka, 1988). In order to measure the pore pressure and cell pressure, membrane-transducers are used with 1000kPa full scale.

Axial strains are measured externally by a LVDT which is integral to the movements of the piston. Moreover, volumetric strains are measured by a volume gauge which measures the amount of water that goes in and out the specimen.

In order to read the signals of transducers and to control the pressure regulators, a A/D-D/A (CIL Group) is adopted. The remote control via pc is managed thanks to open source QuickBasic software that permits the acquisition of all the transducers, the control of the electro-pneumatic regulator and of the stepping motor, and the feedback control between required and measured parameters

IV.4.1.1 Triaxial tests procedures

Test procedures for triaxial tests in a stress-path controlled cell have been widely described (Santucci de Magistris, 1992; 1996). In this paragraph the peculiar aspects regarding the different procedures adopted for the setting up of intact and reconstituted specimens are detailed.

- *Undisturbed soil*

The undisturbed samples, taken from the excavation cut, were in an unsaturated condition since during the excavation phase the ground water level in the station shaft was depressed.

The saturation procedure suggested by Olivares & Picarelli (2001) was adopted. This technique takes advance of the high CO2 solubility in water. Using an external air/water interfaces hooked up to drainage circuits of the cell, the specimen is first flashed with CO_2 that is then replaced by de-aired water. This technique allows specimens saturation applying very low stress condition.

In order to evaluate correctly the void ratio, it was necessary to monitor the dimensions of the specimens during the testing steps. The saturation may induce significant volume variation related to collapse or swelling of the specimen due to the progressive reduction of suction. Nevertheless, during the saturation phase the measurement of water volume does not correspond to volumetric strain of the specimens this implies that volume variations cannot be measured by volume gauge. For this reason after the saturation phase the cell was disassembled to measure the dimensions of the specimens. After the consolidation step, the cyclic tests were performed by applying undrained axial stress varying with a sinusoidal law whose frequency (0.006Hz) was chosen low enough to equalize the pore pressure within the specimen (Hight, 1982).

- *Reconstituted soil*

Reconstituted samples were initially prepared adopting the moist-tamping technique in unsaturated conditions. Nevertheless, during the set up phase many specimens liquefied because of their very loose state and, if this was not the case, they always experienced very high volume variations during the saturation phase that significantly modified the target density.

The previous difficulties were overcome by assembling saturated and frozen specimens. This procedure only required to quickly set up the specimen into the cell to avoid the thawing before pressure was applied.

IV.4.2 Resonant column and torsional shear cell (RCTS)

The resonant column and torsional shear device used in this investigation is described in details in Silvestri, (1991) and d'Onofrio, (1996) that is why, once again, in this paragraph the main features are just reported.

The apparatus is capable of applying a maximum torque M_T of more than 5 Nm. The torque is applied through an electro-magnetic motor which generates the specified torque by coupling four pairs of coils and corresponding magnets. The torque amplitude M_T is directly measured by a transducer installed under the drive plate, at the specimen top. The rotation θ is measured by two couples of gap sensors allowing

accurate readings of shear strains spanning from $\gamma=5x10^{-5}$ % to 0.5 % on a specimen of 36 mm in diameter.

According to the test conditions required, a function generator allows to apply shear loads which can vary in amplitude, frequency and wave-form.

Axial and volumetric deformations are measured by a LVDT and a volume gage respectively, while a miniaturised pressure transducer allows reliable pore pressure measurements.

With the experimental apparatus described above, it is possible to carry out any sequence of monotonic (MTS), cyclic (CTS), and resonant column (RC) torsional shear tests on a single specimen.

The configuration of the control-acquisition system consists of the following devices:

- A fully programmable digital signal generator, which, in connection with the power amplifier, generates torsional loads over wide ranges of amplitudes ($5x\cdot10^{-4}$ to 5 Nm), frequencies (0.1 to 100 Hz, with a minimum frequency step of 0.001 Hz) and wave-forms, according to test requirements;
- A fully programmable digital voltmeter that acquires one signal at a time from pressure, displacement and accelerometer transducers;
- A digital counter which records the frequency of the shear loading signal during dynamic tests;
- a digital oscilloscope which records time histories of torque, rotation, pore pressure and axial displacement, during monotonic and cyclic tests.

The core of the entire instrumentation chain is a digital switching box, that:

- connect the signal generator to the loading system;
- connect the appropriate transducer to the relevant digital acquisition instrument, in order to record the frequency-amplitude response during resonant column tests or the stress-strain time history during monotonic and cyclic tests;

- scan all the output signals of pressure, axial strain and volume change transducers and send them through to the voltmeter buffer, thus allowing an automatic and continuous record of the consolidation stages.

The recording devices transfer digitized data to the computer; the I/O communication occurs via an IEEE 488 port.

IV.4.2.1 Procedure for RCTS tests

RCTS tests were carried out only on undisturbed samples. Some more difficulties arose in the saturation phase because the device is equipped with just one drainage line in the bottom pedestal.

In a first trial test, the saturation was carried out applying a cell pressure lower than the lithostatic mean effective stress (p=120kPa and back-pressure=100kPa) but the required level of saturation (S_R>95%) was not achieved.

In a second trial, higher values of cell pressure and the back-pressure have been applied (p=320kPa and back-pressure=300kPa). In this case, on the specimen was applied an effective confining pressure greater than in-situ one: because of that the soil was subjected to an instantaneous volumetric strain, due to the compression of the air inside the specimen, whose evaluation was not possible.

Once again, in this second case, B-tests have not provided the correct values of saturation, so the following part of the test was performed in unsaturated conditions.

After the saturation, a consolidation stage at the estimated in situ stress followed.

At the end of the isotropic loading path, an undrained sequence of CTS and RC tests was performed with increasing strain levels, in order to investigate the behaviour of the pyroclastic ash from small to medium strains. In all the tests, a back-pressure typically around 200kPa was adopted.

IV.4.3 Definition of parameters used during cyclic tests

The interpretation of dynamic tests differs from that of cyclic tests because these latter allow for a 'static' analysis of the equilibrium of the soil element. The procedures adopted to estimate the stress-strain parameters in the different test types will be briefly reported in the following subsections, respectively regarding the shear modulus and the damping ratio.

- *Shear modulus*

During CTS tests, the stress-strain relationship can be directly obtained from the continuous acquisition of torque and rotation. Once the time records are reduced in terms of stress-strain curve, τ_{pp}-γ_{pp}, the shear stiffness G from and CTS tests is computed using the following expressions:

$$G = G_{eq} = \frac{\tau_{pp}}{\gamma_{pp}} \tag{IV.1}$$

where: τ_{pp} and γ_{pp} are peak-to-peak shear stress and strain values pertaining to a given CTS cycle.

The interpretation criteria of resonant column tests (RC) refer to the dynamic equilibrium of the specimen-drive plate system. The shear modulus from a dynamic test, G_{dyn} , is obtained on the basis of the wave propagation theory in an ideal elastic continuum:

RC tests:

$$G_{dyn} = \rho V_s^2 \tag{IV.2}$$

where the shear wave velocity is calculated by solving the frequency equation at the first resonance mode:

$$\frac{I_P}{I_0} = \frac{2\pi f_r L}{V_S} \tan\left(\frac{2\pi f_r L}{V_S}\right) \tag{IV.3}$$

where I_0 is the mass inertia moment of the drive system; I_p is the inertia moment of the specimen; f_r is the measured resonance frequency; L in the height of the specimen; V_s is the shear wave velocity of the tested soil.

As shown by equations (IV.2) and (IV.3), the determination of several quantities is required in the evaluation of the 'dynamic' shear modulus, G_{dyn}: besides to a convenient accuracy in the frequency measurement (the resolution of which is generally as high as 0.01 Hz), a comparable accuracy in the measurement of the specimen geometry is also needed. Moreover, it can be shown that errors in the measurements of height, diameter and volume of the specimen can affect the evaluation of G_{dyn} in a major extent than those involved in the measurement of frequency itself (Silvestri, 1991a).

The same considerations apply to the estimate of the reference peak strain, γ_{max}, derived from the measurements of top rotation amplitude, θ_{max}, specimen height, *L*, and equivalent radius, $\overline{R}$.

- *Damping ratio*

The equivalent damping ratio in cyclic torsional tests was directly derived from the definition, i.e.:

$$D_{CTS} = \frac{W_D}{4\pi W_S} \qquad \text{(IV.5)}$$

where W_D is the dissipated energy during the current cycle while W_S is the energy accumulated during the 1° cycle (Figure IV.4).

The use of equation (IV.5) was implemented in the CTS testing procedure through numerical integration routines applied to the digitised stress-strain loops (Silvestri, 1991a); it follows that the damping ratio evaluated in CTS tests directly derives from stress and strain measurements, and results sensitive to the same experimental uncertainties as the shear modulus G_{eq}.

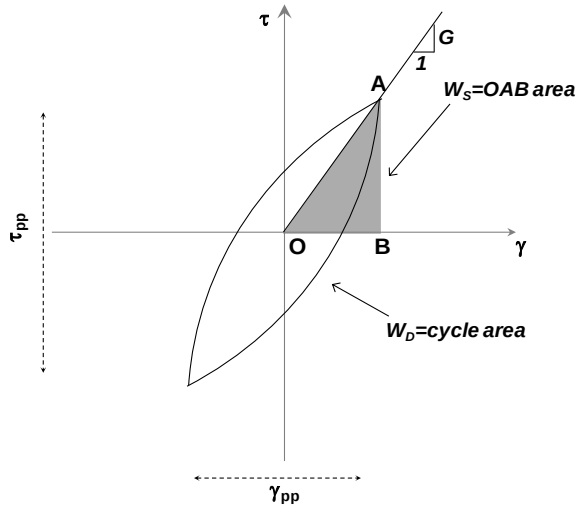

FIGURE IV.4: GEOMETRIC-ANALYTIC DEFINITION OF THE EQUIVALENT SHEAR MODULUS AND DAMPING RATIO (SILVESTRI, 1991).

On the other hand, the evaluation of the damping ratio from RC tests is based on the assumption of the equivalence between the real soil and the ideal visco-elastic medium, such as in the Kelvin-Voigt rheological model.

According to the experimental tradition and some national standards (e.g. ASTM D4015-87), the results of RC test can yield two different estimates of the damping ratio:

- D_{rf} , obtained adopting the "resonance factor" method:

$$D_{rf} \cong \frac{M_0 \overline{R}}{2GJ\gamma_{max}} \tag{IV.6}$$

  where M_0 is the torque amplitude, J is the polar moment of inertia of the cross-section;

- D_{hp} , resulting from the so called " half power" method:

$$D_{hp} = \frac{f_2 - f_1}{2f_r} \tag{IV.7}$$

  where f_1 and f_2 are the so-called frequency cut-off values.

Since based upon completely distinct approaches, and affected by different experimental factors, the two methods systematically yielded consistent results throughout the entire experimental program.

Similarly, in the triaxial cyclic tests a secant Young modulus, E, was evaluated at each cycle as follows:

$$E = \frac{q_{pp}}{\varepsilon_{pp}} \tag{IV.8}$$

Experimental results

V.1 Introduction

The results of the experimental program included tests on undisturbed and reconstituted samples, since the laboratory investigation was aimed to evaluate the influence of structure, texture, fragility of particles and non-plastic fine content on cyclic liquefaction resistance. In particular, the investigation regarded pumice+ash intact and reconstituted (PAN, PARa and PARb) and, in addition, the mixtures of silica sand+ash (SAR) and pumice+clay (PCR). In Appendix 1 the physical and state properties monitored during each phase of the tests are reported.

V.2 Compressibility

Compressibility features of mixtures were determined by performing isotropic compression tests in a range of effective mean stresses, p', varying differently for each material between 50kPa to 600kPa.

Figures V.1a-b-c show the results of isotropic compression in terms of void ratio, e, and effective mean stress, p', respectively for intact and reconstituted pumice+ash (PAN, PAR-a and PAR-b), pumice+clay (PCR) and silica+ash (SAR).

It can be noticed in Figure V.1a that at the same effective mean stress, p', PAN shows very high void ratio if compared with reconstituted PAR-a and PAR-b. PAR-a and PAR-b mixtures, prepared by two different techniques at the same initial relative density, at the start of the isotropic compression show different void ratios because of volumetric collapse associated to the different assembling procedures (see Chapter IV).

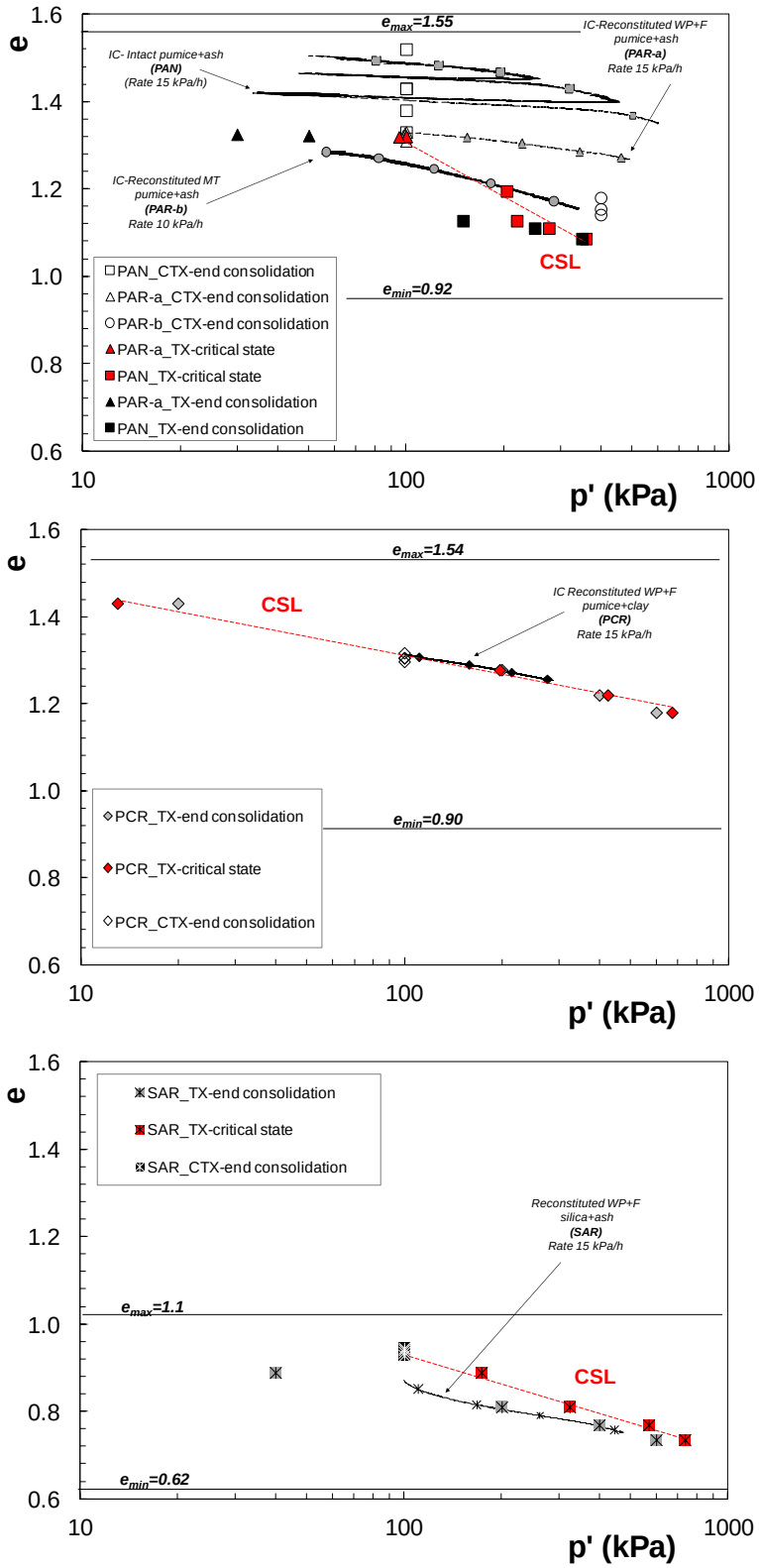

FIGURE V.1: SYNTHESYS OF EXPERIMENTAL RESUSLTS FOR PUMICE+ASH (A); PUMICE+CLAY (B); SILICA+ASH (C).

In addition, comparing PAR-a and PAR-b curves, it can be noticed that the compressibility is slightly affected by the rate of application of loads since the slope

of PAR-a compressibility curve is lower than PAR-b one. Such an occurrence may be addressed to creep phenomena associated to the fragility of particles (Penta et al., 1961) induced by the slower application of isotropic pressure.

PARa and PCR curves in Figure V.1a and Figure V.1b, being both pumice sands with the same fine content, respectively, non plastic and plastic, show the same initial void ratio. The compressibility of mixture containing clay is slightly higher than pumice+ ash.

Despite of PCR, PAR-a and SAR were prepared by the same technique, grain size distribution and fine content, Figure V1.c show the latter mixture has very low void ratio likely addressed to the segregation of heavier silica particles.

It can be noticed that in Figure V.1a, the dots of intact PAN related to the end of consolidation of CTX and TX show marked differences of void ratio and do not lay opportunely on its isotropic compression. Such an occurrence may be addressed, somehow, to the heterogeneity of undisturbed samples of PAN. On the contrary for all the reconstituted mixtures, PAR-a, PAR-b, PCR and SAR, the end consolidation void ratio lay on the own isotropic compression curves which are very close to the projection of critical state line.

V.3 Strength under monotonic loads

In order to investigate the strength features of materials, a set of triaxial compression tests was performed.

In Figure V.2, the results of drained and undrained tests are illustrated for the intact and reconstituted pumice+ash (respectively, PAN and PAR-a) under the application of different effective cell pressures. In particular, PAN was tested under both drained and undrained conditions by applying values of effective mean stress comparable with the stress state in situ, 100kPa<p'<350kPa; instead, PAR-a was consolidated at low confining stresses, p'=30kPa and 50kpa.

The effective stress paths in Figure V.2 show that the undrained behavior is characterized by an initial contraction followed by a point of phase transformation

and increasing dilatancy. In the range of in situ confining pressures, PAN has a partially stable behavior. PAR-a, at 30kPa, shows only dilatant behavior.

Figure V.2a shows the deviator stress versus the axial strain. It can be observed that the point of phase transformation occurred before than 3% axial strain. After this point axial strains increase to value close 20% at which point is considered that steady-state conditions were achieved.

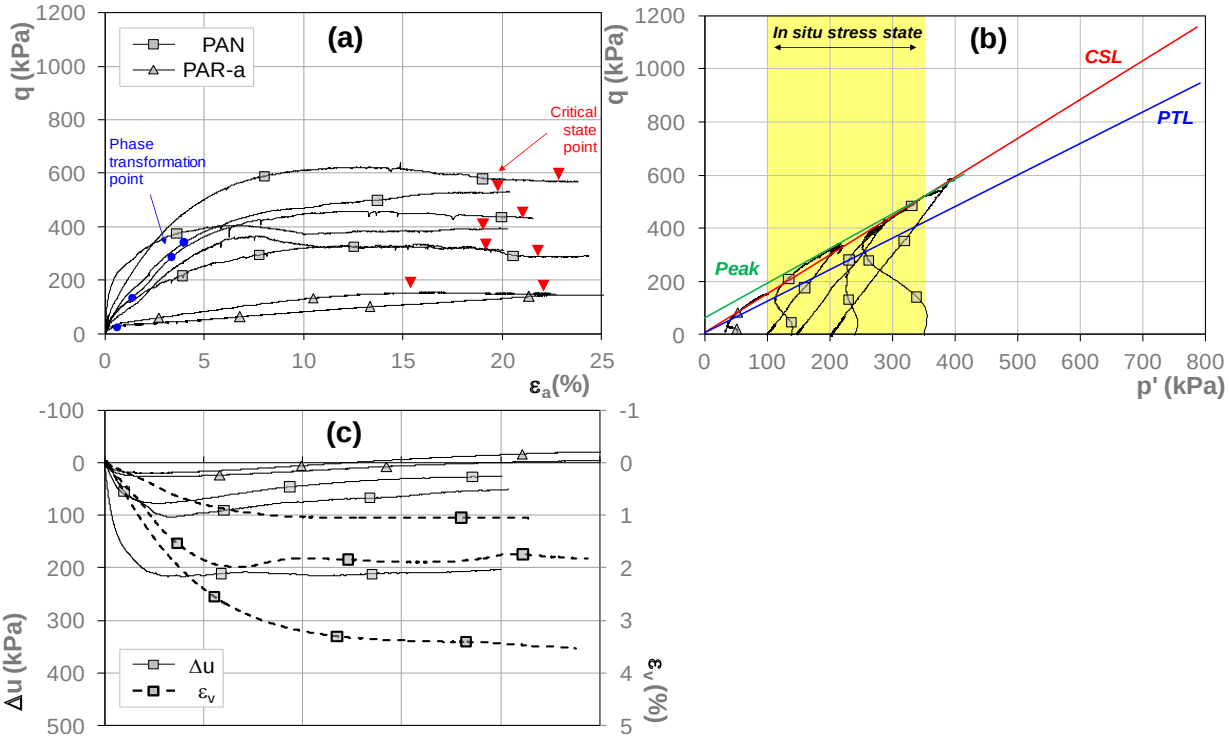

FIGURE V.2: PAN AND PAR-A STRESS-STRAIN CURVES (A); EFFECTIVE STRESS-PATHS (B); PORE PRESSURE INCREMENTS, VOLUME STRAINS AGAINST AXIAL STRAINS (C).

Figure V.3 and V.4 show the compression triaxial results respectively for PCR and SAR. The tests were only performed in undrained conditions and in a range of confining stress range varying between 30kPa up to 600kpa.

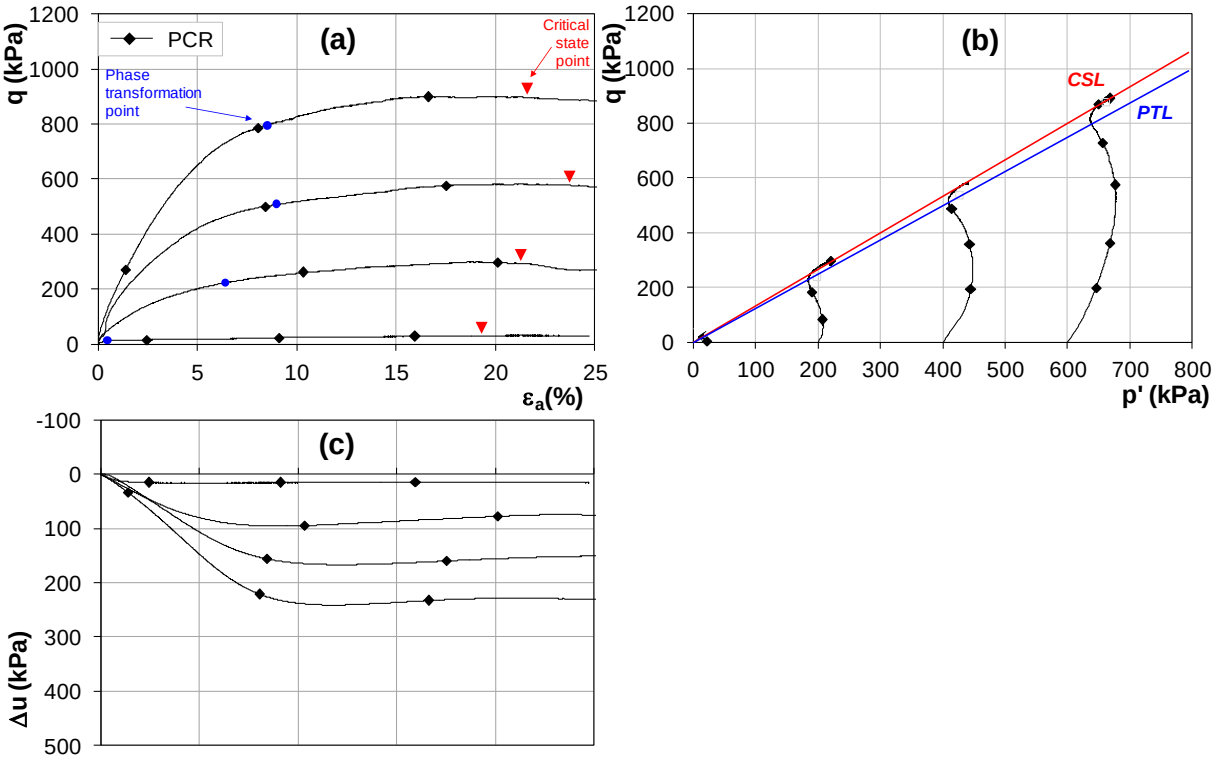

FIGURE V.3: PCR STRESS-STRAIN CURVES (A); EFFECTIVE STRESS-PATHS (B); PORE PRESSURE INCREMENTS, VOLUME STRAINS AGAINST AXIAL STRAINS (C).

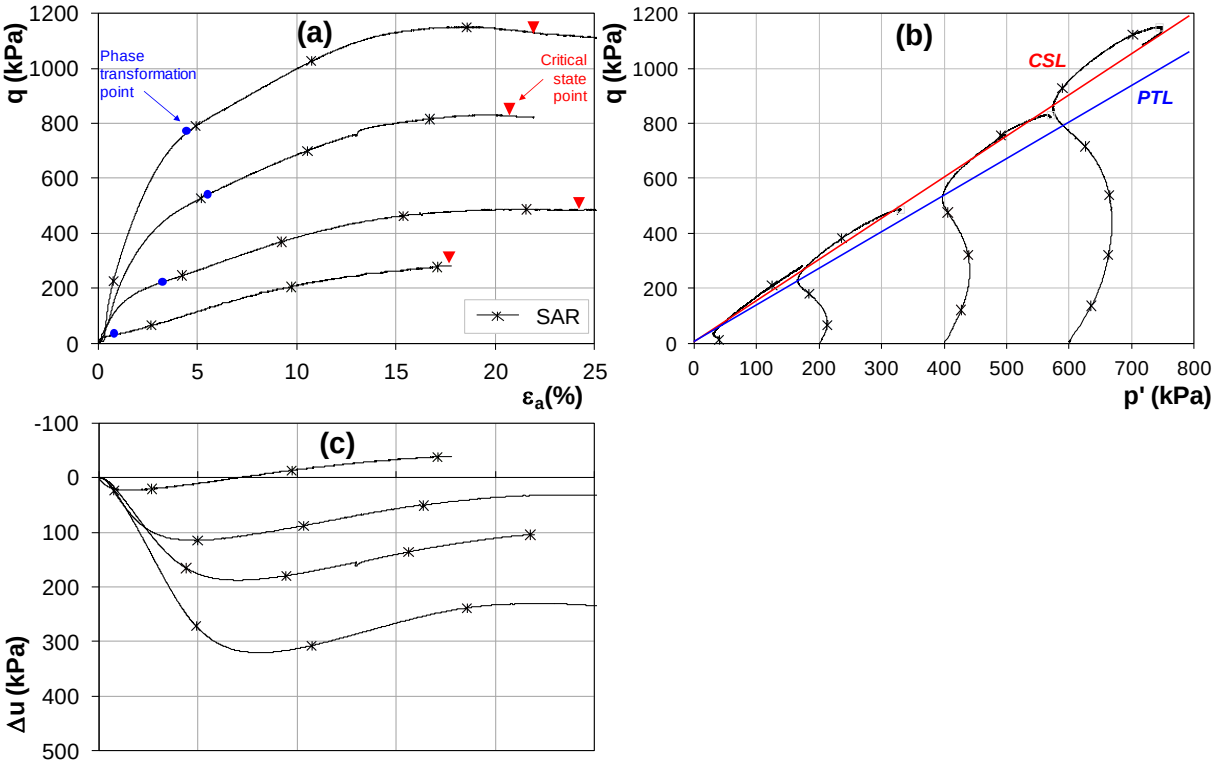

FIGURE V.4: SAR STRESS-STRAIN CURVES (A); EFFECTIVE STRESS-PATHS (B); PORE PRESSURE INCREMENTS, VOLUME STRAINS AGAINST AXIAL STRAINS (C).

As illustrated in Figure V.2b and Figure V.3b, the effective stress path, once again, show a partially stable behavior for which, after a rapid increasing of positive pore pressures, the latter become stable with an increasing of p'.

Comparing Figure V.2a and Figure V.3a, it can be noticed that for the stress-strain curves of PCR, the phase transformation points correspond to higher value of axial strain than stress-strain curves of SAR. In both PCR and SAR stress-strain behavior no softening is shown and, even, SAR shows a slightly hardening behavior more markedly as the deviator and the effective confining stress become higher and higher.

The synthesis of strength parameters of the mixtures is reported in Table V.1:

TABLE V.1: STRENGTH PROPERTIES

	M_{peak}	φ'_{peak} °	c' kPa	M_{cv}	φ'_{cv} °
Pumice + Ash	1.34	34	18	1.51	38
Pumice + Clay	-	-	-	1.32	33
Silica + Ash	-	-	-	1.52	38

V.4 Results of cyclic triaxial tests

The main goal of the experimental program was the analysis of the undrained cyclic behavior of pyroclastic soil highlighting the influence of fabric, particles fragility and non plastic fine on the cyclic resistance of this material. Cyclic triaxial tests were carried out on natural (PAN) and reconstituted pumice with ash soil (PARa and PARb) with the aim of analyzing the influence of fabric, relative density and stress state. Furthermore the cyclic resistance of the reconstituted pumice+ash soil (PARa) was compared to that of a material with the same grain size distribution, but prepared with hard-grained silica sand and the same ashy fine content (SAR), in order to evaluate the effects of particle breakage. Finally, the effects of non-plastic ash content were evaluated by comparing the cyclic resistance of the reconstituted

pumice+ash soil with that of a pumice-clay mixture (PCR). The preparation of the reconstituted samples is detailed in Chapter IV. It is worth remembering that reconstituted specimens were all prepared so that, at the end of consolidation phase, they had the same relative density of the natural soil samples (40%) except for the specimens of PARb prepared at a relative density of 60%.

All the cyclic triaxial tests were carried out starting from an isotropic stress state. An effective confining pressure, σ'_c equal to 100kPa was applied in all tests except for those carried out on the reconstituted specimens of PARb, subjected to an isotropic effective stress of 400kPa. After consolidation, each specimen was shared in undrained conditions by applying a cyclic axial stress of given amplitude until the achievement of failure conditions.

Figure V.5 reports the results obtained on natural soil samples, PAN in terms of stress-strain response and related stress path obtained applying a cyclic deviator stress increasing from 60 kPa up to 100 kPa. All the specimens showed a cyclic mobility mechanism at failure, more evident at higher deviator stresses (80kPa and 100kPa); the cyclic axial strains increase at an almost constant rate up to large values but no brittle collapse occurs. The same cyclic mobility mechanism is also exhibited by the reconstituted specimens of the same soil (PARb) with a relative density of 60% (at the end of consolidation), higher than that of the undisturbed soil samples, and subjected to an isotropic confining stress of 400kPa, as can be observed in Figure V.7.

A totally different behavior instead is shown by the reconstituted samples of the same soil (PARa) with a relative density equal to that of the undisturbed samples (Dr=40%). As it can be noticed in figure V.6 in this case when the stress paths get closer to the zero stress condition axial strains rapidly runaway to failure, as expected when a liquefaction mechanism is triggered. The observed different behaviour between natural and reconstituted specimens of the same soil can be related to the different grain particle arrangement pertaining to the three set of samples. It is wide recognized (Ladd, 1974, Mulilis et al, 1975; Ghionna and Porcino, 2006) that in the case of cyclic loading, fabric has a very important effect on failure mechanism. In this

case field condition (state and history of the natural soil) could have induced a different fabric to soil particles if compared to that of the reconstituted material prepared at the same relative density and tested at the same confining pressure (100kPa); this in turn influences the behaviour at failure. The peculiar particles arrangement induced by depositional and post depositional processes on the natural soil could have had a role in the development of shear dilation that acts to offset the densification induced excess pore pressure giving rise to a cyclic mobility failure mechanism. To obtain the same failure mechanism in the case of reconstituted specimens it was necessary to prepare them to a denser state and to apply an higher confining stress.

A liquefaction failure mechanism is instead triggered in the case of reconstituted specimens of silica sand with ashes, SAR and pyroclastic sand with plastic clay, PCR , as can be observed in Figures V.8 and V.9: in both cases cyclic strain amplitude is initially very small and then rapidly increases up to values in excess of 5%, particularly on extension side of the cycles where large liquefaction strains begin to occur after cyclic stress paths cross the phase transformation line.

All the reconstituted specimens with the same initial relative density and tested at the same confining pressure exhibited the same failure mechanism independently of the mineralogy of the sandy particles and the plasticity of the fine content.

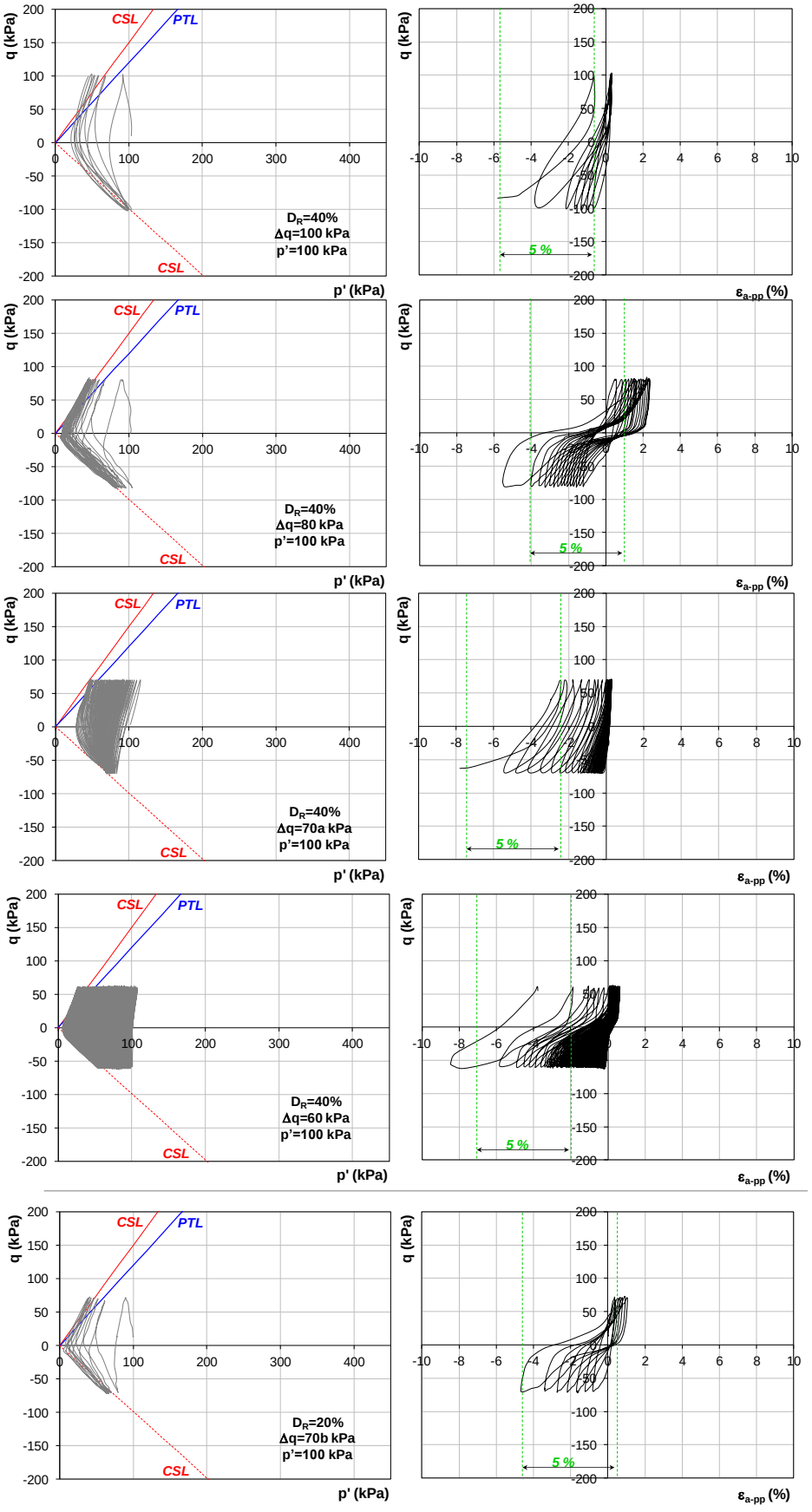

FIGURE IV.5: CYCLIC EFFECTIVE STRESS PATHS AND STRESS STRAIN CURVES FOR INTACT PUMICE+ASH (PAN).

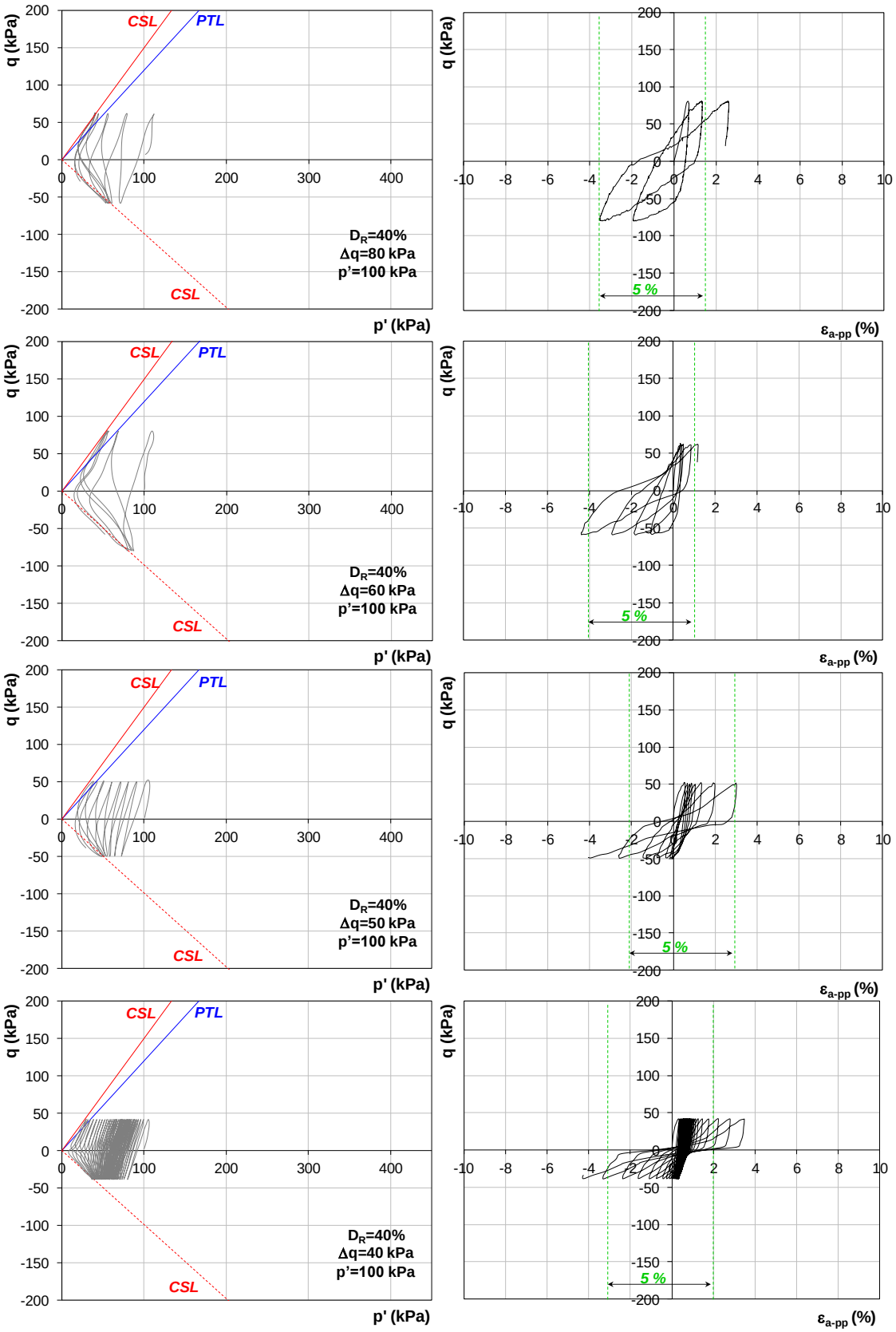

FIGURE V.6: CYCLIC EFFECTIVE STRESS PATHS AND STRESS-STRAIN CURVES FOR RECONSTITUTED PUMICE+ASH (PARA).

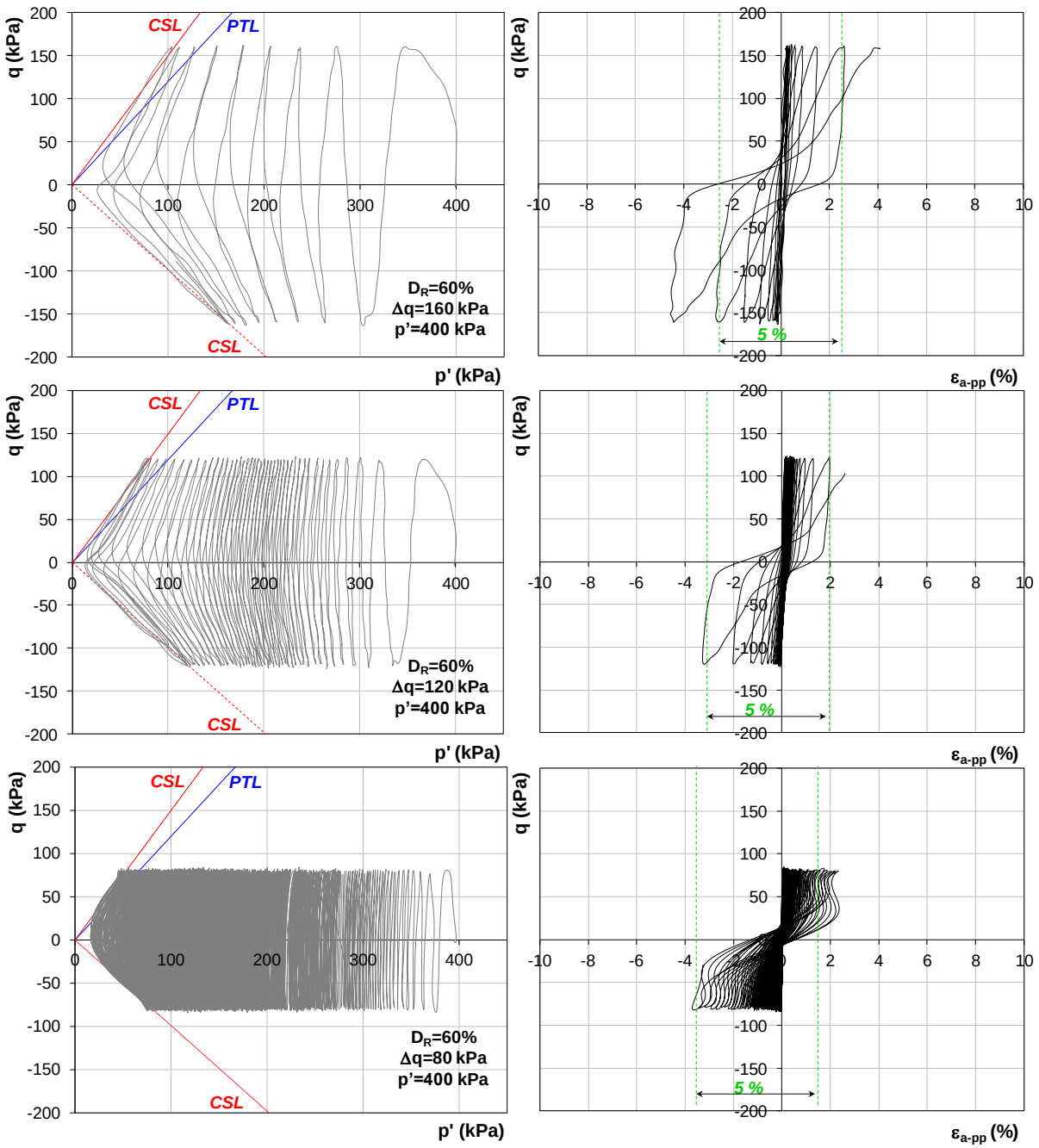

FIGURE V.7: CYCLIC EFFECTIVE STRESS PATHS AND STRESS-STRAIN CURVES OF RECONSTITUTED PUMICE+ASH PARB.

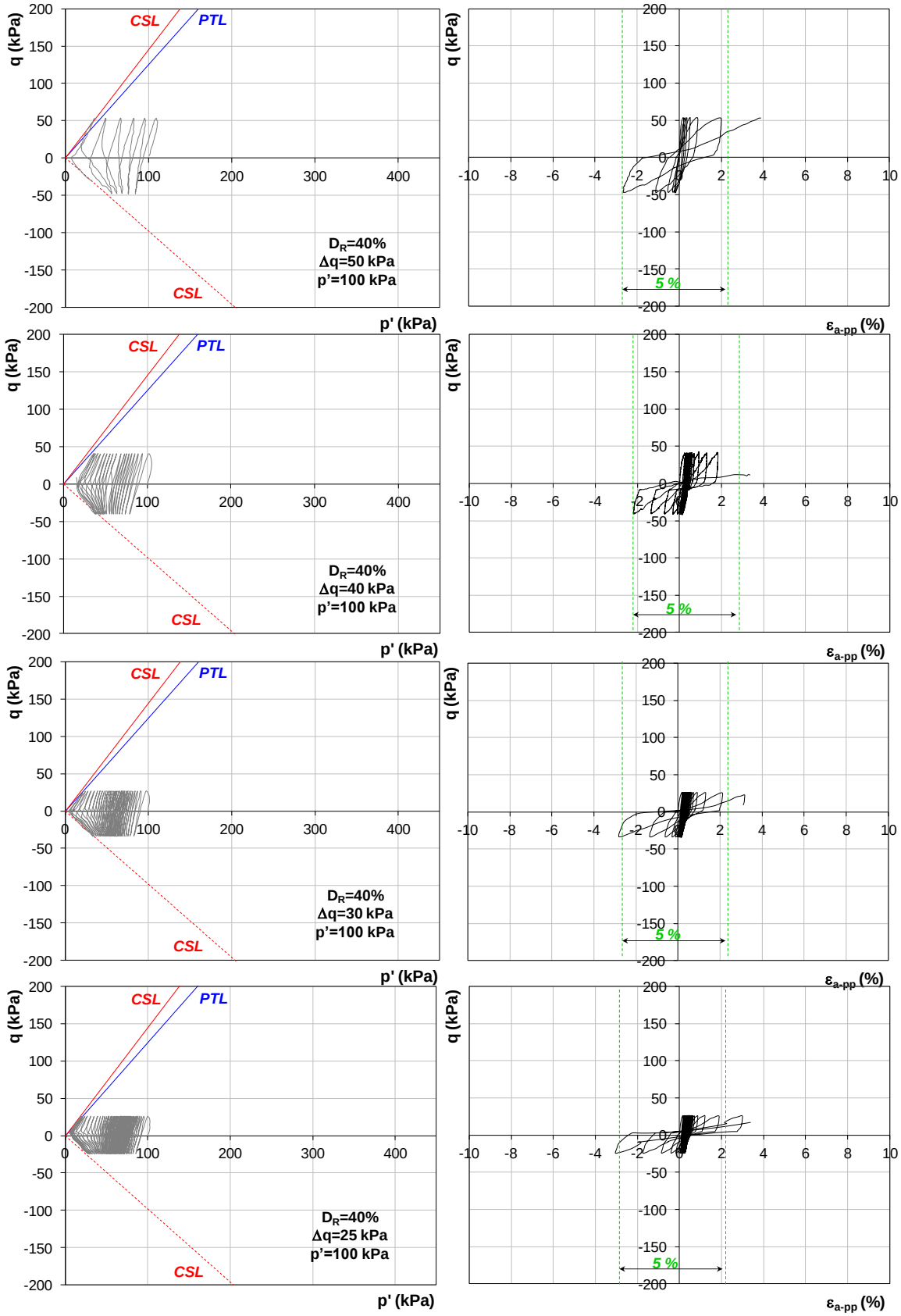

FIGURE V.8: CYCLIC EFFECTIVE STRESS PATH AND STRESS – STRAIN CURVES FOR RECONSTITUTED SILICA + ASH (SAR).

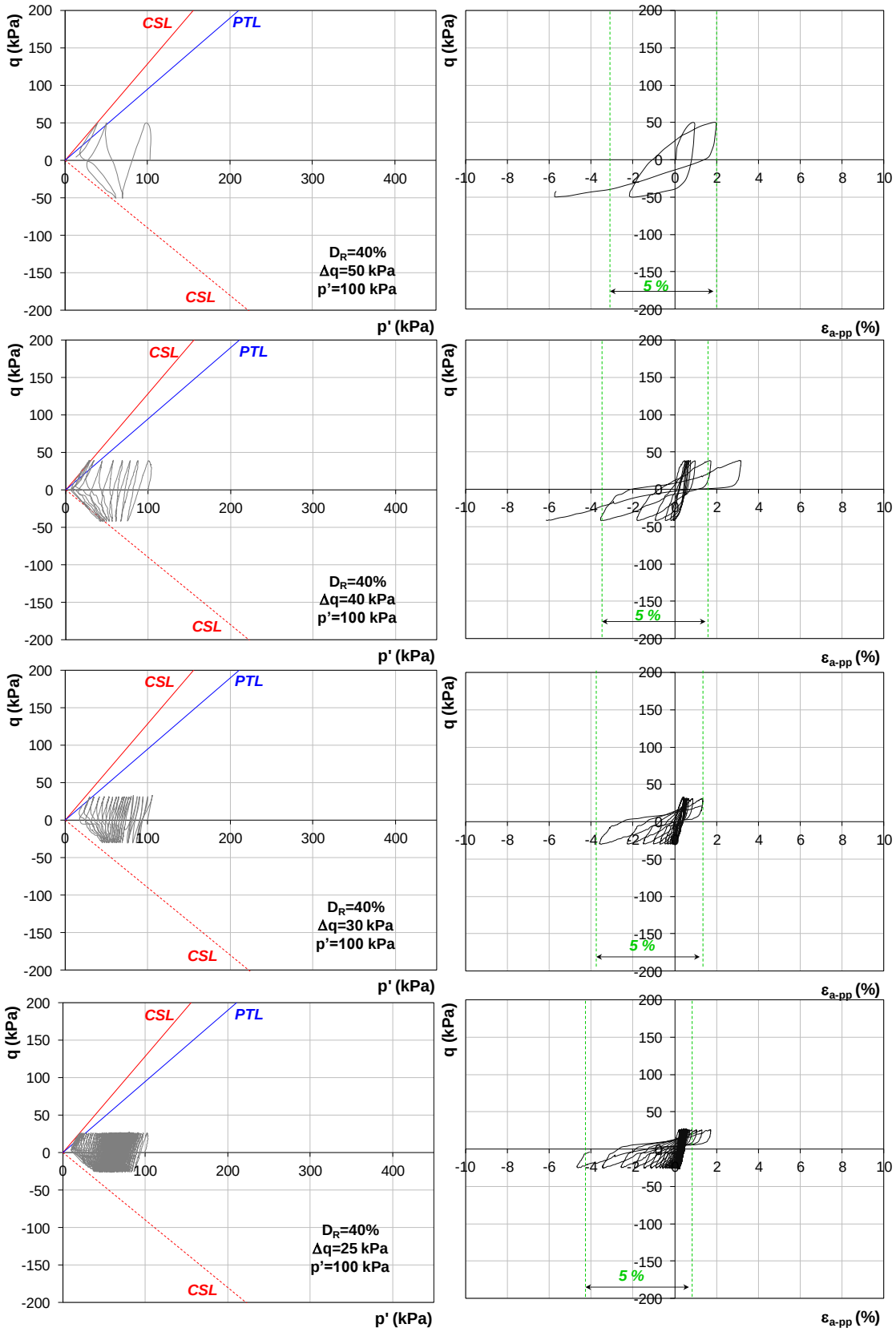

FIGURE V.9: CYCLIC EFFECTIVE STRESS PATH AND STRESS – STRAIN CURVES FOR RECONSTITUTED PUMICE + CLAY (PCR).

V.4.1.1 Undrained cyclic resistance curves

The onset of liquefaction can be defined adopting two different failure criterion. According to the stress criterion, liquefaction starts when the ratio R_u between the pore pressure variation Δu, and the effective confining pressure, σ'_c approaches the value 1. Alternatively, the strain criterion relate the occurrence of liquefaction to the achievement of a double amplitude cyclic strain, $\varepsilon_{a\text{-}pp}$ equal to 5% (Toki et al. 1986; Ishihara 1996). In the present work a pore pressure ratio, R_u of 90% is assumed as stress criterion.

Strain criterion: *Stress criterion:*

$$\varepsilon_{a-pp} = 5\% \qquad R_u = 90\%$$

These two criterion allows the inclusion of both cyclic mobility and the classical liquefaction failures.

Figures V.10-14 show the results of the triaxial tests in terms of the cyclic axial strain, $\varepsilon_{a\text{-}pp}$, and pore pressure ratio, R_u, as function of the number of cycles, N_{cyc}. In the same plots the above defined thresholds values are also reported to identify the onset of liquefaction. Almost all the tests results show that failure occurred at the $\varepsilon_{a\text{-}pp}$=5% condition, much before the attainment of the R_u=90% stress criterion.

Only in the case of natural soil specimen subjected to Δq=70akPa liquefaction is reached only referring to the strain criterion while the pore pressure increment reaches just the 75% of the effective confining stress (Figure V.10). Such a circumstance may be due to localized phenomena of liquefaction inside the specimen that the pore pressure transducer did not catch. Comparing the results obtained on reconstituted samples PARa and PARb, it can be noted that the number of cycles at the onset of liquefaction is inversely proportional to the density of the tested material (Figure V.11 and V.12).

Natural soil samples shows a behaviour almost similar to that exhibited by the reconstituted samples at the denser state characterized, at low deviator stress, by a

sudden change in the accumulation rate of plastic axial strain; while, at higher deviator level, the axial strain are characterized by an almost constant rate of growth.

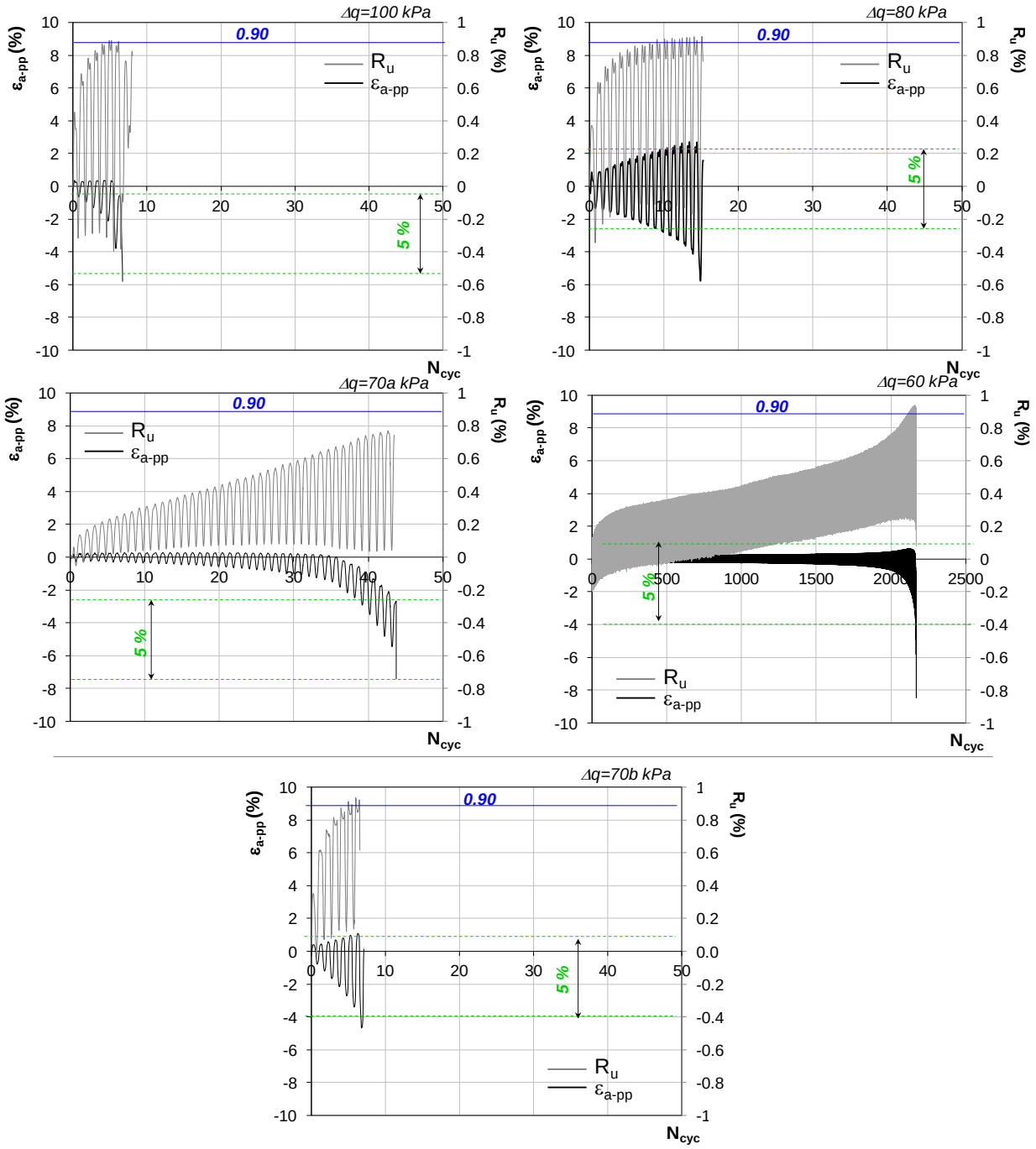

FIGURE V.10: CYCLIC AXIAL STRAINS AND PORE PRESSURE RATIO FOR INTACT PUMICE + ASH (PAN).

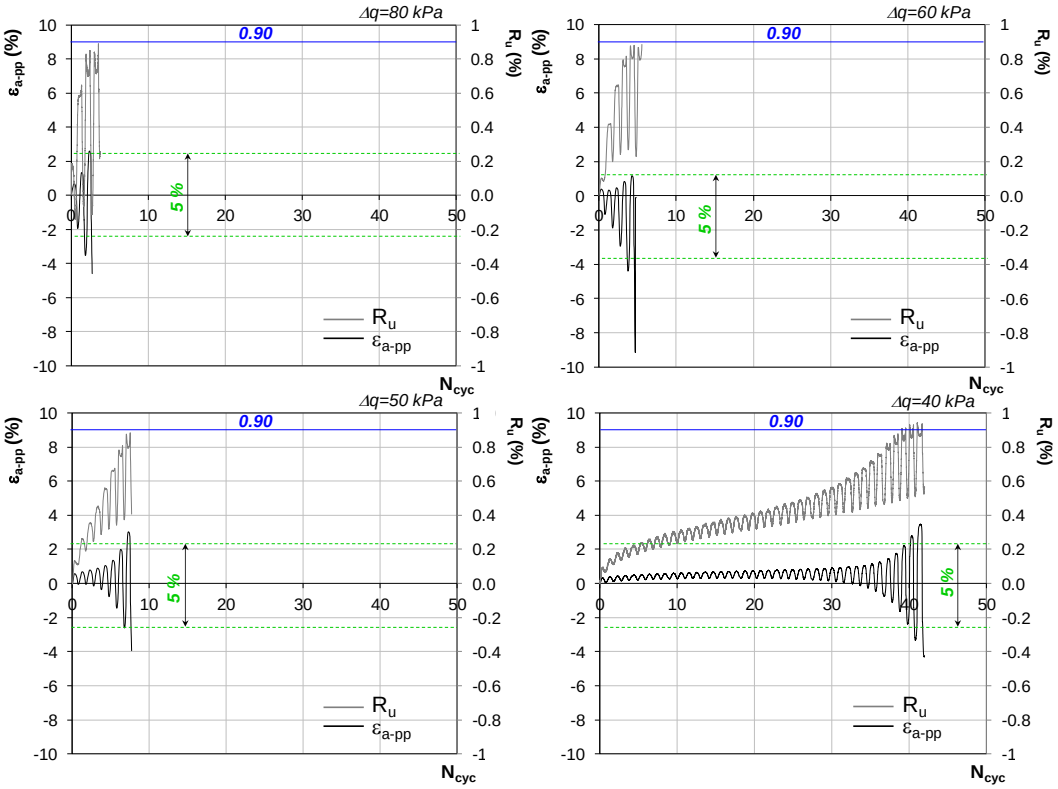

FIGURE V.11: CYCLIC AXIAL STRAINS AND PORE PRESSURE RATIO FOR RECONSTITUTED PUMICE + ASH (PAR-A).

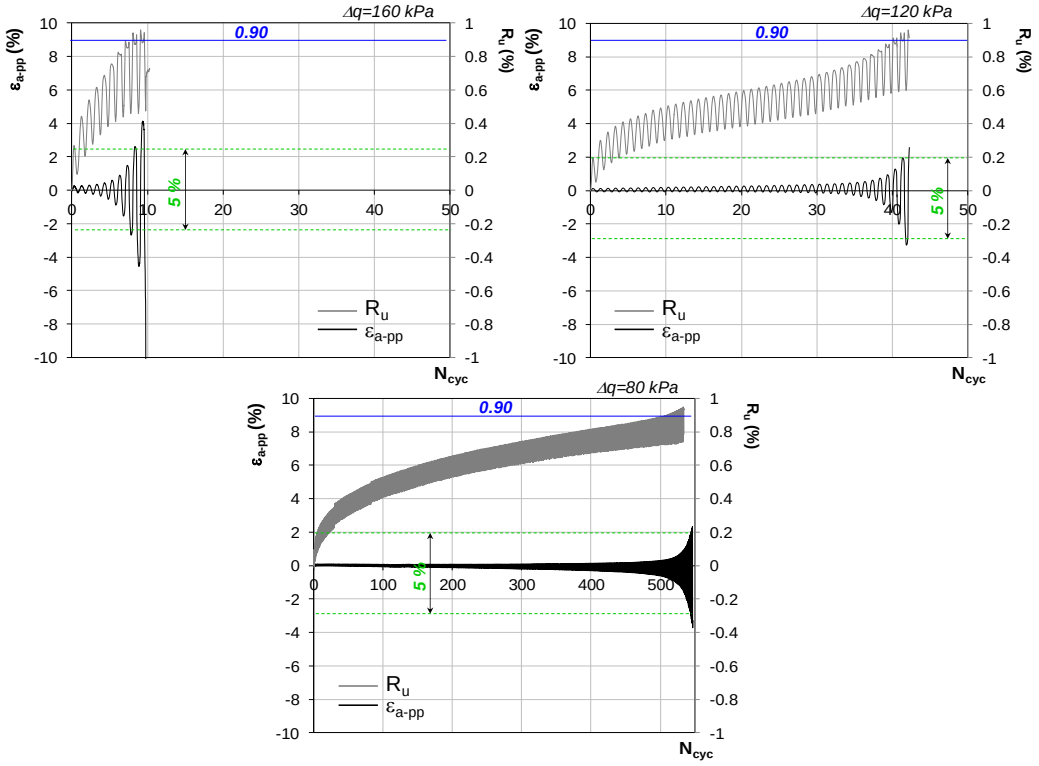

FIGURE V.12: CYCLIC AXIAL STRAINS AND PORE PRESSURE RATIO FOR RECONSTITUTED PUMICE + ASH (PARB).

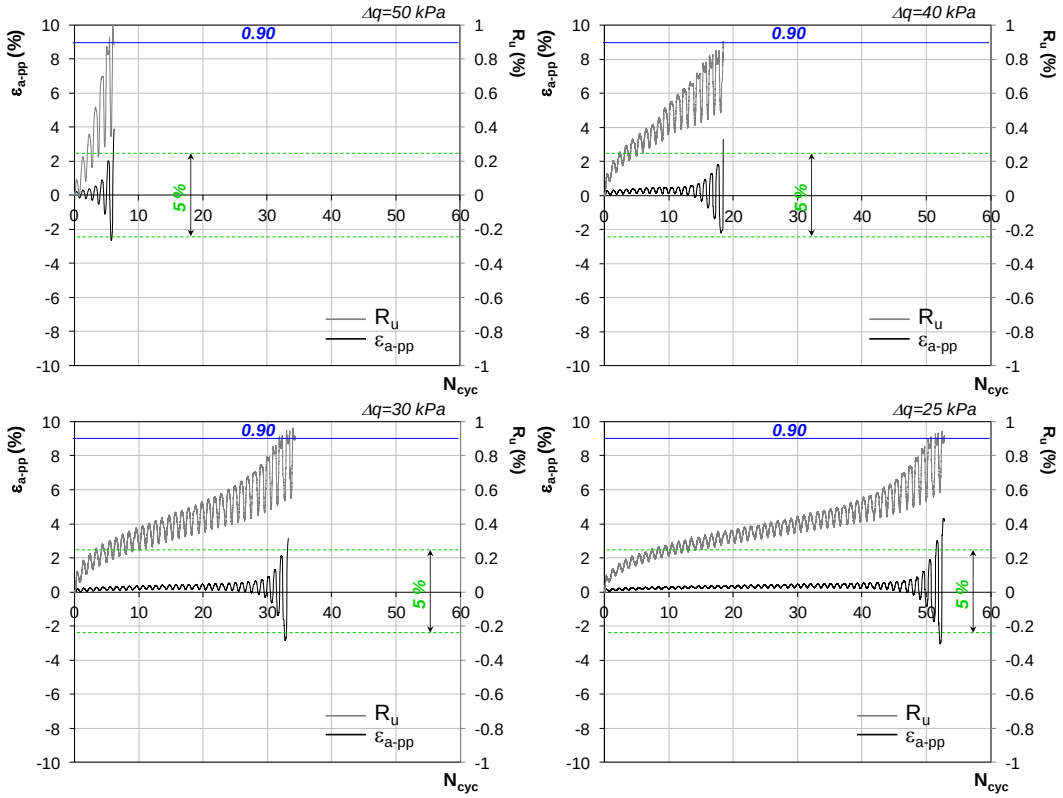

FIGURE V.13: CYCLIC AXIAL STRAINS AND PORE PRESSURE RATIO FOR RECONSTITUTED SILICA + ASH (SAR).

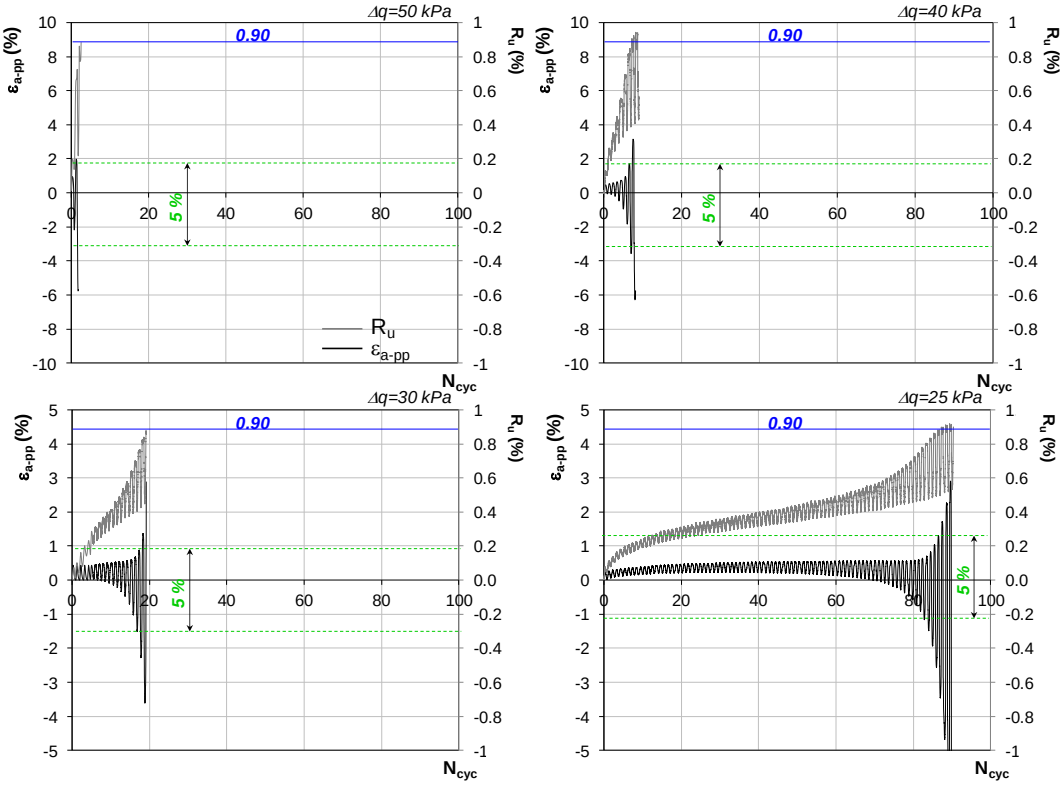

FIGURE V.14: CYCLIC AXIAL STRAINS AND PORE PRESSURE RATIO FOR RECONSTITUTED PUMICE + CLAY (PCR).

Based on the above reported results it is possible to evaluate the undrained cyclic resistance of the tested soils. It is generally defined as the normalized cyclic deviator stress, $\Delta q/2\sigma'_c$, required to cause liquefaction failure at a given number of cycles, N_{cyc}.

Figure V.15 shows the experimental relationship between cyclic stress ratio CSR and the number of cycle to cause liquefaction obtained for the different soil applying both strain and stress approaches.

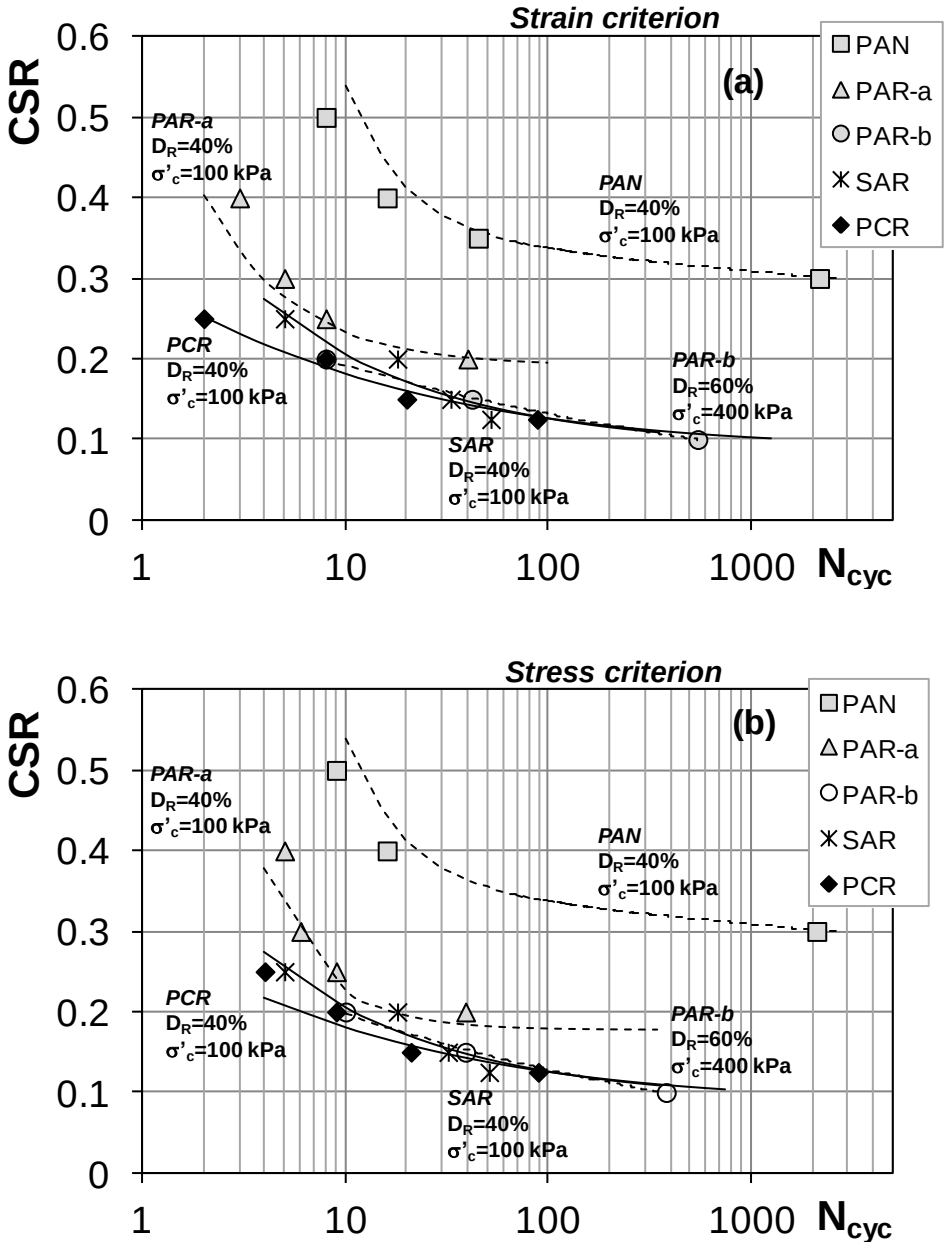

FIGURE V.15: UNDRAINED CYCLIC RESISTANCE CURVES WITH STRAIN CRITERION (A) AND STRESS CRITERION (B).

All the data describes similar trend: the smaller the amplitude of cyclic stress ratio, CSR, the higher the number of cycles to cause liquefaction. All the curves basically have a horizontal asymptotic trend at high number of cycles below which liquefaction cannot occur; the corresponding cyclic stress ratio represents the threshold stress below which no volumetric-distorsional coupling can occur.

A clear effect of fabric can be observed if comparing the cyclic stress ratio curves pertaining to natural and reconstituted soil at the same density and stress state: at equal relative density, the shear stress to liquefaction in 40 cycles increases of about 75% if reference is made to the natural soil response, PAN, rather than to the reconstituted one, PARa.

V.4.2 Effect of density

In order to highlight the effects of relative density on the liquefaction features of the reconstituted pumice + ash mixtures, the cyclic resistance curves of PARa (D_R=40%) and PARb (D_R=60%), are plotted in Figure V.16 and compared to the double strain amplitude, ε_a=5%, resistance curves measured on loose (D_R=50%) and dense (D_R=90%) silica Toyoura sand (black dots and squares), by Yamamoto et al. (2009), and that obtained on loose and dense pumice sand (red star and cross) by Orense & Pender (2013).

The cyclic resistance curves of Toyoura sand are markedly affected by the relative density of the samples: the CSR measured at a number of cycles equal to 100 on the dense samples is about twice that obtained on loose samples. This ratio is not constant since the slope of the curves is increasing with the relative density.

Also in the case of pumices loose specimens have gentler liquefaction resistance curves, while dense specimens have curves rising sharply as the number of cycles decreases. The effect of relative density that is very pronounced for Toyoura sand, appear to be not as remarkable in the case of pumices.

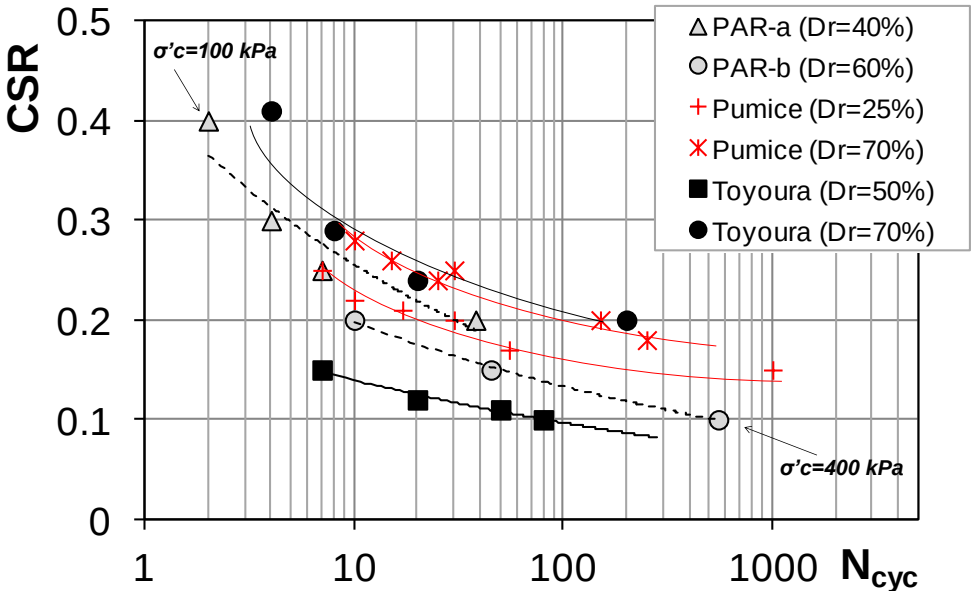

FIGURE V.16: COMPARISON OF DOUBLE AMPLITUDE CYCLIC RESISTANCE CURVES FOR TOYOURA SAND (YAMAMOTO ET AL., 2009), PUMICE SAND (ORENSE & PENDER, 2013) AND PUMICE+ASH SAND (PARA AND PARB).

The cyclic resistance curves measured on PARa and PARb reconstituted samples are in accordance with that of pumiceous soil: also in this case the relative density has no significant influence on liquefaction resistance of pyroclastic soil samples PARa and PARb. Neverthless the cyclic resistance of the reconstituted pyroclastic soil seems to be affected by the confining stress state since the CRS curve measured on PARb specimens, subjected to higher confining stress, shows a reduced variability of the cyclic resistance with the number of cycles, if compared to that of PARa. This behaviour may be addressed to a confining-pressure dependence of volcanic-crushable soils. In fact, as demonstrated by Orense & Pender (2013), the liquefaction resistance increases as the confining pressure decreases much more markedly as relative density increases (Hyodo et al.,1998).

V.4.3 Effect of FC

The effect of non plastic fine content on the liquefaction resistance has been evauated comparing the undrained cyclic curves of the reconstituted pyroclastic soil (PAR-a) with that of the pumices mixed with clay plastic fine (PCR), tested with the same fine content (F_C=30%), at the same relative density (D_R=40%) and effective confining pressure. The comparison is shown in figure V.15. The pyroclastic soil with

non-plastic fine is less liquefiable than the mixture of pumices with plastic fine: PARa is characterized by slightly higher CSR values respect to that triggering liquefaction on PCR soil samples at the same number of cycles. At low value of N_{cyc} the PARa requires a CRS value almost twice that needed to trigger liquefaction on PCR soil samples; as the N_{cyc} increases, such a marked difference between the cyclic resistance measured on PAR-a and PCR decreases.

The described results are in contrast with different literature findings, based on laboratory studies, aimed to evaluate the role of both fine content and its plasticity on liquefaction resistance.

As a matter of fact pumices with 30% plastic fine content, PCR, liquefies despite the finding of Ishihara (1993), Tokimatsu & Yoshimi (1983) which, on the basis of experimental results, respectively, classified sands containing more than 20% and 10% of clay as non-liquefiable. Furthermore the experimental results collected in the current study show that the cyclic resistance of soil with plastic fine decreases as plasticity increases. This result does not confirm the relationship suggested by Ishihara & Koseki (1989) and reported in Figure V.17 according to which an increase in the plasticity index consistently corresponds to an increases the CSR_{20} evaluated at N_{cyc}=20,

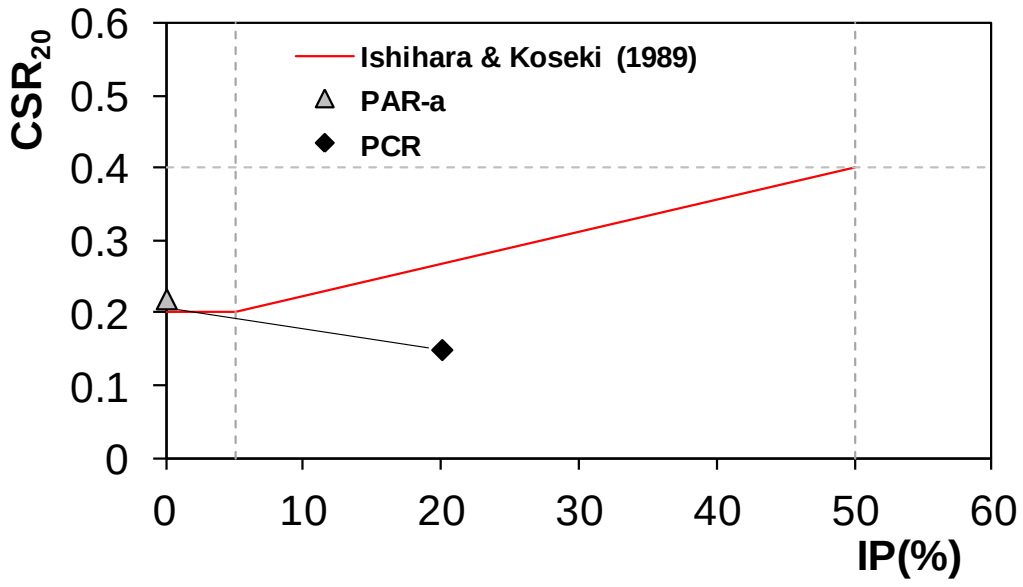

FIGURE V.17: INCREASE IN CYCLIC RESISTANCE WITH INCREASE IN PLASTICITY INDEX.

The decrease observed in the cyclic resistance exhibited by the PCR soil sample can be ascribed, somehow, to the effect of plasticity on factors that rules the undrained behavior of the soil. According to Prakash & Puri (2003) the addition of plastic clay in silty-sand mixtures may induce an increment in the buildup of pore water pressure because the clay fraction reduces the hydraulic conductivity of the soil.

Moreover, it has been demonstrated by Law & Ling (1992) that in the case of sand mixture with cohesive and non-cohesive fine the cyclic resistance is affected by the monotonic strength of the soil. In particular, CSR is a function of the so-called dynamic friction angle, φ'_d, which is measured as the slope of cyclic effective stress paths at liquefaction. It has been demonstrated that this dynamic friction angle is identical to that evaluated in monotonic tests , φ' (Law & Ling, 1992).

In Figure V.17 the dependence of cyclic liquefaction resistance on the strength parameters of the tested soil is shown. The CSR, evaluated for different N_{cyc} on PAR-a and PCR cyclic resistance curves, is plotted against the friction angle, φ', given by the relative monotonic triaxial tests.

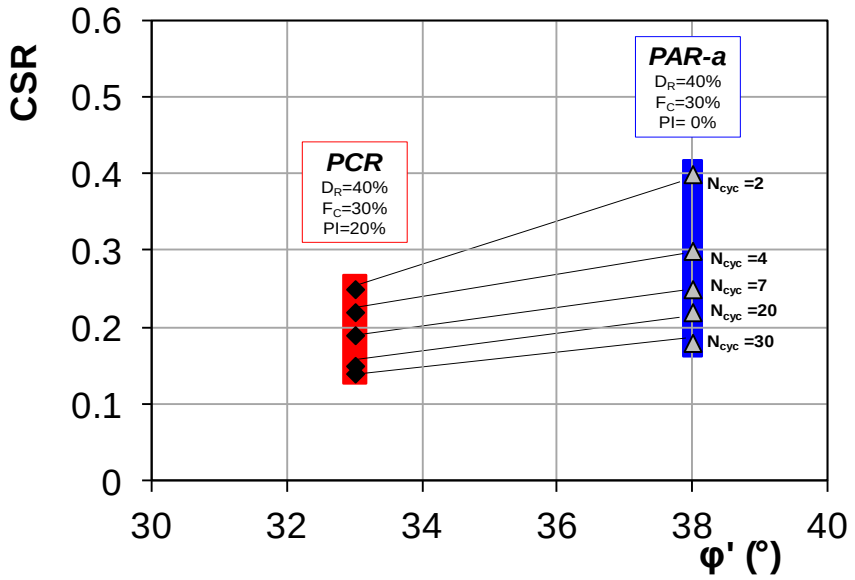

FIGURE V.18: CSR VERSUS φ'.

The results in Figure V.18, coherently with Law & Ling (1992) findings, show that, the different plasticity index of PARa and PCR soil samples, characterized by the same

grain distribution, relative density, fine content significantly affect their strength characteristics since the friction angle decreases from 38° to 33° degree as Ip increases. This, in turn, obviously influences the cyclic response. In particular, at a given number of cycles, CSR increases as the friction angle increases.

V.4.4 Effect of crushing

In order to define the effect of particles crushing on liquefaction resistance, in Figure V.15 the PARa cyclic resistance curve is compared with that of the hard-grained silica sand SAR, having the same grain size distribution, D_R and non-plastic ashy content.

The comparison between the PARa, PARb and SAR curves in Figure V.15 reveals no significant difference in terms of undrained cyclic resistance. This evidence highlights that the mineralogical origin of sand particles have a meaningless effect on cyclic resistance and also that probably no crushing occurred of the pumiceous particles during the cyclic shear, or, in other terms, that the possible crushing did not affect the liquefaction resistance, at least in the range of deviatoric stress applied in this experimental program.

To assess the occurrence of crushing during the cyclic tests, grain size distributions of material were determined before and after the tests.

In Figure V.18 the grain size distributions of sandy fraction of PARa, PARb and SAR untested and tested with CTX are illustrated. It can be noticed that no significant particles crushing is revealed by the comparison of grain size distributions. In particular, SAR grain size distribution of untested sand has perfectly the same shape of the tested SAR, confirming that no crushing occurs for hard-grained silica particles. On the contrary, slight differences are revealed between the grain size distribution of untested PAR and the other tested ones.

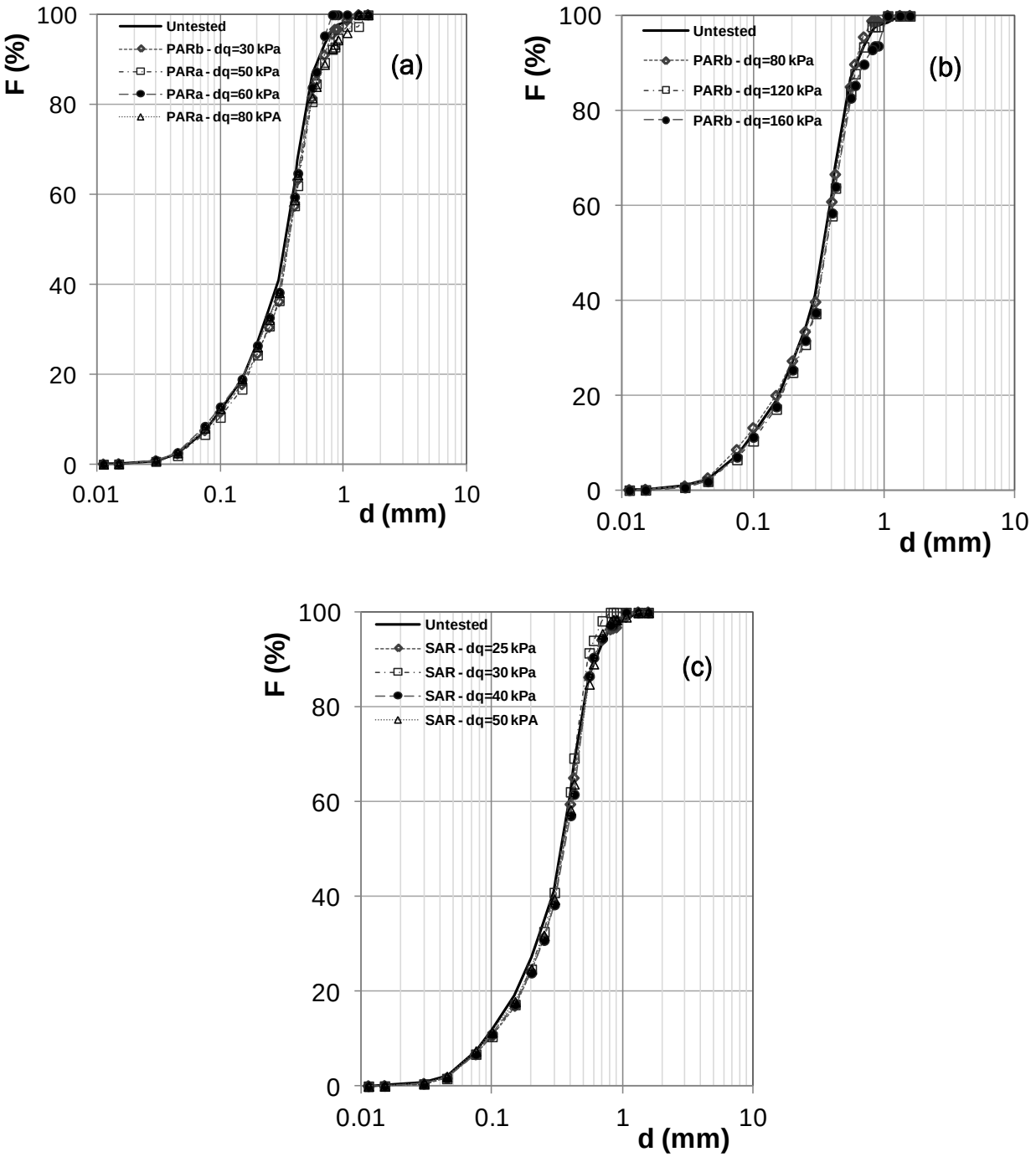

FIGURE V.19: GRAIN SIZE DISTRIBUTION BEFORE AND AFTER THE TESTS.

The degree of particle crushing after cyclic loading was also evaluated using a method originally proposed by Miura and Yamanouchi (1971). The method involves the quantification of the surface area of the particles defined by:

$$S_A = \sum \frac{F}{100} \frac{4\pi\left(\sqrt{\frac{d_1 d_2}{2}}\right)^2}{\frac{4}{3}\pi\left[\left(\sqrt{\frac{d_1 d_2}{2}}\right)^3\right]} G_s \gamma_s \qquad (V.1)$$

Where d_1 and d_2 are adjacent sieve sizes; F is the % by weight retained on the sieve; G_s is the specific gravity of the particles and γ_w is the unit weight of water.

In Figure.19, the surface area was calculated for PARa, PARb and SAR and for the virgin material and plotted against the cyclic stress ratio, CSR. Once again, no crushing is shown by the results in Figure V.20. In fact, all the dots lay on the initial surface area line evaluated on the virgin material.

The lack of significant breakage of PAR soil particles may be addressed to the high percentage of fine content, that may have 'amortized' the contacts between the asperities of sandy particles. Such an occurrence is revealed by comparing the results of PAR sand (F_C=30%) with pumice sand (F_C=0%) of Orense & Pender (2013) results for which it was demonstrated the greater is the CSR the higher is the aumont of crushing.

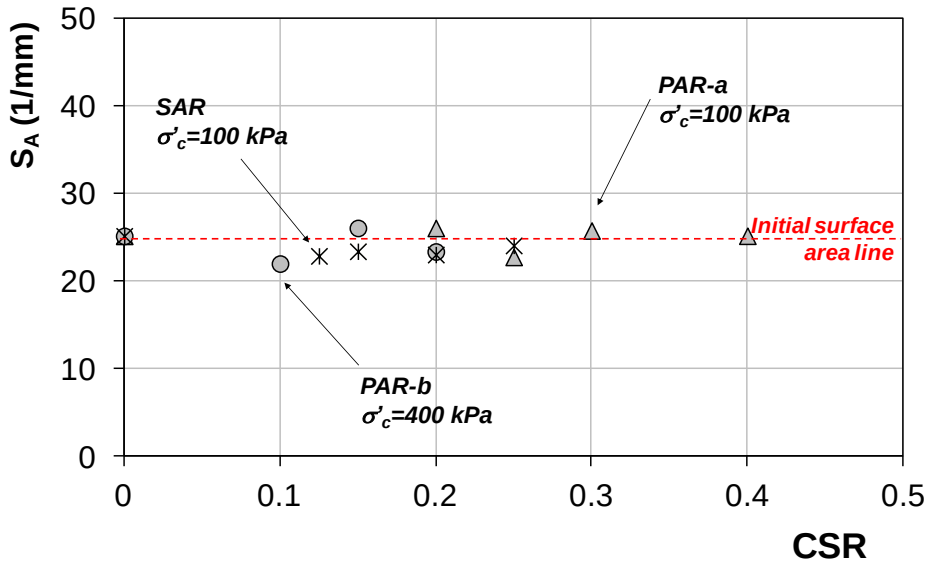

FIGURE V.20: GRAIN SIZE DISTRIBUTIONS (A); DEGREE OF PARTICLE CRUSHING BY SURFACE AREA OF PAR AND SAR (B).

V.5 Results of cyclic and dynamic torsional tests

Torsional tests just regarded the characterization of undisturbed samples (PAN) in order to characterize the dynamic properties of soil for the dynamic analysis.

Two tests were performed, where the value of mean effective stress, p'= 100 kPa, applied during the consolidation phase, was evaluated considering a k_0=0.5 (min value of Figure III.9b at the depth of sampling).

In Figure V.21a and V.21b, the results of two RCTS tests performed (RCTS1 and RCTS2) are illustrated in terms of normalized shear modulus, G/G_0, and the damping ratio, D (Figure V.21a), shear modulus, G, pore pressure, Δu (Figure V.21b), plotted with the strain amplitude, γ.

The general trend of the curves in the Figure V.21a e V.21b is typically divided into an approximately linear non-hysteretic behavior and non-linear hysteretic behavior. The stiffness and attenuation parameters strongly depend on particle type in terms of mineralogy and morphology, through the response at particle contacts, the elastic properties of the individual particles and the packing of the granular assembly (Silver & Idriss, 1971; Youd, 1972; Vucetic, 1994; Ladd et al. 1999).

The linear thresholds, defined at 5% decay of normalized shear modulus, shows very small strains. Below this threshold, the shear modulus corresponds to its maximum value, denoted as G_{max} or G_0 (Figure V.21b), and the damping ratio approximates to a minimum value, denoted as D_{min} or D_0 (Figure V.21a). In addition, no development of pore pressure, Δu, is detected (Figure V.21b).

Beyond the linear elastic threshold, denoted as γ_l, the onset of non-linear elastic behavior is shown. At medium strain levels, it has been demonstrated by Orense et al. (2012) and Senetakis et al. (2013) that the dynamic behavior of sands depends on the type of particles. The authors, comparing quartzitic granular materials and volcanic soils, revealed that soils of variable mineralogy and morphology of particles show markedly different macro-scale responses up to medium strain levels.

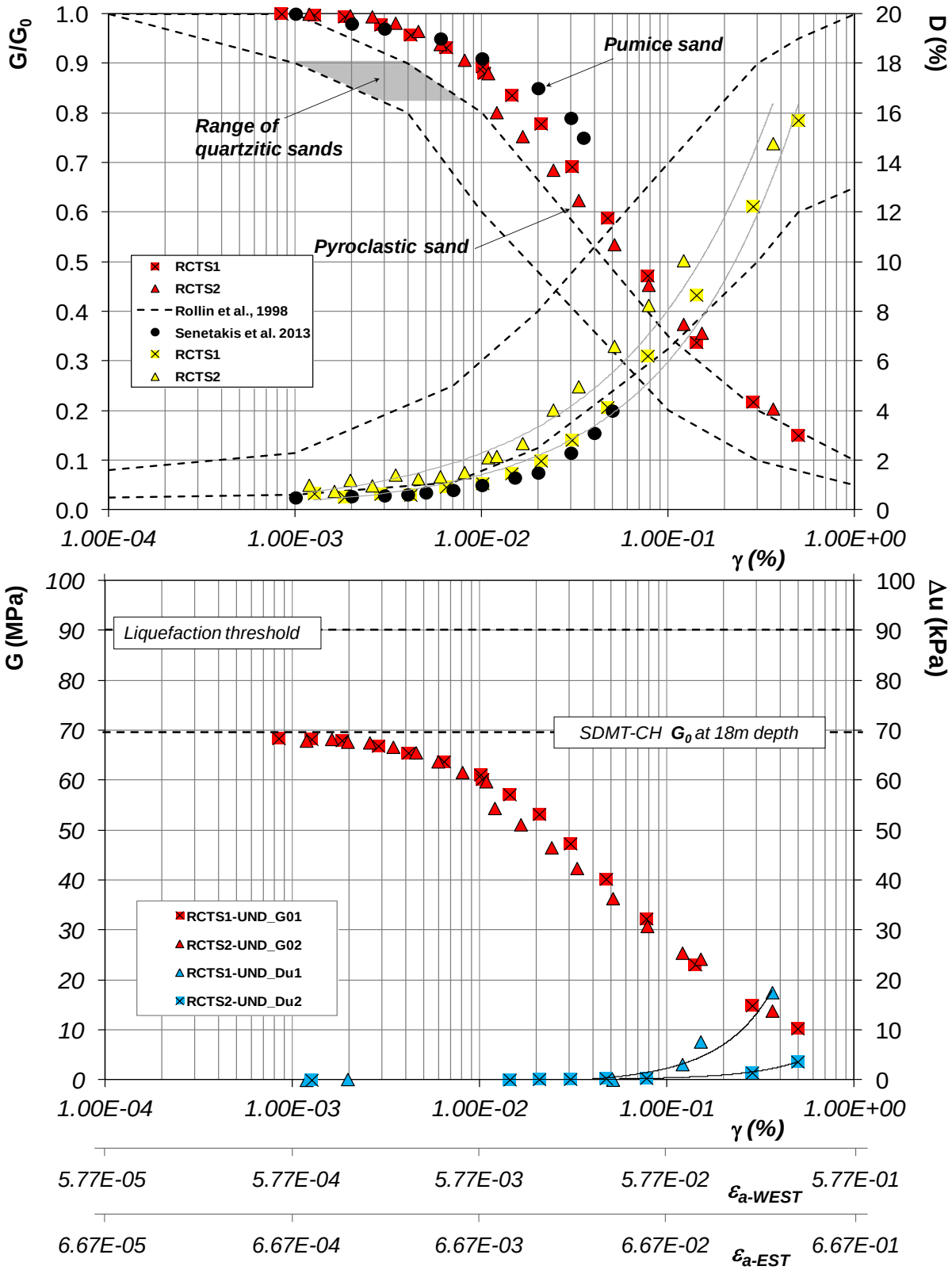

FIGURE V.21: (A) NORMALIZED SHEAR MODULUS, G/G_0, AND DAMPING RATIO, D; (B) SHEAR MODULUS, G, AND PORE PRESSURE, ΔU, VARYING WITH THE STRAIN AMPLITUDE, γ, ε_A.

Such a comparison is evaluated, in Figure V.21a, plotting the upper and lower bounds of G/G_0 and D curves proposed by Rollins et al. (1998) for quartzitic sands. The curves proposed by Rollins et al. do not describe satisfactorily the behavior of pumice soils of Senetakis et al. as well as the pyroclastic sand of this study. In fact, it can be seen that the plots are outside of the literature curves, with a remarkably more linear response of both the pumice sand and pyroclastic sand. Such an effect may be addressed both to the different mineralogy or texture of pyroclastic soils.

At higher strain levels, beyond the volumetric threshold, γ_v, the behavior of soils is markedly hysteretic non-linear; the shear modulus decreases while the opposite trend is observed for the damping ratio (Figure V.21a). At both medium and high strain levels, other mechanisms dominate the response of the volcanic soils. It is possible that micro-crushing at the asperities of the particles prevails during the cyclic loading, a micro-mechanism which prevents significant particles rearrangement and thus the reduction of shear stiffness and increase in damping is less pronounced in these soils (Senetakis et al., 2013).

During the RCTS tests, no significant pore pressures increments were registered (blue dots in Figure V.21b). Such a circumstance may be addressed to the lack of saturation condition (see §IV.3.2.1) as well as to the lack of the achievement of significant strain amplitude achieving high pore pressure values. The latter aspect is estimated by comparing the conventional value, ε_a=5%, adopted to define the liquefaction conditions with the final γ reached during RCTS tests. The comparison is evaluated by adopting two different criteria to reduce γ and ε in the same representation scale (Silvestri, 2001). The approaches are based on the equality of deviator stress and shear strain invariant; equality of maximum values of shear stress and strain.

The criteria, with the hypothesis of ε_v=0, gives the expressions:

$$\varepsilon_{a-WEST} = \frac{\gamma}{\sqrt{3}} \tag{V.3}$$

$$\varepsilon_{a-EST} = \frac{\gamma}{1.5} \quad \text{(V.3)}$$

In Figure V.21b, G and Δu are plotted in function of the different strain levels, γ, $\varepsilon_{a\text{-}WEST}$ and $\varepsilon_{a\text{-}EST}$. The last γ value achieved by Δu corresponds to $\varepsilon_{a\text{-}WEST}$=0.23% and $\varepsilon_{a\text{-}EST}$=0.27% which are very far from the conventional liquefaction threshold, ε_a=5%.

Critical analysis of semi-empirical approaches

VI.1 Introduction

For liquefaction assessment, in common practice, semi-empirical approaches based on literature charts are mostly used (e. g. Seed & Idriss, 1982; Idriss & Boulanger, 2004; Andrus & Stokoe, 2000).

The main advantage of such methods is a quantitative and synthetic estimation of liquefaction potential by performing three steps:

- Evaluation of the equivalent seismic demand at the site, expressed by the cyclic stress ratio (CSR);
- Evaluation of the resistance capacity of the soil under cyclic loads, expressed by cyclic resistance ratio (CRR);
- Comparison of CSR and CRR with the evaluation of Factor of Safety (FS=CRR/CSR).

The result of the assessment is strongly dependant on reliability of the choice of parameters determining both CSR and CRR.

The present chapter provides the results of the liquefaction assessment for the 'Riviera di Chiaia' site through semi-empirical methods, where CRR was determined by in situ investigations/tests, while CSR was calculated by a pseudo-static approach.

VI.2 Definition of cyclic stress ratio (CSR)

The well known Seed & Idriss (1971) procedure defines CSR by means of a pseudo-static approach with equation VI.1:

$$CSR_M = \frac{CSR_{7.5}}{MSF} = 0.65\left(\frac{\sigma_{v0}a_{max}}{\sigma'_{v0}}\right)\frac{r_d}{MSF} \quad \text{(VI.1)}$$

where:

- $a_{max}= a_g \cdot S_S \cdot S_T$ max horizontal acceleration;
- σ_{v0} and σ'_{v0} are vertical total and effective stress at the depth, z;
- r_d is the seismic reduction coefficient which takes into account the deformability of the soil column (r_d=1 when the soil column is rigid);
- MSF is a correction factor depending on magnitude, M_w.

The definition of CSR implies the choice of some parameters such as MSF and a_g; in the following, the influence of the definition of such parameters on CSR will be critically analyzed and, in particular, it will be studied how to combine their dependency on the seismic hazard. Moreover, the influence of the cyclic resistance curve on the definition of MSF will be discussed too.

VI.2.1 Magnitude scaling factor, MSF

According to Seed & Idriss (1982) simplified procedure, the values of $CSR_{7.5}$ calculated using equation VI.1 pertain to the equivalent uniform shear stress induced by a 7.5 magnitude earthquake. In order to apply equation VI.1 to any value of magnitude, $CSR_{7.5}$ can be adjusted introducing the magnitude scaling factor, MSF.

MSF is a correction factor that provides an approximate representation of the effects of shaking duration, or equivalent number of cycles, N_{eq}, which in literature is determined by two distinct way; based on: statistical assessment of case histories data showing liquefaction/non liquefaction field performance; comparison between the cyclic stress ratio and number of equivalent cycles curves developed on the basis of cyclic laboratory tests results.

The second approach is mostly adopted; on such a basis, the range of MSF-M_w curves reported in Figure VI.1 for liquefaction assessment was determined.

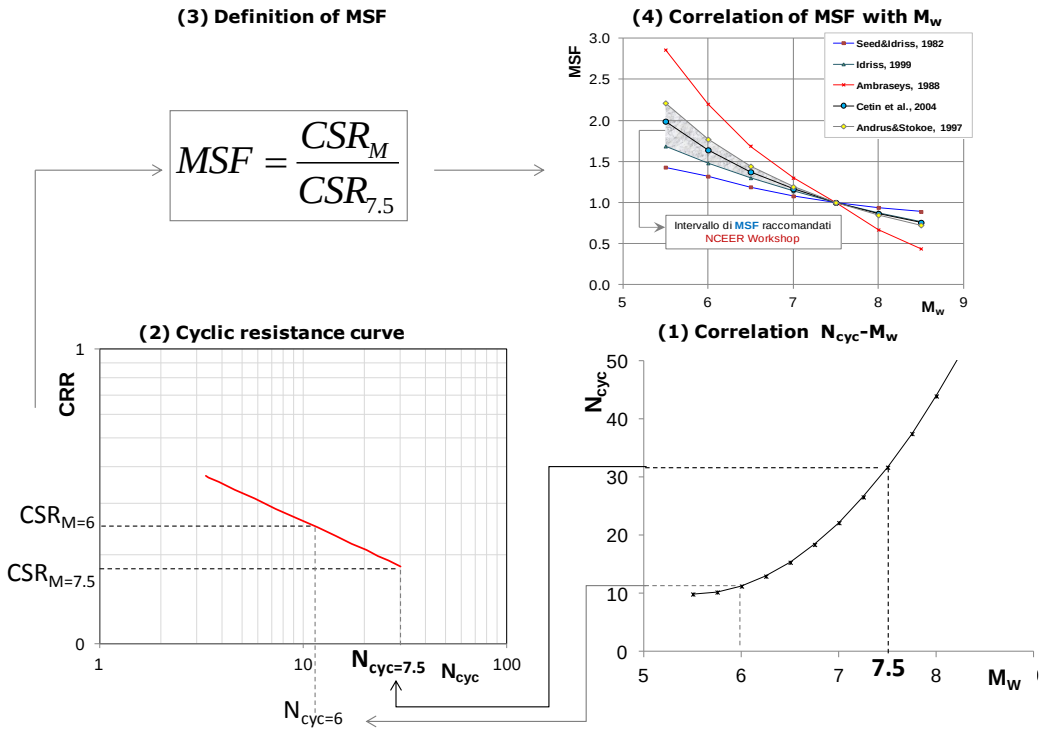

FIGURE VI.1: PROCEDURE TO DETERMINE MSF.

The approach based on laboratory curves, used here in the semi-empirical analysis, schematically reported in Figure VI.1, consists of the following procedure:

- (1) defining the correlation of the number of equivalent cycles, N_{eq}, versus either magnitude, M_w, or a combination of synthetic ground motion parameters;
- (2) determining experimentally the curve CSR-N_{cyc} (2) and the ratio MSF=$CSR_M/CSR_{7.5}$ (3);
- (4) correlating MSF with M_w, in turn.

Step (1) implies the conversion of an irregular seismic load to equivalent uniform cycles, N_{eq}. A wide range of conversion procedures is available for evaluating the equivalent number of cycles (Lee & Chen, 1972; Seed et al., 1975; Annaki & Lee, 1977; Valera & Donovan, 1977; Green, 2001; Liu et al., 2001; Biondi, 2002; Green & Terri, 2005). These procedures, however, are rather complex and their results strictly depend on the adopted conversion curve and on the techniques for choosing and counting the stress cycles that significantly affect the pore pressure build-up (Biondi et al., 2012). To bypass such conversion procedures, literature provides

simplified evaluations of N_{eq} as a function of synthetic parameters of seismic irregular history (see §VII.3) which were deduced by the application of conversion procedure to a wide set of seismic records.

In the present study, for step (1), N_{eq} was correlated to moment magnitude, M_w, by means of the three relationships shown in Figure VI.2.

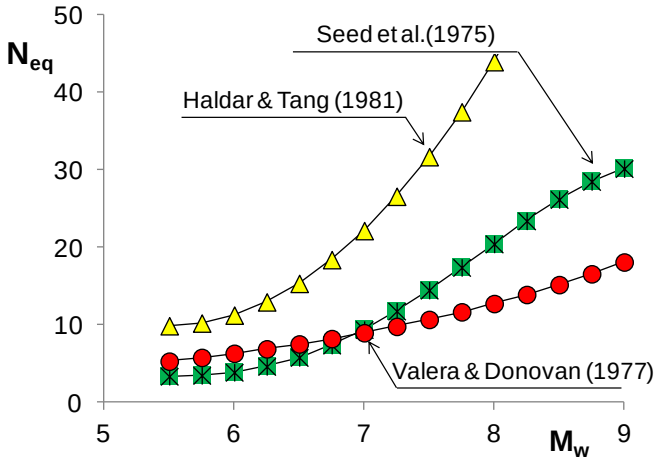

FIGURE VI.2: CORRELATIONS N_{EQ}-M_W.

For step (2), the cyclic resistance curve of intact pumice+ash mixture (PAN), reported in §V.5.1.1 based on the strain criterion, $\varepsilon_{a\text{-}pp}$=5%, was adopted. In addition, in order to evaluate the sensitivity of MSF to the cyclic resistance curve, the latter was defined by interpolating the experimental points with two different functions of the number of cycles, N_{cyc}: a power function and an hyperbolic function suggested by Park & Ann (2013).

The power function is mostly used in literature for the interpolation of cyclic resistance curve, but it does not provide a satisfactory representation of soil behavior; since there is no asymptotic threshold above which no accumulation of pore pressure develops; for such a reason, Park & Ahn (2013) curve was used too. The functions are respectively defined by equation VI.2 and VI.3:

Power function $$CSR = 0.5446 N_{cyc}^{-b} \quad \text{(VI.2)}$$

Hyperbolic function

$$\frac{(CSR - CSR_{min})}{(CSR_{ref} - CSR_{min})} = \left(\frac{N_{ref}}{N}\right)^{1/a} \quad \text{(VI.3)}$$

where:

- 'b' is the slope of the logCSR - logN_{cyc} curve;
- CSR_{ref} and N_{ref} are defined by a reference point of the curve;
- CSR_{min} corresponds to the asymptote;
- 'a' is inversely proportional to the slope of P&A curve.

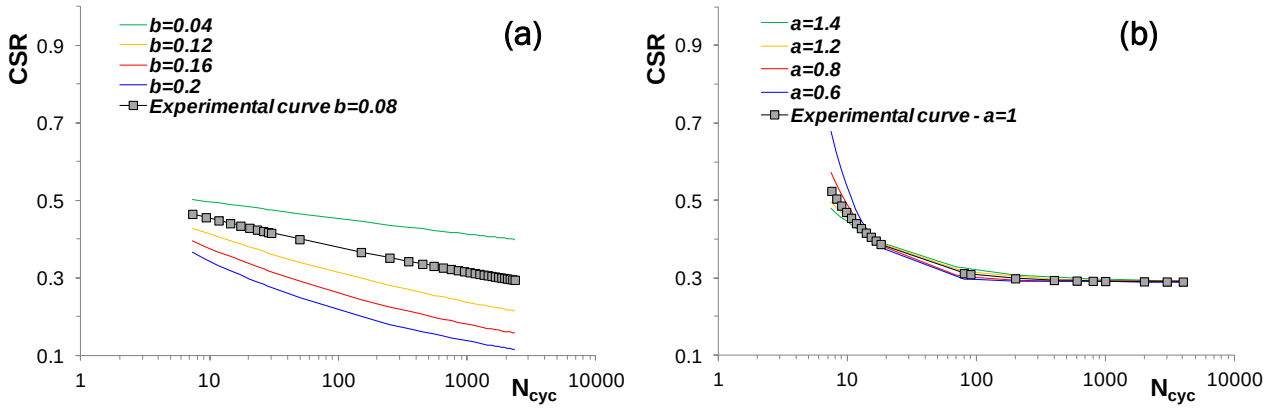

FIGURE VI.3: CYCLIC RESISTANCE CURVES PREDICTED BY THE POWER FUNCTION (A) AND HYPERBOLIC FUNCTION (B).

Figure VI.3 a-b reports the data point CSR against N_{cyc}, obtained by results of cyclic tests (square dots in Figure VI.3a and Figure VI.3b), interpolated respectively with power function and hyperbolic function. On the same charts, the curves are plotted varying the exponents 'b' and 'a', in order to evaluate also the effect of slope on the definition of MSF. The ranges of 'b' and 'a' were chosen around the values corresponding to the actual exponents, b=0.08 and a=1, of the experimental curve.

The value of MSF was thus calculated as the ratio $MSF=CSR_M/CSR_{7.5}$, where both the generic and the reference values of magnitude, M and 7.5, were estimated according to the Seed et al. (1975), Haldar & Tang (1981) and Valera & Donovan (1977) correlations presented in Figure VI.2.

For the final step (3), MSF was finally correlated and plotted against M_w in Figure VI.4.

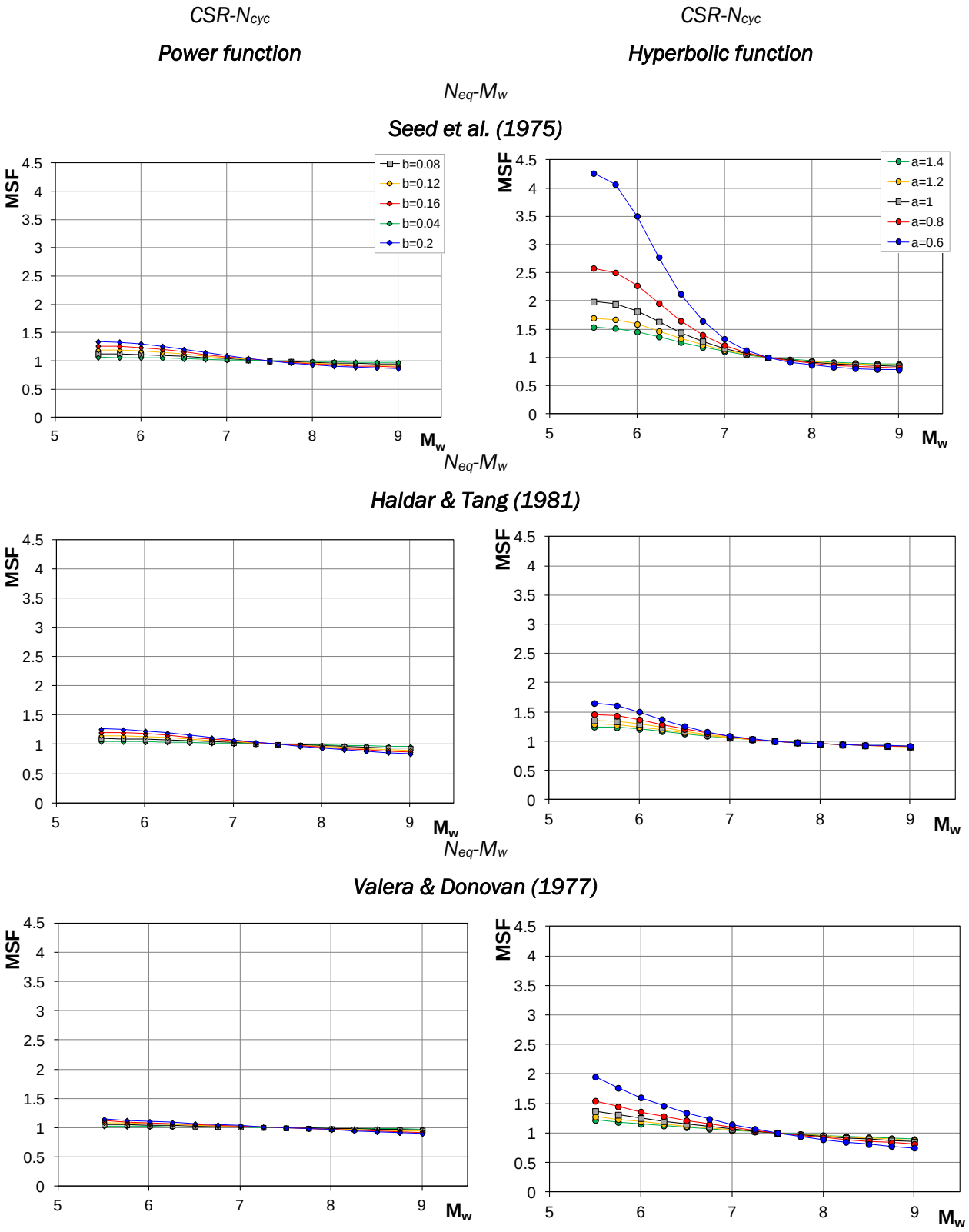

FIGURA VI.4: MAGNITUDE SCALING FACTOR, MSF, AGAINST MAGNITUDE, M_w.

It can be noticed that MSF, if evaluated with the power function, is slightly affected by both the slope of the curve (exponent 'b') and the correlation N_{eq}-M_w adopted: at M_w=5.5, MSF varies in the range 1.1-1.4; for higher M_w, the range of MSF becomes increasingly narrower. On the contrary, if MSF is calculated by the hyperbolic function by Park & Ahn (2013), at low M_w value, it shows a great sensitivity to the slope of the curve (exponent 'a'). Such dependence is markedly highlighted when the correlation by Seed et al. (1975) is used to convert the magnitude into the equivalent number of cycles. In this case, the range of variation of MSF is 1.5-4.25.

In order to calculate CSR using the MSF defined above, the curves in Figure VI.4 were interpolated with a sigmoid function defined in the equation:

$$MSF = g + \frac{h - g}{((1 + (s \cdot logM_w)^n)^m} \tag{VI.4}$$

In Table VI.1 and Table VI.2 the coefficients of sigmoid function are reported, respectively, for power curves and hyperbolic curves.

TABLE VI.1: COEFFICIENTS OF SIGMOID FUNCTION ADOPTED FOR THE INTERPOLATION OF POWER CURVES.

M_w-N_{eq} (Seed et al., 1975)					
b	0.2	0.16	0.12	**0.08**	0.04
h	1.348	1.277	1.201	1.150	1.073
g	0.805	0.804	0.847	0.938	0.969
s	1.227	1.245	1.244	1.055	1.039
n	32.633	32.633	32.632	15.183	15.356
m	0.308	0.310	0.298	4.702	5.817
M_w-N_{eq} (Haldar & Tang, 1981)					
h	1.272	1.277	1.159	1.124	1.061
g	0.804	0.804	0.475	0.907	0.951
s	1.242	1.245	1.271	1.019	1.015
n	32.633	32.633	32.032	12.434	12.417
m	0.309	0.310	0.077	3.902	3.913
M_w-N_{eq} (Valera & Donovan, 1977)					
h	1.163	1.252	1.183	1.128	1.062
g	0.803	-5.642	-8.606	0.701	0.849
s	1.262	1.248	1.216	0.729	0.738
n	32.633	5.392	5.305	4.237	4.388
m	0.312	0.039	0.022	2.573	2.524

TABLE VI.2: COEFFICIENTS OF SIGMOID FUNCTION ADOPTED FOR THE INTERPOLATION OF HYPERBOLIC CURVES.

M_w-N_{eq} (Seed et al., 1975)					
a	0.6	0.8	**1**	1.2	1.4
h	4.369	2.632	2.018	1.723	1.552
g	0.736	0.765	0.788	0.807	0.821
s	1.281	1.277	1.274	1.271	1.270
n	52.126	48.796	46.193	44.148	44.146
m	0.437	0.380	0.349	0.331	0.301
M_w-N_{eq} (Haldar & Tang, 1981)					
h	1.677	1.473	1.367	1.301	1.254
g	0.887	0.854	0.834	0.821	0.809
s	1.286	1.287	1.285	1.284	1.283
n	47.708	49.175	46.533	44.618	44.259
m	0.342	0.246	0.213	0.189	0.164
M_w-N_{eq} (Valera & Donovan, 1977)					
h	3.100	1.691	1.475	1.359	1.285
g	0.219	0.236	0.094	-0.178	-0.737
s	1.501	1.389	1.397	1.404	1.408
n	51.946	48.663	45.709	42.856	40.812
m	0.092	0.068	0.046	0.030	0.018

VI.2.2 Acceleration and magnitude of reference

According to the customary approach based on the probabilistic analysis (PSHA), adopted by the Italian Building code (NTC-08), the value of reference of the peak ground acceleration, a_g, is given by the combination of the limit state (related to a probability of exceedance, P_R), the return period, T_R, and the importance of the building, V_R.

For 'Riviera di Chiaia' site, the median hazard curve shown in Figure VI.5a provides the value a_g=0.168g, by assuming SLV (P_R=10%), T_R=475y and V_R=50y. The corresponding de-aggregation histogram is reported in Figure VI.5b, shows the distribution of the relative contribution, w, to the a_g of the magnitude - epicentral distance bins.

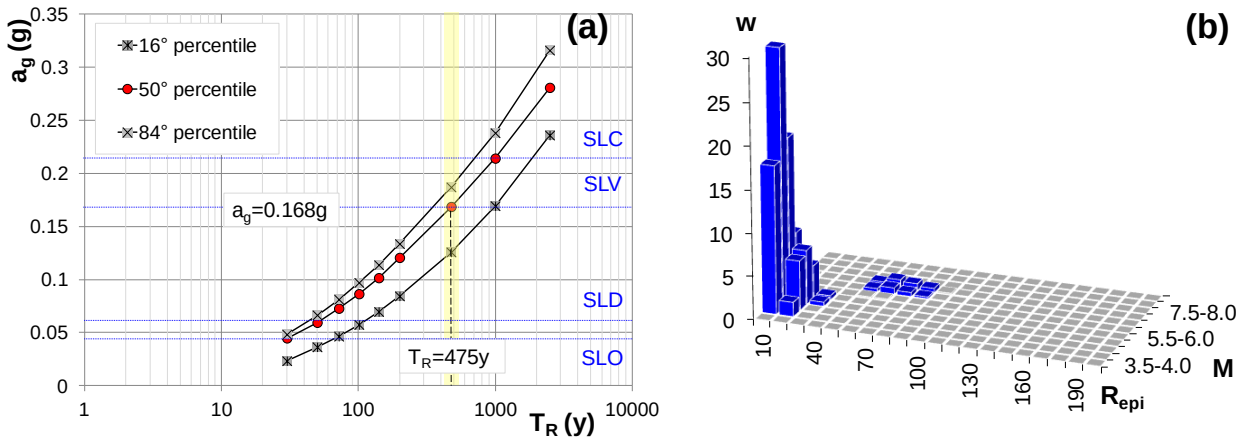

FIGURE VI.5: HAZARD CURVE (A) AND DE-AGGREGATION ANALYSIS (B) FOR 'RIVIERA DI CHIAIA' SITE.

The probabilistic approach, by which the site specific hazard curve is defined (Figure VI.5a), provides a_g as a function of the magnitude and site-source distribution distance of each seismic source interesting the site (Figure VI.5b). Such approach violates the basic hypothesis to calculate CSR, by Seed & Idriss simplified procedure, for which the acceleration and the magnitude reference are univocally related. In other words, the matter is the choice of the most representative value of magnitude, by which calculating MSF and, thus, CSR, to be associated to a_g, as given by the hazard curve.

A reasonable solution was firstly approached by Idriss (1985), who performed the probabilistic hazard analysis by directly implementing the value of MSF in the Ground Motion Prediction equation, provided by:

$$\lambda_{IM} = P\left[\frac{a_g}{MSF} > a^*_{g|M,R}\right] \nu = \left\{\sum_M \sum_R \left[1 - \phi\left(\frac{lna^*_g - ln\overline{\frac{a_g}{MSF}}}{\sigma_{lna_g}}\right)\right] f_M f_R \Delta m \Delta r\right\} \nu \qquad \text{(VI.5)}$$

where:

- ϕ is the log-normal distribution of acceleration (modified by MSF) characterized by the median value;
- $\overline{a_g}$, and standard deviation, σ_{lna_g}, given by the attenuation relation;
- a_g* is the value referred to the limit state of reference;
- f_M and f_R are, respectively, magnitude and distance distributions;

- ν is the annual frequency of occurrence of the earthquake.

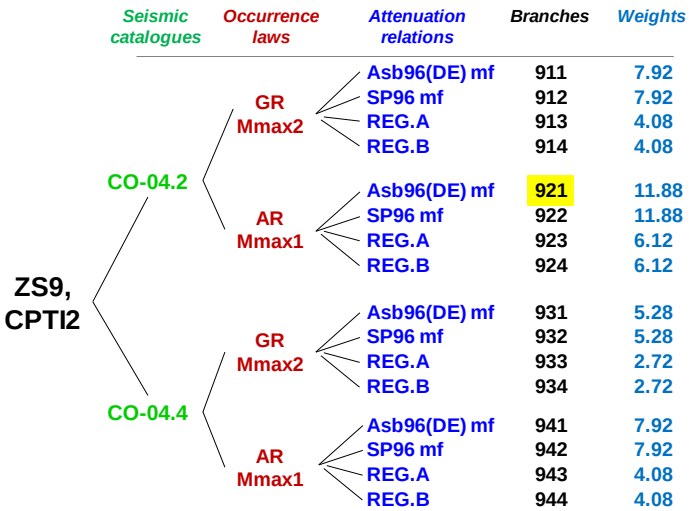

FIGURE VI.6: LOGIC TREE FOR THE PROBABILISTIC HAZARD ANALYSIS (WORKING GROUP MPS, 2004).

The implementation of equation VI.5, on one hand, provides a direct a_g value for the definition of CSR that takes intrinsically into account the contribution of the different potential magnitudes of all the seismic sources. On the other hand, it is not an easy task to define the seismic demand for the liquefaction assessment with a simplified approach (such as the semi-empirical one). In fact, a typical probabilistic hazard analysis is usually performed calculating equation VI.6 for each weighted branch of the so-called 'logic tree'; therein seismic catalogues, occurrence laws and attenuation relations are differently combined, as shown in Figure VI.6, in order to consider the epistemic uncertainty of input parameters (Workgroup MPS, 2004).

In order to overcome the difficulties of a rigorous probabilistic hazard analysis, a more suitable approach is hereafter proposed, called 'liquefaction-hazard method': a_g is evaluated, once again, in function of all the magnitude contributions (as the probabilistic hazard analysis provides) but, above all, it is not necessary to follow all the branches of the logic tree. In this case, only the branch #921 was considered since, the de-aggregation analysis is related to it.

The liquefaction-hazard method adopts basically the same expression of ground motion prediction equation (equation VI.5), but $\lambda_{IM\text{-}LIQ}$ is calculated by considering the

products of $f_M f_R \nu$ from the combination of the contributions, w, of de-aggregation histogram (Figure VI.5b) and a_g* corresponding to the 50° percentile of each return period, T_R, in Figure VI.5a.

Figure VI.7 shows the result of liquefaction-hazard method providing $\lambda_{IM\text{-}LIQ}$ against the acceleration level, a_g, and by using the three different MSF relationships proposed by literature.

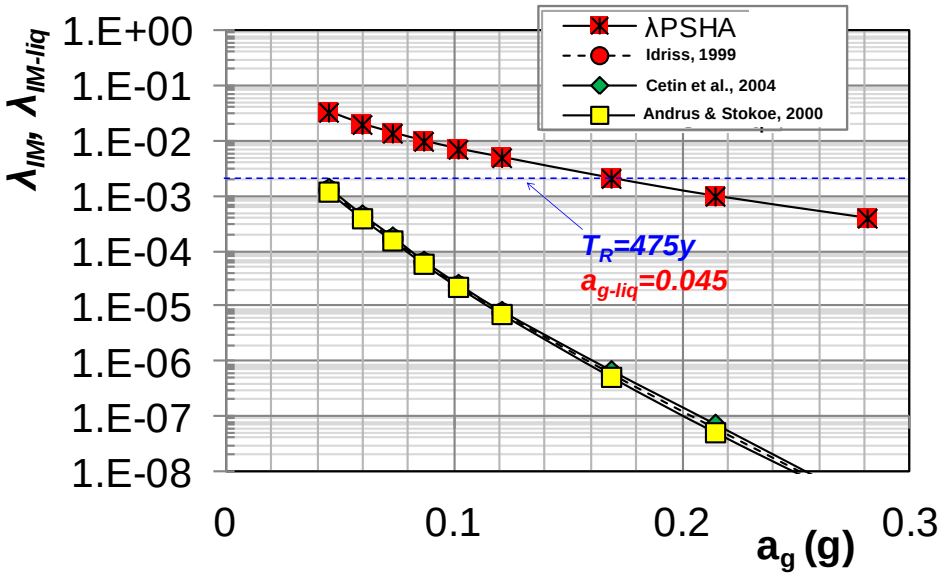

FIGURE VI.7: LIQUEFACTION-HAZARD METHODS WITH LITERATURE RELATIONSHIPS OF MSF.

For comparison, $\lambda_{IM\text{-}LIQ}$ was evaluated by adopting three MSF correlations proposed by Cetin et al. (2004), Andrus & Stokoe (2000) and Idriss (1999) relationships. On the same charts, the standard probabilistic hazard curve (λ_{PSHA}) is reported too.

For the case at issue, the $a_{g\text{-}liq}$ values to be adopt for the semi-empirical verifications were chosen for $\lambda_{IM\text{-}liq}$ corresponding to T_R=475y (λ_{IM}=0.0021). It can be observed in Figure VI.7 that the liquefaction-hazard curve evaluated is practically unaffected by MSF relationships provided by literature whichever is the value of annual frequency of occurrence, $\lambda_{IM\text{-}LIQ}$ or λ_{IM}.

$\lambda_{IM\text{-}LIQ}$ was also evaluated using MSF determined by the power function and hyperbolic function interpolating the CSR-N_{cyc} curve; where, the relation N_{eq}-M_w was determined through the correlations proposed by Seed et al. (1975), Haldar & Tang (1981) and Valera & Donovan (1977). In addition, in order to evaluate the sensitivity

of liquefaction-hazard curve to the slope of CSR-N_{cyc} curve, three different value of slope were considered: i.e. the value corresponding to the best fit of the exponent values of the experimental curve and those along with the minimum, the maximum possible value in the ranges considered in Figure VI.3.

Figures VI.8a-b show that the $\lambda_{IM\text{-}liq}$-a_g curves, evaluated with the MSF-M_w relationships based on power function, interpolating the cyclic resistance curve, is basically unaffected by the correlation N_{eq}-M_w adopted (Figure VI.8a). The same kind of observation may be done for the case of interpolating hyperbolic function except for Haldar & Tang relation in Figure VI.8b.

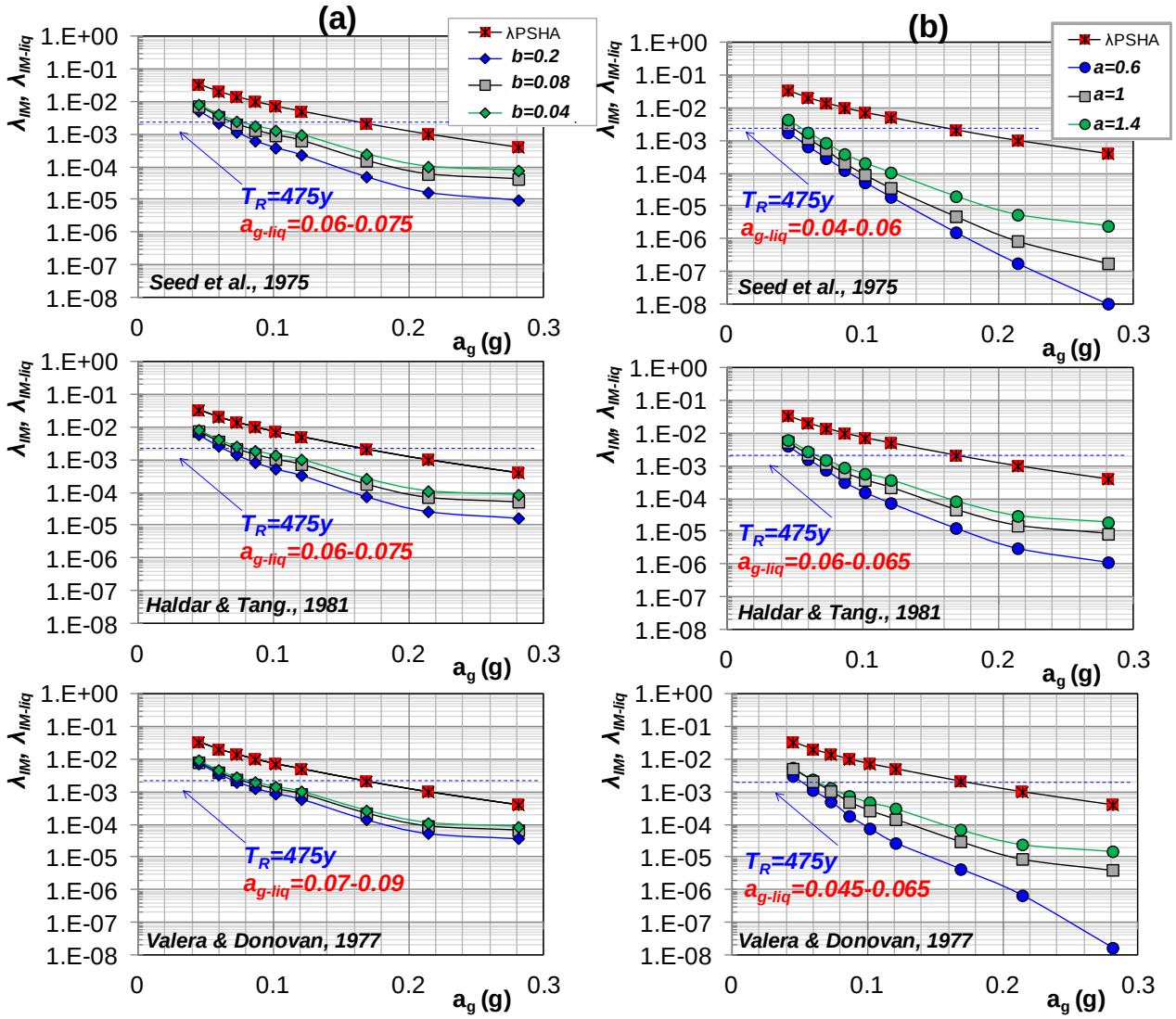

FIGURE VI.8: LIQUEFACTION-HAZARD METHODS WITH POWER FUNCTION-MSF (A) AND HYPERBOLIC FUNCTION-MSF (B).

The main factor affecting the $\lambda_{IM\text{-}liq}$-a_g curves seems to be the slope (exponents 'b' or 'a') of the cyclic resistance curve by which MSF was determined. As shown, once again, by Figure VI.8a-b, the lower the value of annual frequency of occurrence, $\lambda_{IM\text{-}liq}$, the greater the effect of slope on liquefaction-hazard curves. Such a dependence is much higher for hyperbolic rather than for power function interpolation.

VI.3 Definition of cyclic resistance ratio (CRR)

The cyclic resistance ratio of soil for the estimation of liquefaction potential was based on the charts applicable to Standard Penetration tests (SPT), Cone Penetration tests (CPT) and measurements of shear wave velocity, V_s.

The cyclic resistance ratio, CRR, was determined, in this case, on the basis of the results obtained from SPT, CPT, SDMT and CH tests.

Firstly, the procedure implied the correction of standard penetration resistance N_{SPT} for a hammer efficiency of 60% with the correction factors proposed by Youd et al. (2001). Secondly, corrected standard penetration resistance, N_{60}, cone resistance, q_c and V_s were transformed into a normalized values, i.e. $(N_1)_{60}$, q_{c1} and V_{s1}, respectively, for an overburden stress equivalent to the atmosphere (pa=1bar=98.1kPa) through the coefficients:

$$(N_1)_{60} = C_N N_{60} \qquad C_N = \left(\frac{p_a}{\sigma'_v}\right)^{0.784-0.0768\sqrt{(N_1)_{60}}}$$

$$q_{c1} = C_q q_c \qquad C_q = \left(\frac{p_a}{\sigma'_v}\right)^{1.338-0.294(q_{ciN})^{0.264}} \qquad \text{(VI.6)}$$

$$V_{s1} = C_V V_s \qquad C_V = \left(\frac{p_a}{\sigma'_v}\right)^{n} \rightarrow n = 0.25 \div 0.33$$

where:

- 'n' takes into account if the sand is clean or not and must be obtained by an iterative procedure in the first two cases;
- p_a is atmospheric pressure;
- σ'v is the effective vertical pressure at the z depth.

Finally, CRR was evaluated by means of the equations proposed by Idriss & Boulanger (2004):

$$CRR \cong exp\left[\frac{(N_1)_{60cs}}{14.1} + \left(\frac{(N_1)_{60cs}}{126}\right)^2 - \left(\frac{(N_1)_{60cs}}{23.6}\right)^3 + \left(\frac{(N_1)_{60cs}}{25.4}\right)^4 - 2.8\right]$$

$$CRR \cong exp\left[\frac{(q_{c1N1cs})}{540} + \left(\frac{(q_{c1N1cs})}{67}\right)^2 - \left(\frac{(q_{c1N1cs})}{80}\right)^3 + \left(\frac{(q_{c1N1cs})}{114}\right)^4 - 3\right] \quad \text{(VI.7)}$$

$$CRR \cong exp\left[0.022\left(\frac{V_{s1}}{100}\right)^2 + 2.80\left(\frac{1}{V_{S1c} - V_{S1}} - \frac{1}{V_{S1c}}\right)\right]$$

where:

- $(N_1)_{60cs}$ was modified for the percentage of fine content, F_c, as follow:

$$(N_1)_{60cs} = (N_1)_{60c} + \Delta N \qquad \Delta N = exp\left(1.63 + \frac{9.7}{F_c} - \left(\frac{15.7}{F_c}\right)^2\right)$$

- q_{c1N1} is calculated in function of the equations:

$$q_{c1N} = C_q \frac{q_c}{p_a}$$

$$F = \left[\frac{f_s}{(q_c - \sigma_v')}\right] 100$$

$$Q = \left[\frac{(q_c - \sigma_{v0})}{q_a} / p_a\right]\left[\left(\frac{p_a}{\sigma_v'}\right)^n\right] \quad \text{(VI.8)}$$

$$I_c = [(3.47 - logQ)^2 + (1.22 - logF)^2]^{0.5}$$

$$K_c = -17.88 + 33.75I_c - 21.631I_c^2 + 5.581I_c^3 - 0.403I_c^4$$

where the exponent 'n' is 0.5 if the sands are clean, otherwise 1.

- V_{s1c} is a critical value which is 215 if F_C<5; 200 if F_C>35. In other cases it is necessary a linear interpolation if 5<F_C<35.

CRR functions, as shown by equations VI.7, grow with increasing value of normalized parameters, $(N_1)_{60cs}$, q_{c1cs} and V_{s1} up to an asymptotic value which corresponds to

$(N_1)_{60cs}$=30, q_{c1cs}=180 and V_{s1}=215. Such values are usually adopted as thresholds above which a soil is not liquefiable.

In principle, only clean sands should be assessed with the above empirical procedures. Nevertheless, silty sand can be also considered if, in the expression of CRR, the effect of plastic fine is also introduced. For such a purpose, Eurocode 8 suggests that a soil with fines is not susceptible to liquefy in the cases of clay fraction > 20% with plasticity index > 10; and content > 35% and $(N_1)_{60}$>20. Indeed, as reviewed by Prakash & Puri (2010, 2012) and as described in §V.5.1.3, many uncertainties pertain to the effective role of both fine content and its plasticity. For such a reason, at 'Riviera di Chiaia' site section', CRR was evaluated assuming conservatively F_C=0% since the soil is essentially a silty sand with non-plastic fine.

Since CRR varies with effective confining stress and is affected by the presence of static driving shear, Seed (1983) recommended that to correct it for these effects by means of equation VI.9:

$$CRR = CRR \cdot k_\sigma \cdot k_\alpha \tag{VI.9}$$

in which K_σ is the overburden correction factor and K_α is the static shear stress correction factor. In the recent update of the semi-empirical field-based procedures reported by Idriss & Boulanger (2004), K_σ was revaluated in order to inter-relate the combined effects of D_R and σ'_v and the likely occurrence of particle crushing.

Sumarising, K_σ and K_α are given by:

$$k_\sigma = 1 - C_\sigma \ln\left(\frac{\sigma'_v}{p_a}\right) \tag{VI.10}$$

$$k_\alpha = a + b exp\left(\frac{-\xi_R}{c}\right) \tag{VI.11}$$

where:

- C_σ is a function of $(N_1)_{60}$ or q_{c1N};

- a, b, c are coefficients dependent on the ratio of static shear stress and effective vertical stress;
- ξ_R is a function of D_R and mineralogy of soil.

In this study, it was assumed conservatively K_α=1, while K_σ factor, that is normally applied to the CRR according to equation (VI.9), was used to convert the site the predicted CSR to an equivalent scaled value. This was accomplished by assuming:

$$CSR = 0.65\left(\frac{\sigma_{v0}a_{max}}{\sigma'_{v0,}}\right)\frac{r_d}{MSF \cdot k_\sigma} \qquad \text{(VI.12)}$$

In Figure VI.9, the values of the normalized N_{SPT}, q_c and V_s measurements at the site under study are plotted against the depths that relevant to the sampling of the tested material highlighted in yellow area. On the same plots, the threshold values above which the soil cannot liquefy are shown with the red lines.

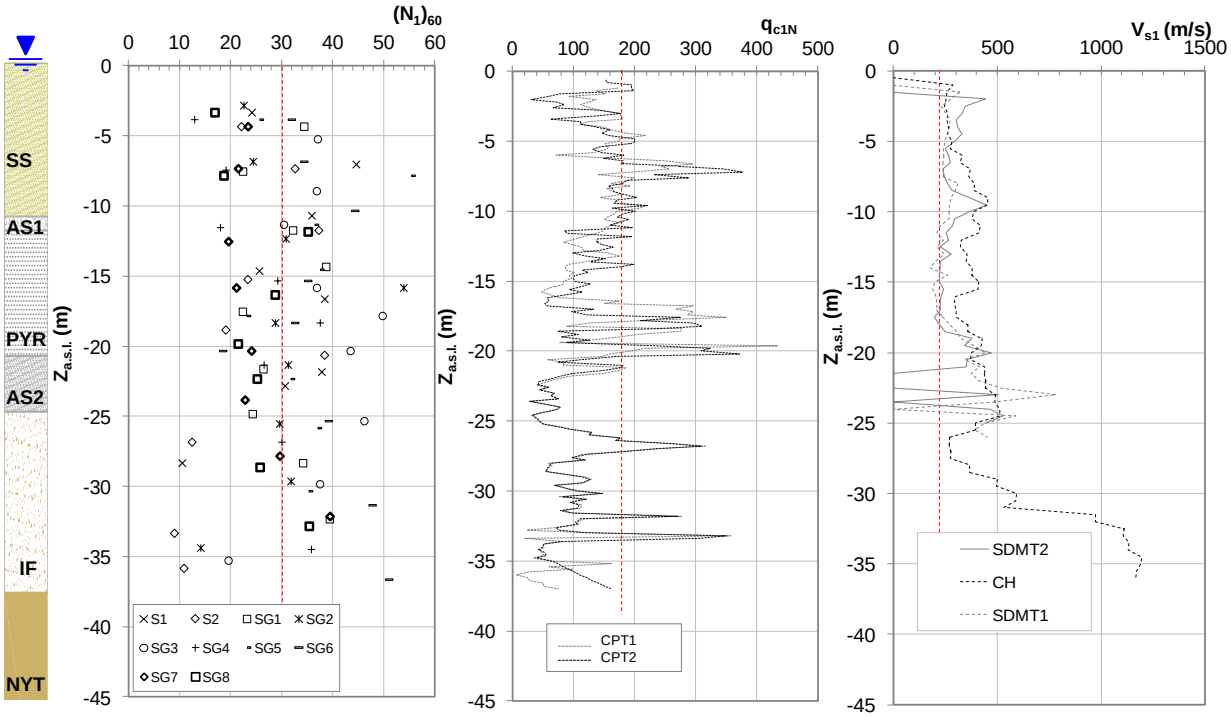

FIGURE VI.9: NORMALIZED PROFILES.

VI.4 Liquefaction assessment

The final step of the semi-empirical method is the comparison of CSR with the limit CRR usually reported on the literature charts (Idriss & Boulanger, 2004; Robertson & Wride, 1998; Andrus & Stokoe, 2000).

In this case, the assessment was carried out by defining CRR as a function of the normalized parameters, $(N_1)_{60cs}$, q_{c1cs} and V_{s1}, corresponding to a range of 1m around the sampling depth (17.5m<z<18.5m).

On the other hand, CSR was calculated adopting MSF by relationships proposed by literature (Cetin et al., 2004; Andrus & Stokoe, 2000; Idriss, 1999) and MSF computed by means of equation (VI.4) for the cyclic resistance curve of intact pumice+ash (PAN). The following different appoaches were considered:

- CSR determined as a function of the modal, average and maximum value of M_w (respectively, M_{mod}, $M_{average}$, and M_{max}), provided by de-aggregation histogram in Figure VI.5b, considered in both MSF and in the deformability reduction coefficient, r_d, (Idriss & Boulanger, 2004);
- CSR determined directly as a function of $a_{g\text{-}liq}$ evaluated, by the 'liquefaction-hazard' method ($PSHA_{\text{-}liq}$) and reduced by r_d (Idriss & Boulanger, 2004) corresponding to M_{ave};
- CSR evaluated by means of the safety factor ($F_{S\text{-}w}$) weighted for the contributions, w, provided by the de-aggregation histogram according to the following equation:

$$CSR = \frac{CRR}{\sum_i w_i \frac{CRR}{CSR(M_i)}}$$

- whatever the case, CSR was evaluated as a function of a_g multiplied by the stratigraphic amplification coefficient, S_s=1.46 (soil class C).

The results are shown in Figures VI.10-12, where CSR, determined in accordance with the above different methods, is plotted against the normalized parameters

$(N_1)_{60cs}$, q_{c1cs} and V_{s1}. On the same charts, the limit curves of CRR, was a function of the same parameters are plotted, in order to separate the data points relevant to liquefaction (above) and non-liquefaction conditions (below).

For semplicity, the assessment was performed only for q_{c1N} determined by CPT1, and for V_{s1} only from SDMT1 test, since CPT1 and CPT2 profiles are approximately equal as well as SDMT1, SDMT2 and CH profiles (Figures III.12).

In general, the comparison between the charts in Figures VI.10-11 highlights a significant dependence of the assessment on the MSF value adopted to scale CSR.

In all the charts, it can be noted that CSR evaluated by M_{mod}, $M_{average}$ and F_{s-w} are basically equal; on the other hand, $PSHA_{liq}$ provides lower CSR values, especially in Figure VI.10 where MSF was calculated with the power function interpolating the cyclic resistance curve.

In Figure VI.10, It is shown that CSR based on literature MSF provide the less conservative results, except for M_{max}, since the data point relevant to F_{s-w}, M_{mod}, $M_{average}$ and $PSHA_{liq}$ are lower than the other cases (Figure VI.10 and Figure VI.12).

In whatever the approach, in all the charts in Figures VI.10-12, it can be noticed that the verifications based on V_{s1} are always satisfied, assessing no potential risk for the site. Referring to SPT and CPT tests, liquefaction occurs for the lowest value of $(N_1)_{60cs}$ and q_{c1cs} in all the cases when CSR is evaluated with M_{max}. In Figure VI.11, it is also shown liquefaction occurring for the lowest q_{c1cs}, when CSR is evaluated by M_{mod}, $M_{average}$ and F_{s-w} (Figure VI.10). Such results may be, somehow, explained by the study of Rippa & Vinale (1983), who concluded that the shear strength of pyroclastic soils is underestimated by penetrometric tests because of the breakage of particles induced by the procedure.

The synthesis of parameters used in the verification is reported in Appendix 2.

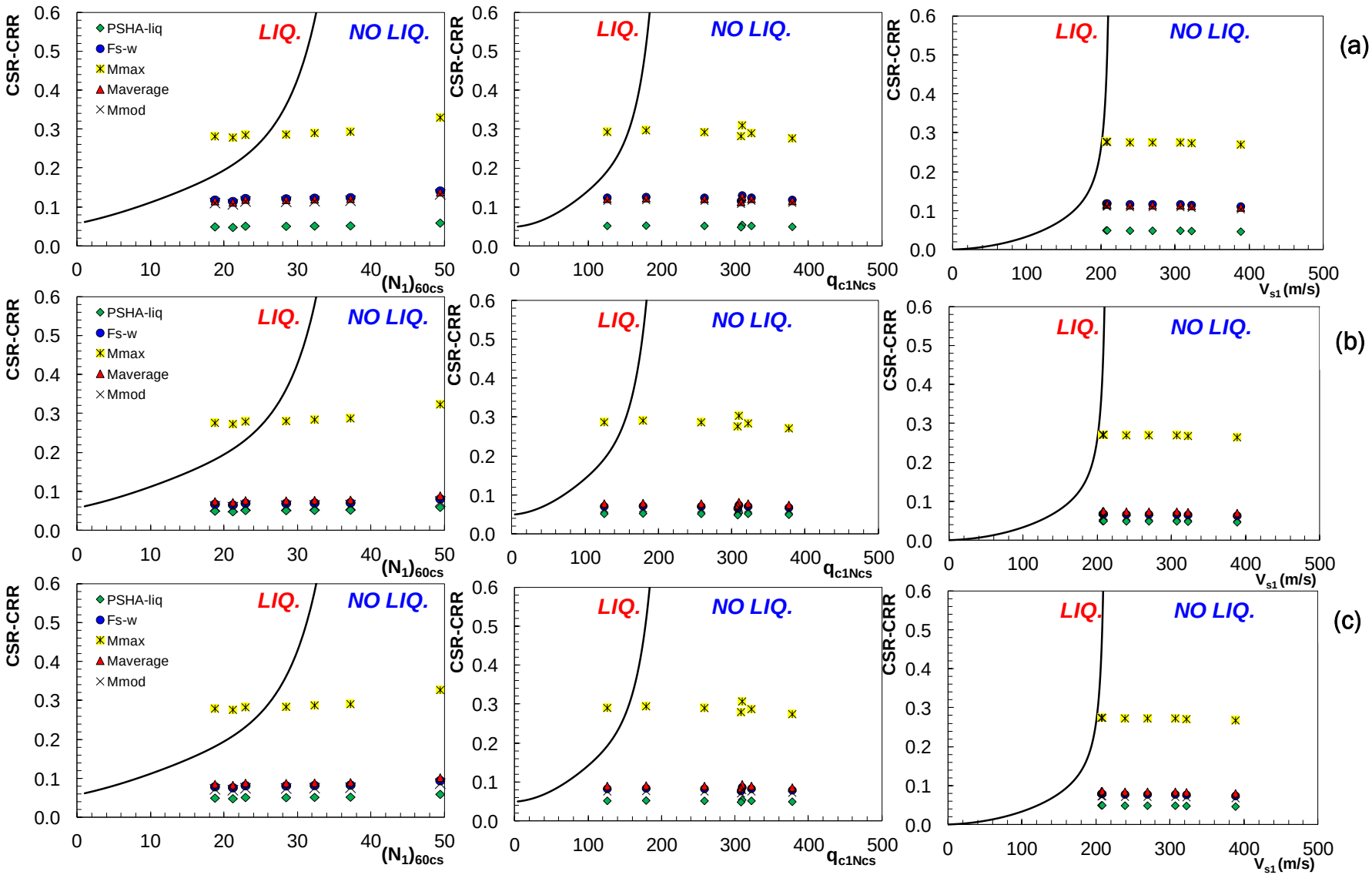

FIGURE VI.10: RESULTS OF VERIFICATION BY MEANS OF (A) IDRISS (1999) MSF RELATIONSHIP; (B) ANDRUS & STOKOE (2000) MSF RELATION AND (C) CETIN ET AL (2004) MSF RELATION (C).

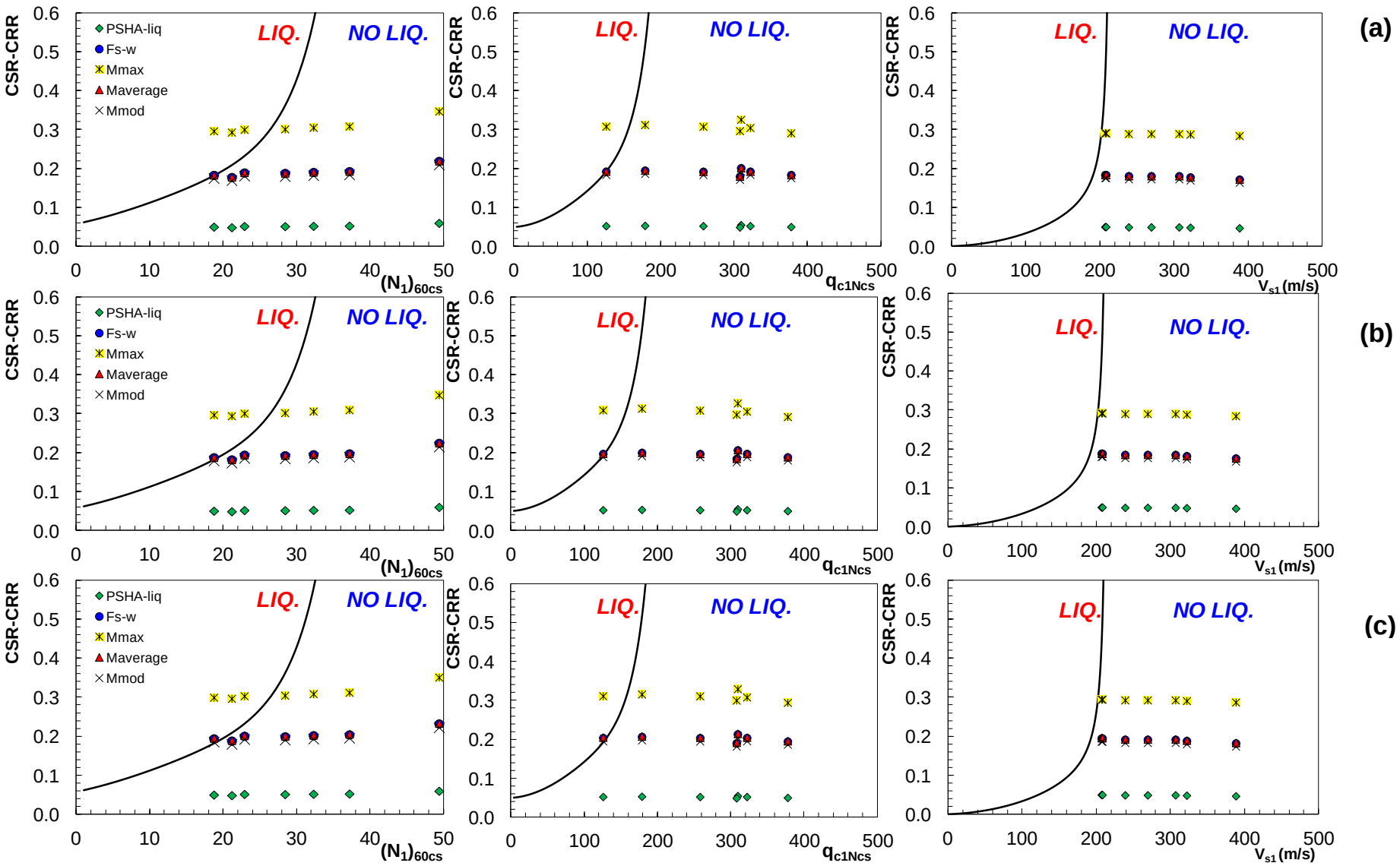

FIGURE VI.11: RESULTS OF VERIFICATION BY MEANS OF PW-MSF RELATIONSHIP; (A) SEED ET AL., 1975; (B) HALDAR & TANG, 1981; (C) VALERA & DONOVAN, 1977.

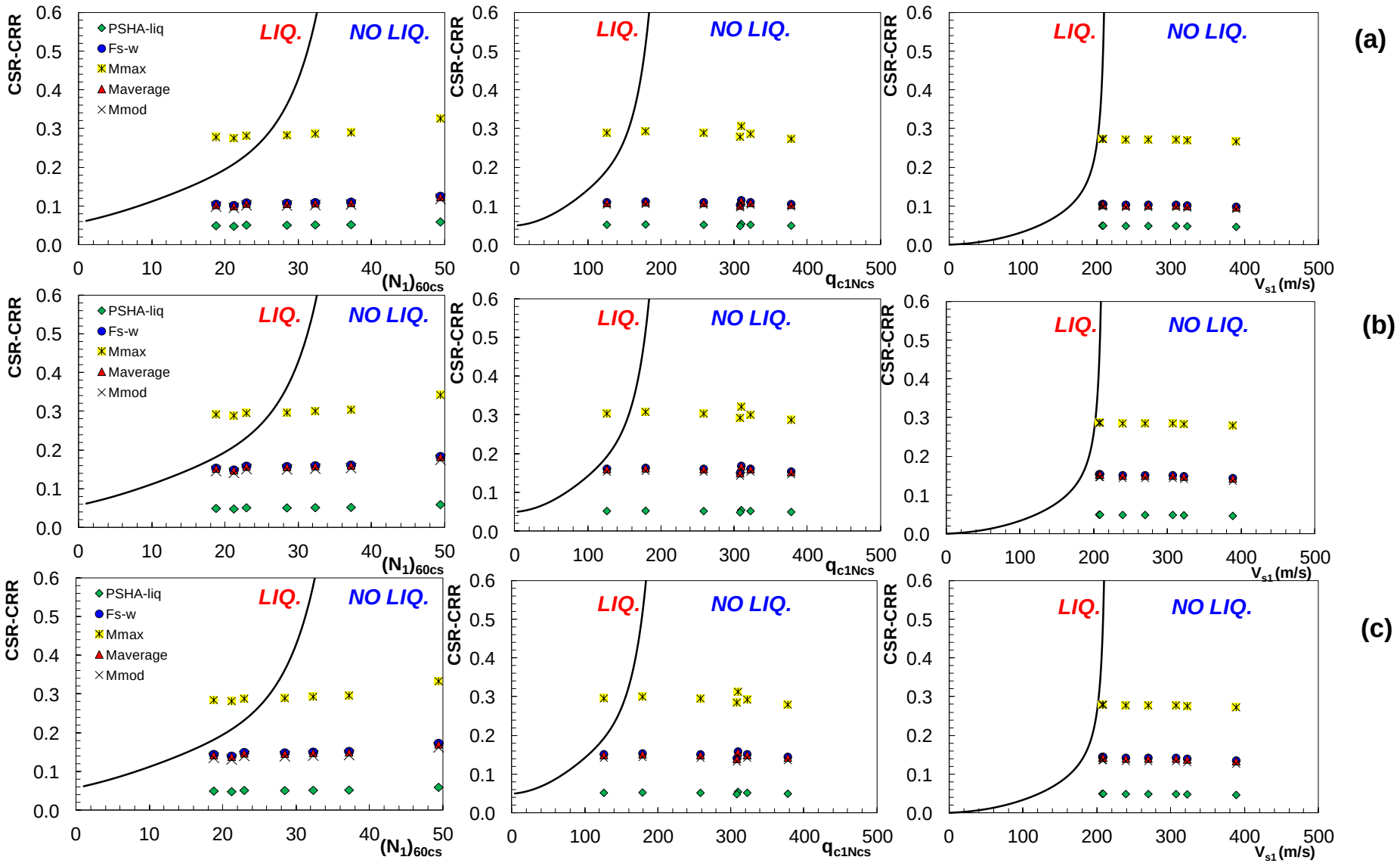

FIGURE VI.12: RESULTS OF VERIFICATION BY MEANS OF P&A-MSF RELATIONSHIP; (A) SEED ET AL., 1975; (B) HALDAR & TANG, 1981; (C) VALERA & DONOVAN, 1977.

Approaches based on dynamic analysis

VII.1 Introduction

Dynamic analyses can be performed fpr applying two different specific approaches to assess liquefaction potential:

- "Stress assessment method", inferring the maximum shear stress profile from the propagation of signals, in order to define the cyclic stress ratio, CSR, given by:

$$CSR = 0.65 \frac{\tau_{max}}{\sigma'_v} K_\sigma \qquad \text{(VII.1))}$$

  where τ_{max} is the maximum shear stress and σ'_v is the vertical effective stress at the depth of interest, already introduced in Section VI; *0.65* is the reduction coefficient. Then, CSR can be compared with soil resistance that, again, can be obtained from results of in situ tests (as shown in §VI.3) or from the cyclic resistance curve from laboratory tests;
- "Pwp assessment method", evaluating the pore pressure ratio, R_u, in order to compare it with the conventional threshold value 0.9 for liquefaction assessment;

In this study, the dynamic analyses were carried out by means of a decoupled approach and a coupled approach, implemented in the 1D time domain non-linear code SCOSSA (Tropeano et al., 2015). The code models the soil profile as a system of consistent lumped masses, connected by viscous dampers and springs with hysteretic behaviour. The stress-strain relationship is described by the MKZ model

(Matasovic & Vucetic, 1993) and the modified Masing rules (Phillips & Hashash, 2009).

In the decoupled approach, the shear stress-time history, was computed at specific depths by a total stress seismic response analysis. In the coupled approach, instead, an 1D effective stress analysis was performed by implementing a simplified pwp model in SCOSSA. In this case, excess pore water pressures were computed at each time step and the resulting reduction of effective stress and stiffness were taken into account in the response analysis.

To estimate the pore pressure build-up, the simplified method proposed by (Chiaradonna et al., 2015) was adopted. Such an approach permits to refer the earthquake irregular time-history of shear stress to the liquefaction resistance, this latter evaluated in laboratory by applying uniform series of cycles of shear stress to soil specimens. The comparison is expressed in terms of so-called 'damage' parameter, κ, that is an incremental function of the shear stress ratio, CSR, i.e. the shear stress normalized by either the mean effective confining pressure in a cyclic triaxial test or the effective vertical stress in a simple shear test. The damage parameter can be computed for any loading pattern avoiding equivalence criteria. The parameters considered in the model are:

- the steepness of the CSR-N_{cyc} curve (a) defined by the equation VI.3 of Park & Ahn (2013);
- the horizontal asymptote of the curve (CSR_t);
- the coordinates of a reference point of the cyclic resistance curve (N_r, CSR_r);
- in addition, it was necessary to implement the values the best-fitting relationship of R_u against the 'damage parameter', which reduces to N_{cyc}/N_L, available from experimental results, given by equation VII.2:

$$R_u = a \cdot \left(\frac{N_{cyc}}{N_L}\right)^b + c \cdot \left(\frac{N_{cyc}}{N_L}\right)^4 \quad \text{(VII.2)}$$

VII.1.1Seismic input and geotechnical model

The selection of seismic input used in dynamic analysis was performed through *REXEL* code (Iervolino et al., 2009) by which 5 spectrum-compatible accelerograms belonging to a range of $4.5<M_w<6$ and $0<R_{epi}<30$km, in accordance with de-aggregation analysis (Figure VI.5), were scaled at $a_g=0.168g$. The selected histories and the compatibility with target sprectrum are, respectively, illustrated in Figure VII.2a and Figure VII.2b.

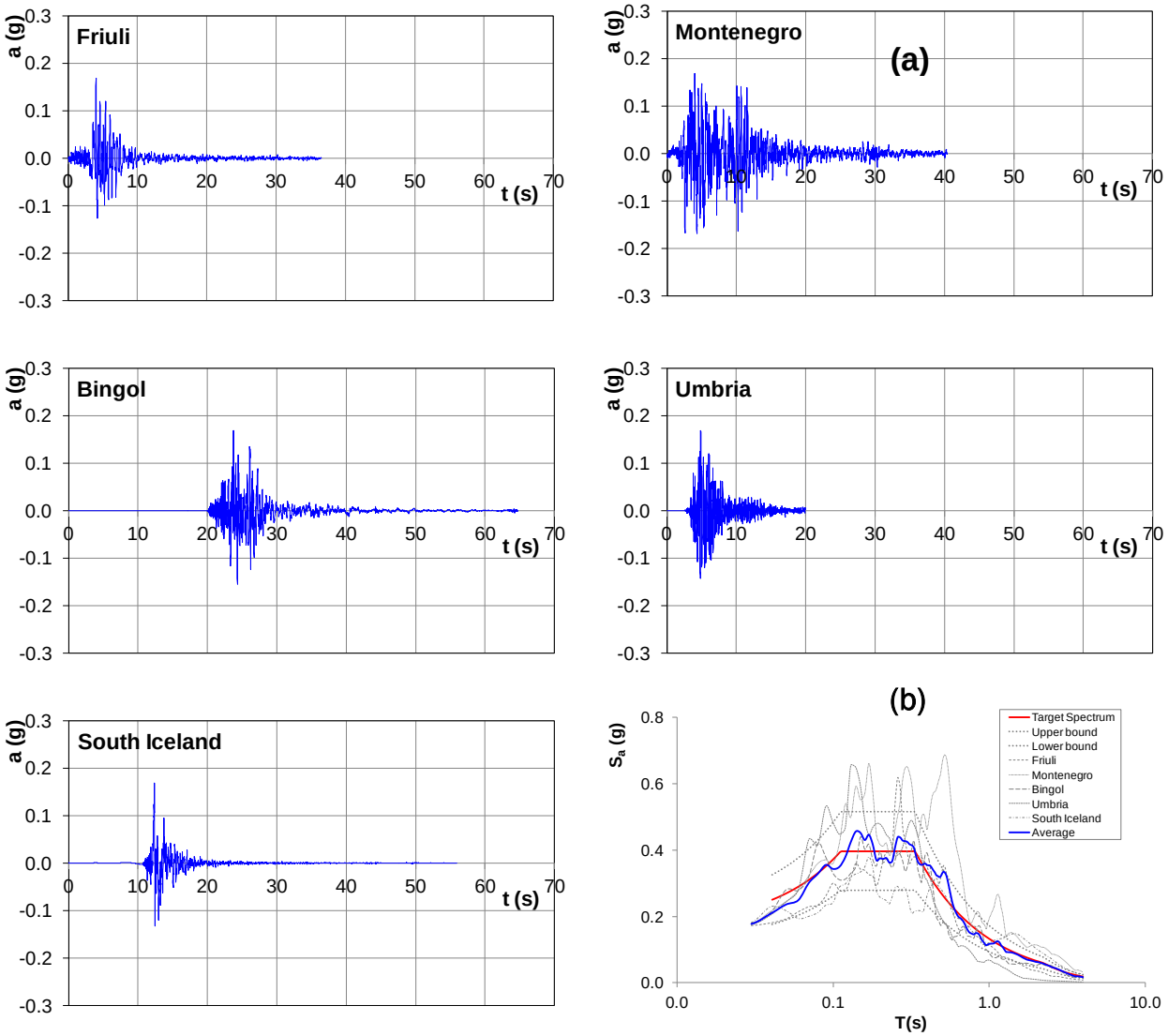

FIGURE VII.1: ACCELEROGRAMS (A) AND RESPONSE SPECTRUM (B).

The main features for the selected accelerograms, are reported in Table VII.1; all of them were recorded by European seismic stations on a stiff rock outcrop, i. e. a soil class 'A' according to the National Technical Code, in order to minimize the influence of local conditions of subsoil on amplitude, frequency content and duration of

signals.

TABLE VII.1: FEATURES OF SELECTED ACCELEROGRAMS

Station ID	Earthquake	Date	M_w	Fault Mechanism	Repi [km]	PGA (g)	EC8 Site class
ST539	Bingol	01/05/2003	6.3	strike slip	14	0.292	A
ST20	Friuli	06/05/1976	6.5	thrust	23	0.356	A
ST64	Montenegro	15/04/1979	6.9	thrust	21	0.181	A
ST236	Umbria Marche	06/10/1997	5.5	normal	5	0.187	A
ST2558	South Iceland	21/06/2000	6.4	strike slip	5	0.837	A

The shear wave velocity profile assumed (red line in Figure VII.2a), for the definition of the geotechnical model, was obtained by averaging in each soil layer the values of V_S inferred from the CH and both the SDMT tests.

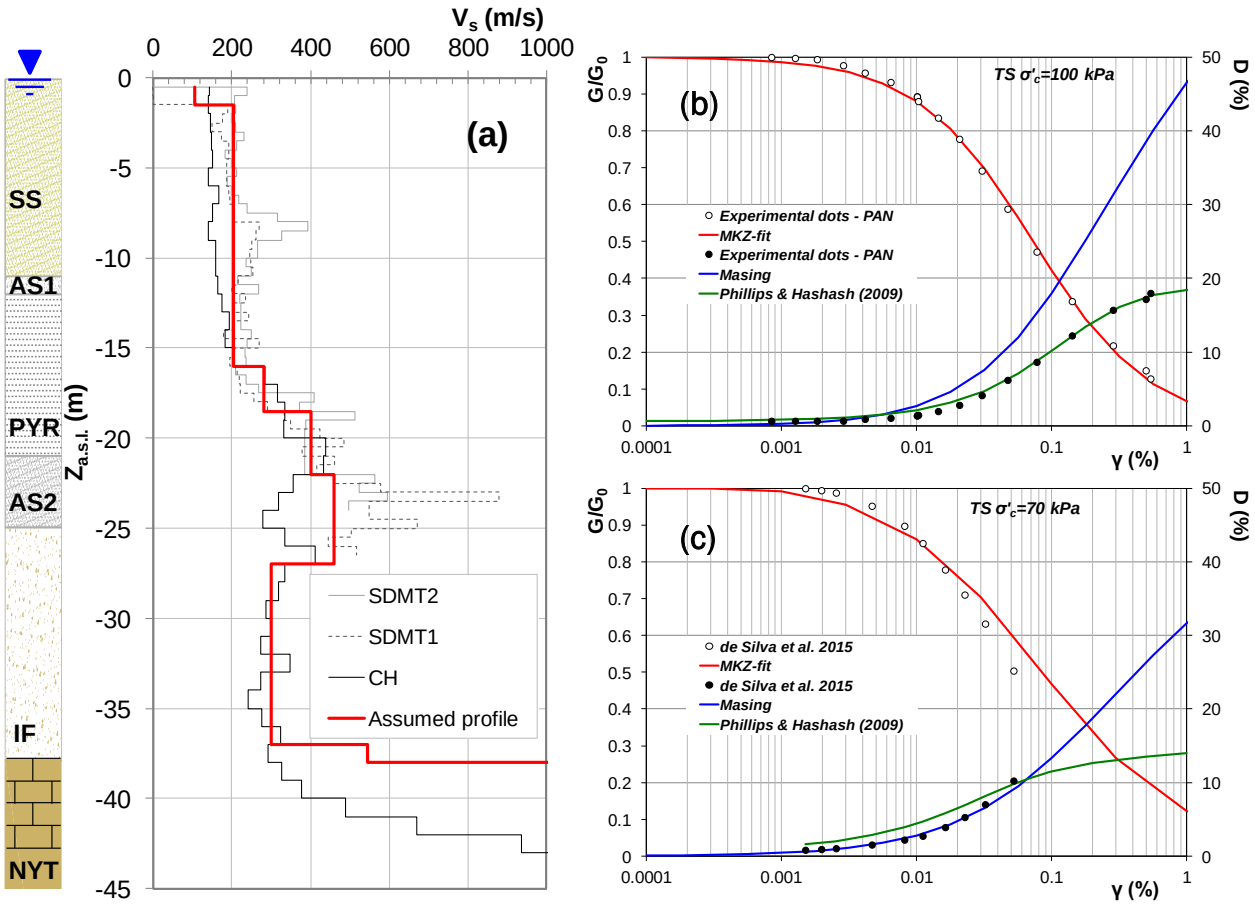

FIGURE VII.2: SHEAR WAVE VELOCITY PROFILE (A); SHEAR-DEPENDENCE OF THE EQUIVALENT PARAMETERS FROM LABORATORY TESTS ON PYROCLASTIC SANDS (B) AND SEASHORE SANDS (C).

Non linear properties of the volcanic materials (ASH1, PYR, ASH2 and IF in Figure VII.2a) were described by adopting normalized decay curves of G/G_0 and damping ratio from the torsional shear tests performed on the intact material PAN (Figure VII.2b) with unit weight γ=15 KN/m^3; instead, for the seashore sands (SS in Figure VII.2c) literature data (de Silva et al. 2015) were used and a unit weight γ=18 KN/m^3. The bedrock was assumed ad the depth of 38m.

In Figures VII.2b-c the decay of the shear modulus curves is plotted also in terms of analytical curves fitted by MKZ model; on the same chart, the damping- strain curves fitted by Masing rules and modified by Philiph & Hashash (2009) are plotted too.

Because of the lack of a cyclic resistance curve relevant to SS layer, the parameters of Park & Ahn pwp model were calibrated by adopting for the whole deposit the cyclic resistance curves of PAN (Figure VII.3a). The relationship between the pore pressure ratio and the damage parameter was defined as the best-fitting function of the R_u-N_{cyc} data points relevant to the laboratory tests performed on PAN (Δq=80kPa and Δq=100kPa) and shown in Figure VII.3b. All the above described parameters are listed in Table VII.2.

TABLE VII.2: PARAMETERS OF PWP MODEL.

CSR-N_{cyc} (Park & Ahn, 2013)				*Ru-N_{cyc}/N_L*		
a	CSR_t	N_r	CSR_r	a	b	c
1	0.3	11	0.4	1.049	0.33375	-0.1548

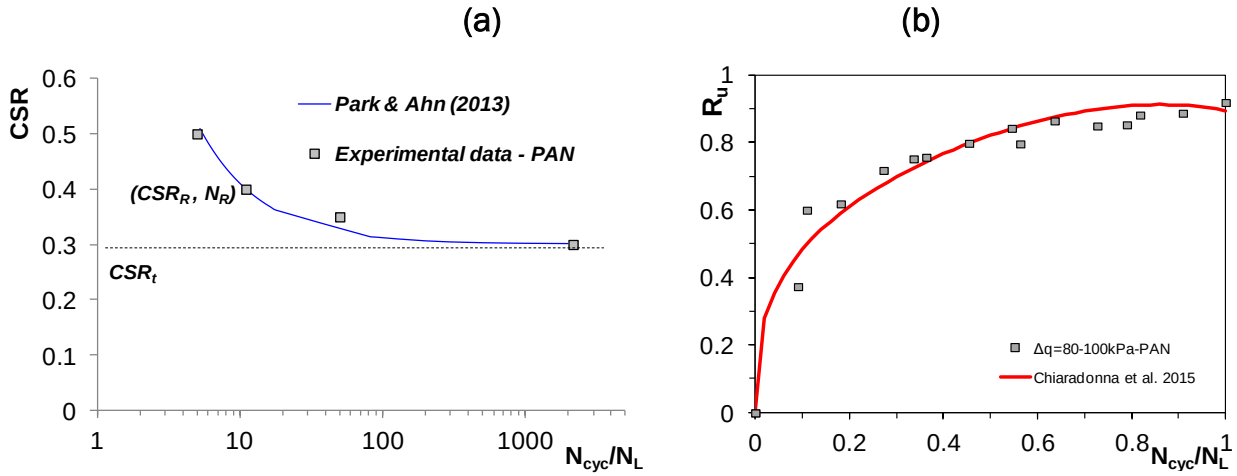

FIGURE VII.3: EXPERIMENTAL DATA VS ANALYTICAL CYCLIC RESISTANCE CURVE (A) AND MAXIMUM SHEAR STRESS PROFILE (B).

VII.1.2 Results of the dynamic analyses

The results of the decoupled and coupled analysis are plotted in terms of vertical profiles of maximum shear stress (Figure VII.4), acceleration (Figure VII.5), shear strain (Figure VII.6) and R_u only for coupled analyses (Figure VII.7). In all the charts of Figures 4-6, it is shown a good agreement between the responses of the dynamic analysis performed in total and effective stresses. The distributions of the maximum acceleration profiles, illustrated in Figure VII.5, show the highest value is reached in all the cases at the top of the deposit. On the contrary, in Figure VII.6, the peaks of maximum shear strain are evidenced at the depth of 16m where the V_s profile in Figure VII.2a highlights a decreasing stiffness.

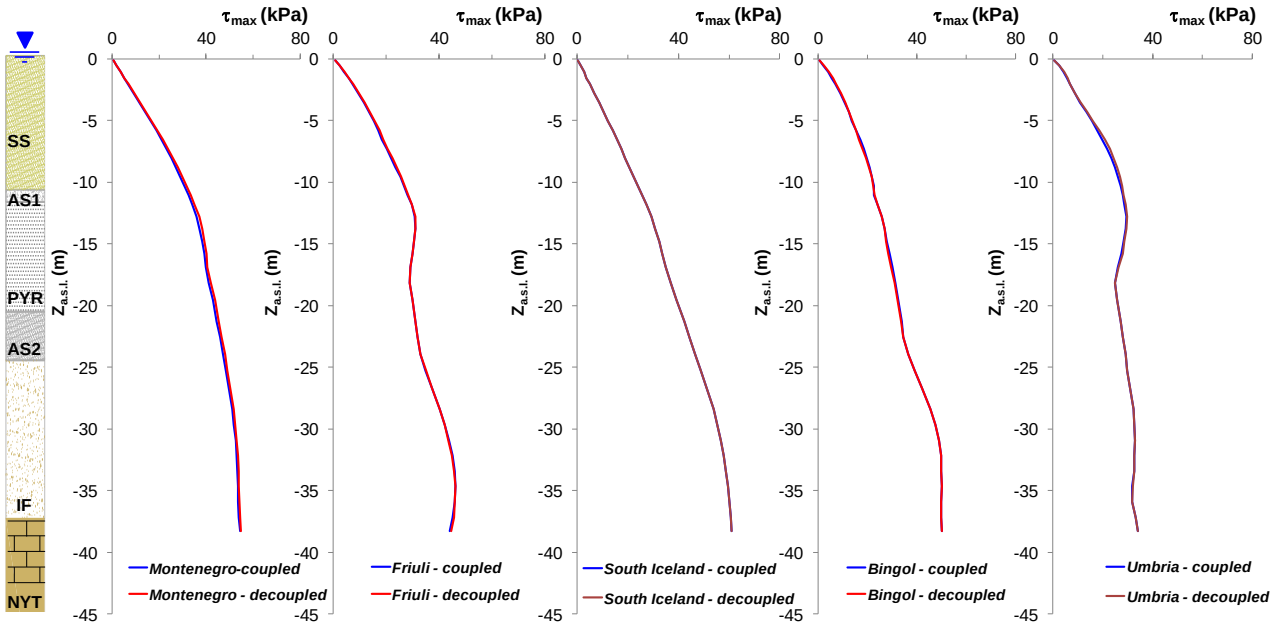

FIGURE VII.4: VERTICAL MAX SHEAR STRESS PROFILES RESULTING FROM COUPLED AND DECOUPLED DYNAMIC ANALYSES.

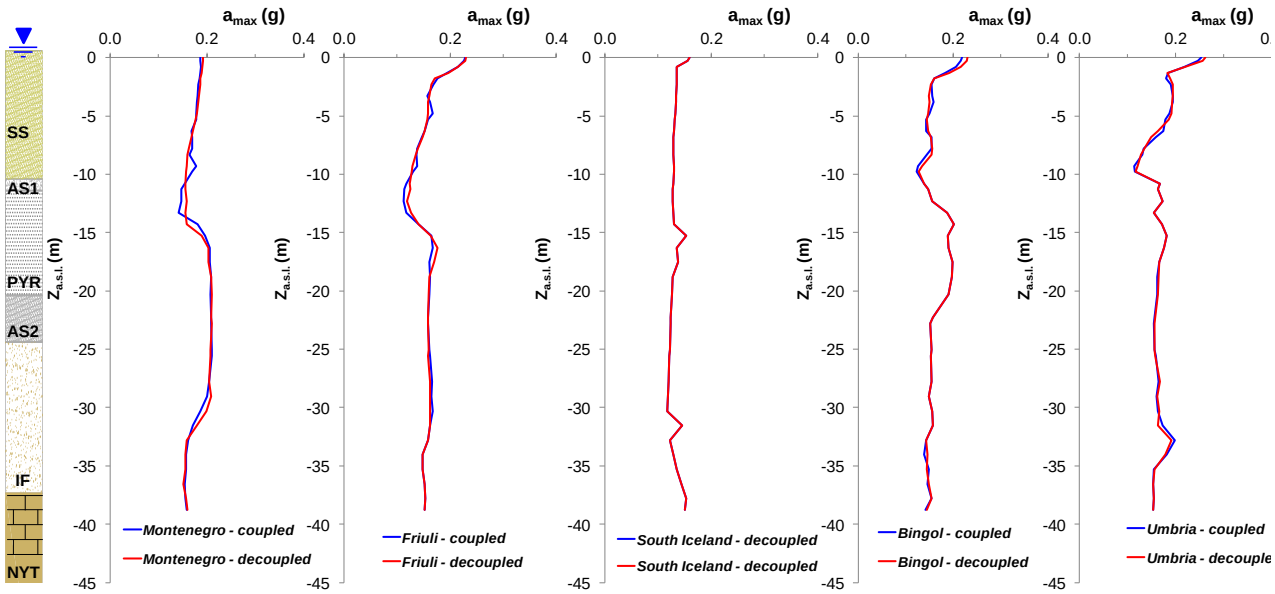

FIGURE VII.5: VERTICAL MAX ACCELERATION PROFILES RESULTING FROM COUPLED AND DECOUPLED DYNAMIC ANALYSES.

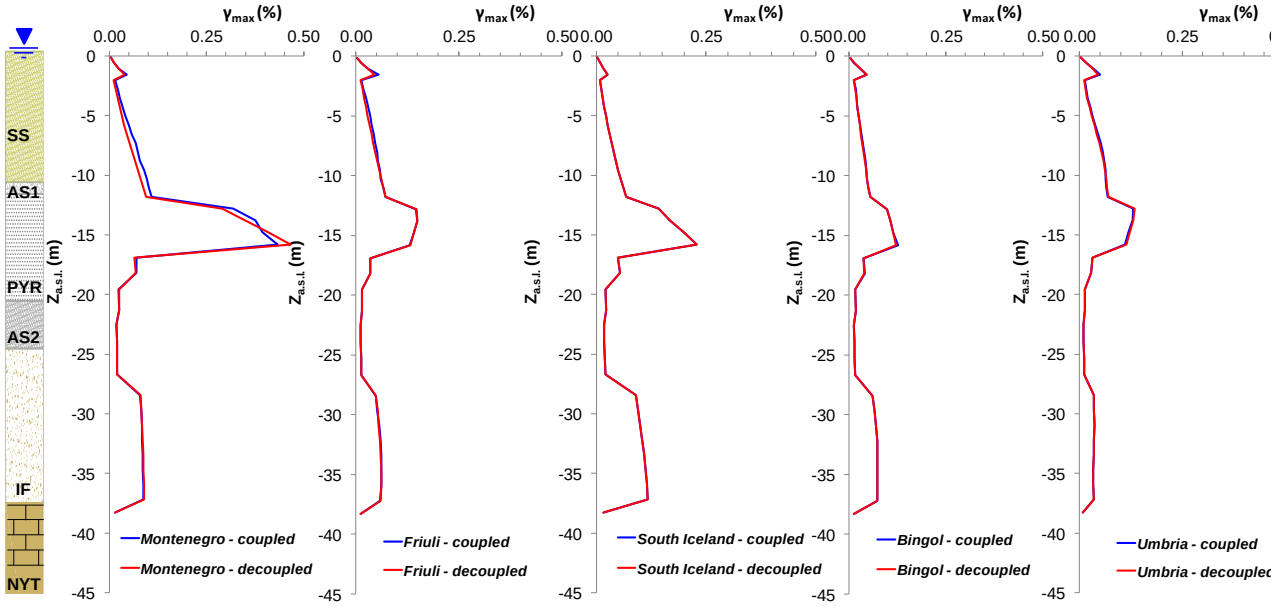

FIGURE VII.6: VERTICAL MAX STRAIN PROFILES RESULTING FROM COUPLED AND DECOUPLED DYNAMIC ANALYSES.

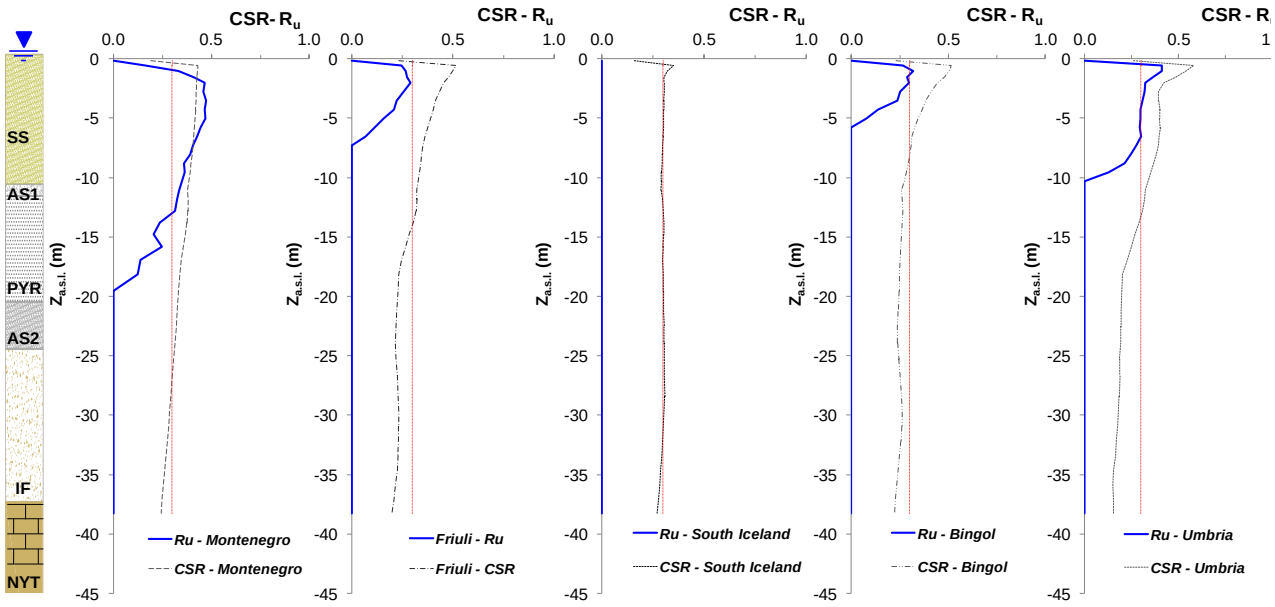

FIGURE VII.7: VERTICAL PORE PRESSURE RATIO, R_u, PROFILES RESULTING FROM COUPLED ANALYSYS.

Figure VII.7 illustrates the profiles of the peak value of R_u (blue lines), inferred from coupled analyses on the basis of the model proposed by Chiaradonna et al. (2015). According to the results shown, excess pore pressure accumulation is revealed only in the shallow layers of SS sandy deposit and, only for Montenegro earthquake, in the first four meters of volcanic layers (AS1 and PYR), while, South Iceland earthquake does not show any pore pressure accumulation. In no cases liquefaction occurred since R_u did not achieved the threshold value 0.9.

The results shown in Figure VII.7 are justified referring to the trend of the cyclic stress ratio, CSR, plotted against the depth, z, on the same charts. In fact, as said in §VII.1, the pwp model of Chiaradonna et al (2015) is stress-based model where the R_u value is computed every time that, at each depth, the normalized stress history of the earthquake achieves the CSR_t threshold. It can be seen that when CSR crosses the threshold above assumed, CSR_t=0.3 (reported by the red lines in Figure VII.7), approximately at the same depth the increment of R_u is detected. On the contrary, if R_u profiles are compared with the shear strain profiles in Figure VII.6, the results are not perfectly coherent since the stress levels result "de-coupled" from the volumetric-shear coupling strain (corresponding to a G/G_0=0.2). In other words, R_u

should start to accumulate when, in conjunction, the CSRt value is crossed and the volumetric threshold is reached.

The shear stress histories in Figure VII.4, computed by the response analysis, were considered in order to assess the liquefaction occurrence as explained in §VII.1. It can be noted that, in seismic response analyses with both ES and TS approaches, the highest CSR are associated to the propagation of Montenegro and South Iceland signals which, among all, show the highest values of PGV.

TABLE VII.2: PARAMETERS REPRESENTING THE SIGNALS PROPAGATED AT DEPTH 18M.

	CSR	PGA (g)	I_a (cm/s)	D_{5-95} (s)	ν_0	PGV (cm/s)	T_m
decoupled analisys							
Friuli	0.169722346	0.170137	28.37	10.33	6.292	11.920	0.390
Montenegro	0.247350918	0.20285	66.3	12.4	12.258	22.160	0.510
Bingol	0.181797125	0.198457	27.3	8.56	10.748	11.480	0.420
Umbria	0.146434656	0.166136	24.8	5.47	22.852	8.940	0.220
South Iceland	0.218078056	0.132109	11.6	3.66	14.754	18.560	0.820
coupled analisys							
Friuli	0.164	0.160	27.200	5.020	11.753	11.920	3.660
Montenegro	0.217	0.206	69.400	12.310	11.942	22.170	0.500
Bingol	0.165	0.198	27.200	8.350	10.419	11.480	0.420
Umbria	0.131	0.157	24.400	5.900	21.017	8.940	0.230
South Iceland	0.196	0.132	11.600	3.630	14.876	18.560	0.820

Table VII.2 lists the parameters of the accelerograms propagated at z=18m performing dynamic analyses in effective and total stresses.

VII.2 Assessment based on dynamic analyses and empirical charts

Figure VII.8a and Figure VII.8b report the results of the assessment based on empirical charts in terms of CRR as function of normalized parameters $(N_1)_{60}$, q_{c1} and V_{s1} (described in §VI.3), CSR was evaluated by means of equation VII.1 (considering the contribute of K_σ) respectively performing a total stress (TS) and an effective stress (ES) dynamic analyses.

It can be noted that liquefaction is not expected to occur in all cases, except for the data points relevant to the lowest $(N_1)_{60}$ and q_{c1}, if the subsoil is shaken with Montenegro earthquake.

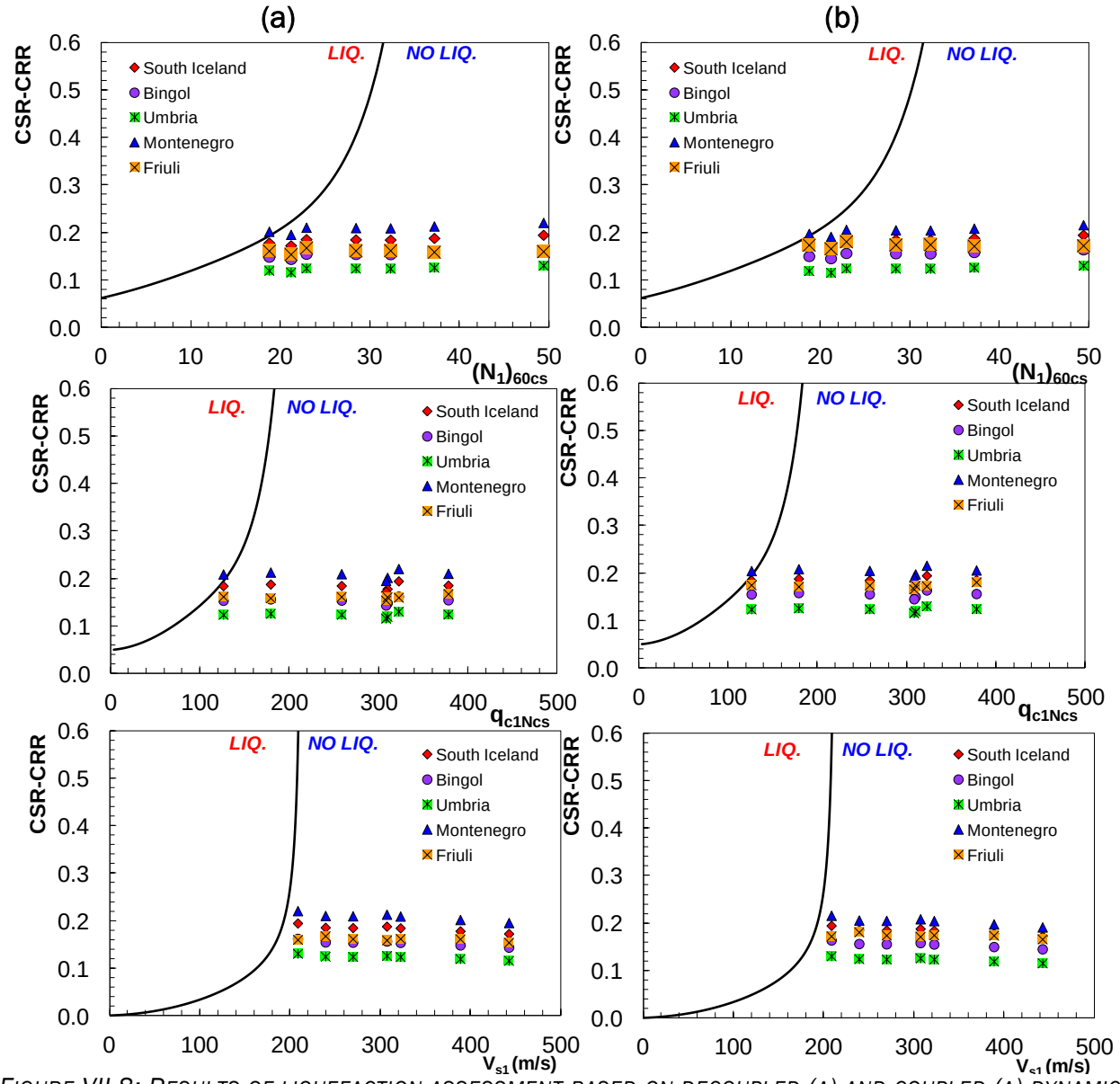

FIGURE VII.8: RESULTS OF LIQUEFACTION ASSESSMENT BASED ON DECOUPLED (A) AND COUPLED (A) DYNAMIC ANALYSES.

VII.3 Assessment based on dynamic analyses and cyclic resistance curve

The results of the dynamic analysis were also used to assess liquefaction potential by comparing CSR, obtained from the accelerogram propagated at the depth of interest (z=18.5m), with maximum resistance of soil, CRR_{lab}, inferred from the cyclic resistance curve of intact soil samples (PAN).

Since the maximum resistance of soil was experimentally obtained by applying regular stress histories, in order to compare CSR with CRR_{lab} it was necessary to convert the irregular earthquake load into an equivalent cyclic stress history with an amplitude $\tau_{eq}=0.65\tau_{max}$. Such a conversion was done by means of relationships provided by literature that correlate the number of equivalent cycles, N_{eq}, to synthetic parameters representing the earthquake records. The correlations used for the conversion are shown by the equations:

di Filippo et al., 2014

$$lnN_{eq} = \alpha + \beta \cdot lnPGA + \gamma \cdot lnI_a + \delta \cdot ln\,\nu_0 + \varepsilon \cdot lnPGV \quad \text{(VII.1)}$$

Biondi et al. ,2012

$$lnN_{eq} = \alpha + \beta \cdot lnPGA + \gamma \cdot lnI_a + \delta \cdot ln\,\nu_0 + \varepsilon \cdot lnD_{5-95} \quad \text{(VII.2)}$$

where:

- *PGA* and *PGV* are respectively the peak ground acceleration and velocity;
- I_a is Arias intensity;
- $D_{5\text{-}95}$ is the significant duration evaluated in the range $5\%<I_a<95\%$;
- ν_0 is the frequency of zero crossings.

All the above parameters must be meant as referred to the signals propagated at the depth of 18m (Table VII.2).

The authors proposed four different models (2V - $3V_1$ - $3V_2$ - 4V) according to the number of parameters considered in the correlations; the relevant coefficients are listed in Tables VII.3 and V.II.4.

The equivalent cyclic stress ratio, CSR, from decoupled and coupled analyses, are reported in Figure VII.9 against the equivalent number, N_{eq}, evaluated for each earthquake by means of the previous correlations. On the same charts, for comparison, the liquefaction curve interpolating the data points based on the strain criterion of cyclic triaxial tests performed on the intact soil samples (PAN) is shown.

TABLE VII.3: COEFFICIENTS FOR N_{EQ} CORRELATIONS

Biondi et al., 2012						
	Coefficients	α	β	γ	δ	ε
Model	parameters	B,C,D	B,C,D	B,C,D	B,C,D	B,C,D
2V	a_{max} - I_a	-0.095	-1.76	0.839	-	-
3V$_1$	a_{max} - I_a – D_{5-95}	0.44	-2.148	0.995	-	-0.393
3V$_2$	a_{max} -I_a - v_o	-2.255	-2.212	1.114	0.868	-
4V	a_{max} -I_a - v_o – D_{5-95}	-1.814	-2.426	1.194	0.829	-0.241
di Filippo et al., 2014						
	Coefficients	α	β	γ	δ	ε
Model	parameters	C,D,E	C,D,E	C,D,E	C,D,E	C,D,E
2V	a_{max} - I_a	-1.289	-1.102	0.547	-	-
3V$_1$	a_{max} - I_a – *PGV*	-5.704	-1.868	0.927		-0.723
3V$_2$	a_{max} -I_a - n_o	-1.168	-1.168	0.969	0.816	
4V	a_{max} -I_a - n_o – *PGV*	-4.529	-1.697	0.993	0.607	-0.279

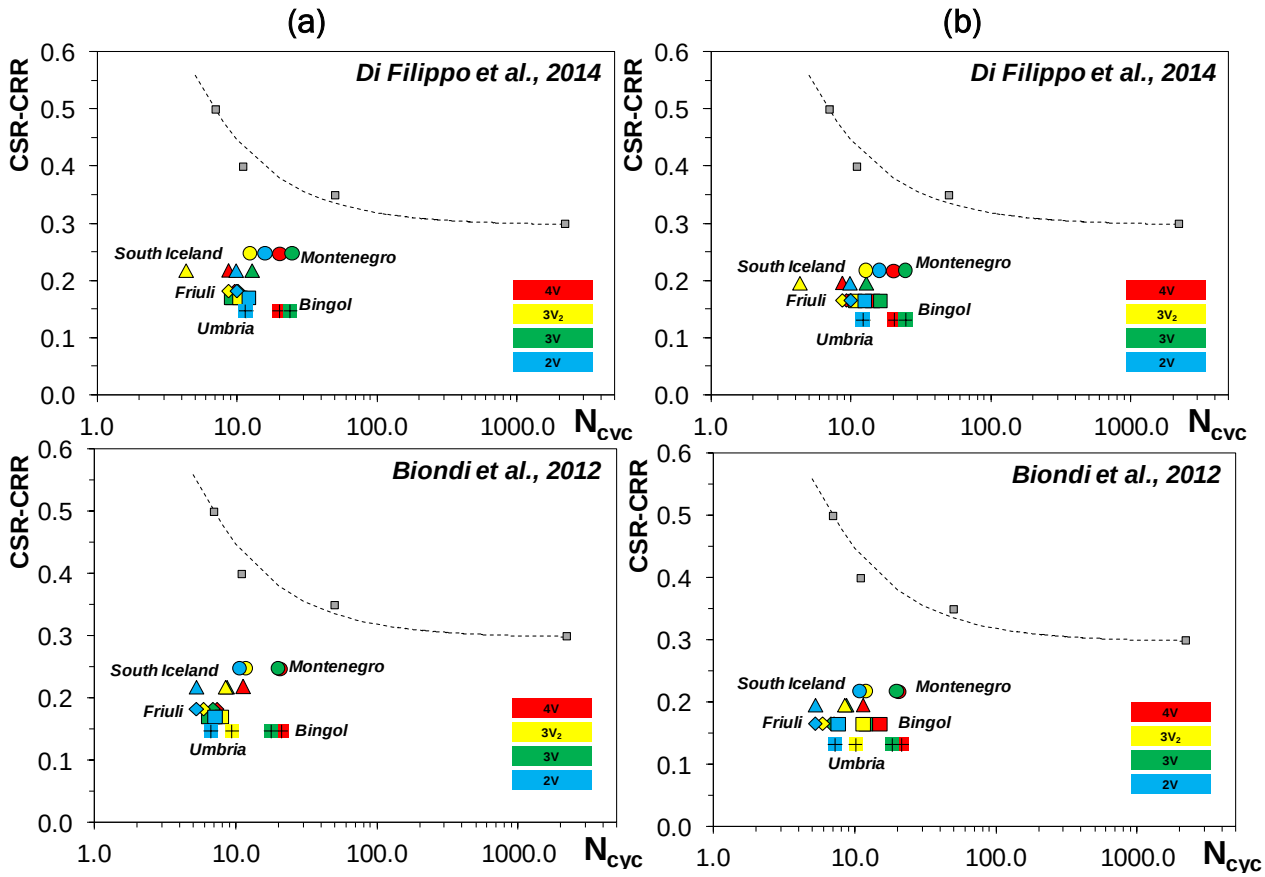

FIGURE VII.9: RESULTS OF LIQUEFACTION ASSESSMENT BASED ON THE COMPARISON WITH CYCLIC RESISTANCE CURVE.

Liquefaction conditions should correspond to the data points lying above the cyclic resistance curve; as shown in Figures VII.9a-b, no one of the CSR-N_{eq} combination computed for each earthquake provides values above the maximum resistance expressed by the cyclic curve. In addition, in accordance with the lack of R_u accumulation in Figure VII.7 at 18m depth, it can be noted that all the CSR values are well below the asymptotic value of the curve. Moreover, N_{eq} resulting from the application of Di Filippo et al (2014) and Biondi et al (2012) is strongly dependant on the models (2V - $3V_1$ - $3V_2$ - 4V in Figures VII.9) adopted; the most precautionary ones seems to be the models calibrated on the I_a, *PGV* and a_{max} parameters (4V and $3V_1$). Again, Montenegro earthquake appears as the most hazardous motion.

Conclusions and future developments

The objective of this thesis was the study of the cyclic liquefaction behavior of a typical pyroclastic silty sand, with a specific attention to geotechnical earthquake engineering applications. It was pursued by experimental investigations both in the laboratory and in the field on a representative case study; the experimental results were used for a critical assessment of chart-based empirical methods and coupled and de-coupled dynamic analyses.

The extensive laboratory testing programme included the execution of different series of cyclic triaxial tests in undrained conditions, through which the cyclic resistance curves of the natural soil as well as those of different reconstituted materials were defined.

The cyclic resistance curve of intact soil samples (PAN) was compared with that of the reconstituted pumice+ash mixture (PARa), prepared with the same grain size and relative density at the end of consolidation (D_R=40%), tested at the same effective confining stress (p'=100kPa). The higher cyclic strength of PAN with respect to that of PARa at the same state revealed a significant effect of the soil fabric on the liquefaction behavior. Similar results had been also achieved by Suzuki & Yamamoto (2004) and Orense & Pender (2013), who found that the liquefaction strength of undisturbed samples of pyroclastic pumiceous sands was higher than that of the reconstituted samples at the same state conditions.

The cyclic resistance of PARa was then compared with that of the same reconstituted pumice+ash mixture (PARb), but in this case prepared with a lower initial void ratio,

in order to obtain a higher relative density (D_R=60%) at the end of consolidation paths driven to higher effective confining stress (p'=400kPa). The comparison of PARa and PARb cyclic resistance curves confirmed that the liquefaction strength of this pyroclastic soil seems poorly affected by the state, in contrast with what usually shown in literature on hard-grained sands (e.g. Yamamoto et al., 2009). On the other hand, the results appear in a substantial qualitative agreement with those obtained by Orense & Pender (2013) on pumice sands. These latter Authors showed that the cyclic resistance slightly increases with density, but tends to decrease with the confining stress. For the specific pumice + ash mixture tested in this study, the results showed an overall slight decrease of cyclic resistance with a simultaneous increase of both relative density and effective stress. Summarizing, it appears that, while an increase of density can result into a less liquefiable soil fabric, the effective confining pressure may likely induce the occurrence of crushing of volcanic sand particles, which, in turn, may inhibit the contrasting beneficial effect of relative density on liquefaction resistance.

Thus, in order to evaluate the effect of a possible occurrence of grain crushing, the cyclic resistance curve of PARa was compared with that of a mixture of silica sand + ashy fine content (SAR), prepared with the same grain size distribution, and consolidated to the same relative density and effective confining pressure. It was verified that SAR cyclic resistance curve was slightly lower than that of PARa; being the grain size distributions of PARa, PARb and SAR measured before and after the tests practically unchanged, no appreciable evidence of particle breakage was found in any case. No crushing occurrence in such pumice+ash mixtures may be justified by the presence of a high fine content (FC=30%) which, surrounding the greater particles, make them more resistant against breakage (Casini & Viggiani, 2011); on the other hand, the conclusions on the effects of relative density and the effective confining pressure before mentioned seem still questionable.

The effect of non-plastic fine on liquefaction strength was also investigated by comparing, once again, the cyclic resistance curve of material PARa with that of a reconstituted mixture of pumice + low-plasticity clay (PCR), again prepared at the same grain size distribution and consolidated at p'=100kPa to obtain D_R=40%. The

comparison showed that, in discordance with many studies reporting the beneficial influence of increasing plasticity on liquefaction resistance (e.g. Ishihara & Koseki, 1989), the non-plastic fine fraction in this case conveys a greater liquefaction resistance to PARa with respect to PCR mixture. This result confirms the overall uncertainties still existing on the effective role of non-plastic fine on undrained behavior, widely discussed in literature (Fei, 1991; Okashi, 1970; Verdugo, 1985; Kaufman, 1982; Chang et al., 1982; Dezfulian, 1982; Troncoso & Verdugo, 1985), and might be justified by the reduction of the friction angle, φ', with plasticity (Law & Ling, 1992).

Summarizing, it can be inferred that, at the site conditions (D_R=40% and p'=100kPa) in a range of cyclic deviator stress of 60-100kPa, no significant particle crushing occurred and the non-plastic fine ash improved the undrained resistance under cyclic loads.

It was then examined if the tools commonly used in practice to assess the field liquefaction potential would somehow reflect the above peculiar results of the laboratory tests.

Liquefaction at Riviera di Chiaia site was first assessed by means of simplified procedures, based on semi-empirical charts (e. g. Seed & Idriss, 1982; Idriss & Boulanger, 2004; Andrus & Stokoe, 2000) where the seismic action was defined on the basis of both pseudo-static approaches and by dynamic analyses; in this latter case, soil resistance was defined through the results of both in situ tests (SPT, CPT and V_s measurements) and the cyclic resistance curve of the natural soil (PAN).

The assessment based on simplified procedures by the pseudo-static approach was affected by the correct choice of the parameters defining both seismic demand, expressed by the cyclic stress ratio (CSR), and soil capacity, expressed by the cyclic resistance ratio (CRR).

Sensitivity analyses of the influence on CSR of the magnitude scaling factor (MSF) and the peak ground acceleration, a_g, led to the proposal of a site-specific 'liquefaction hazard curve', which allowed for including in the formulation of CSR both MSF and a_g, since they are both dependent on the same seismic hazard.

It was shown that CSR, if evaluated by means of literature expressions of MSF (Cetin et al., 2004; Andrus & Stokoe, 2000; Idriss, 1999), underestimates the seismic demand, even if MSF was specifically determined by the procedure based on the cyclic resistance curve of PAN. In particular, it was verified how the slope of the curve and the function interpolating the experimental data points affect the final definition of MSF.

The results of assessment by means of literature charts highlighted that, estimating the seismic action by a pseudo-static approach, liquefaction is predicted for the lowest values of the resistance provided by the results of SPT and CPT; on the contrary, the assessment based on V_s measurements never showed liquefaction. The above results are in agreement with the findings of Orense & Pender (2013).

To further assess the reliability of semi-empirical procedures based on the charts, 1D dynamic analyses were performed with five spectrum-compatible seismic records. The numerical predictions were carried out by the SCOSSA code (Tropeano et al., 2015) by means of a decoupled and a coupled approach, this latter based on a simplified model of pore pressure build-up (Chiaradonna et al., 2015). Both approaches led to define the profile of maximum shear stress, while the latter also simulated the time histories of pore pressure ratio, R_u, at the depth of interest.

The peak shear stress value were used to define CSR, that was then compared with the resistance measured by in-situ tests (SPT, CPT and V_S measurements) and with the cyclic resistance curve of the natural soil samples. The pyroclastic soil layer was verified in both cases safe against liquefaction; moreover, the results of the coupled dynamic analyses showed that the development of R_u was negligible for four out of the five earthquake records selected.

It can be generally concluded that the pseudo-static approach to evaluate the seismic demand may be more or less conservative than the dynamic analyses, depending on the correct choice of the factors to determine it.

Also, when the soil resistance (CRR) is based on in-situ tests by means of literature correlations (e.g. Idriss & Boulanger, 2004), the presence of non-plastic fine is not taken into account as a beneficial effect for liquefaction, as shown by laboratory

results. In addition, it was confirmed that the adoption of CPT and SPT provides an underestimation of soil resistance, maybe due to the breakage of pumice particles under compressive stresses due to penetration (Rippa & Vinale, 1983; Orense & Pender, 2013), even though grain crushing was not apparent from the laboratory experimental evidences. The above observations let further uncertainties arise about the reliability of penetration-based charts to assess liquefaction for pyroclastic deposits.

In the light of the previous findings, future research developments may regard both the laboratory activity and semi-empirical as well as dynamic analyses.

In the laboratory, it should be deepened with more sophisticated experimental tools if and how the fine ash content may affect crushing of pumice particles and, thus, the cyclic resistance curves. Further tests may be also performed to clarify the role of the relative density and effective confining pressure on liquefaction resistance of pyroclastic soils.

In the case of the field scale approaches, literature empirical charts may be ideally adapted to take into account the presence of non-plastic fines and particle breakage. In addition, for the definition of seismic action by the pseudo-static approach, different MSF relationships may be proposed as a function of the relative density, since this latter affects the slope of the cyclic resistance curve.

Finally, the reliability of dynamic analyses obtained by the coupled approach may be further improved trying to link the R_u accumulation based on the trespassing of the stress ratio threshold with the attainment of volumetric-distorsional coupling threshold strain.

Appendix 1

PHYSICAL AND STATE PROPERTIES OF PAN, PARA AND PARB.

		σ_a (kPa)	Δq_{cyc} (kPa)		n	e	w	S_R	γ (kN/m^3)	γ_d (kN/m^3)
PAN	IC	60-600	-	start	0.615	1.596	0.599	0.942	15.169	9.487
				saturation	0.602	1.514	0.604	1.002	15.712	9.795
				end	0.573	1.373	0.536	0.980	16.143	10.510
	TX-CID	100	-	start	0.567	1.309	0.349	0.669	14.383	10.664
				saturation	0.551	1.228	0.487	0.996	16.438	11.053
				consolidation	0.550	1.224	0.486	0.996	16.448	11.069
				end	0.542	1.184	0.470	0.996	16.571	11.275
	TX-CID	150	-	start	0.597	1.483	0.437	0.739	14.249	9.918
				saturation	0.554	1.243	0.496	1.001	16.420	10.978
				consolidation	0.552	1.232	0.491	1.000	16.448	11.033
				end	0.540	1.172	0.467	1.000	16.629	11.335
	TX-CID	200	-	start	0.577	1.365	0.420	0.773	14.791	10.413
				saturation	0.563	1.287	0.510	0.994	16.257	10.768
				consolidation	0.561	1.280	0.507	0.994	16.275	10.799
				end	0.545	1.199	0.475	0.994	16.513	11.197
	TX-CIU	200	-	start	0.548	1.210	0.198	0.410	14.791	11.140
				saturation	0.546	1.202	0.477	0.995	16.257	11.181
				consolidation	0.527	1.116	0.442	0.994	16.275	11.639
				end	0.527	1.115	0.442	0.994	16.513	11.640
	TX-CIU	250	-	start	0.536	1.153	0.204	0.444	13.342	11.435
				saturation	0.537	1.161	0.463	1.000	16.512	11.394
				consolidation	0.522	1.091	0.434	0.999	16.780	11.775
				end	0.518	1.075	0.428	0.999	16.781	11.865
	TX-CIU	350	-	start	0.555	1.247	0.191	0.384	13.053	10.961
				saturation	0.540	1.174	0.467	0.999	16.617	11.326
				consolidation	0.518	1.076	0.428	0.997	16.931	11.860
				end	0.518	1.073	0.426	0.997	16.942	11.879
	TX-CYC	100	60	start	0.603	1.517	0.476	0.787	14.437	9.784
				saturation	0.580	1.380	0.520	0.947	15.731	10.346
				consolidation	0.583	1.398	0.528	0.947	15.687	10.269
				end	0.583	1.398	0.528	0.947	15.687	10.269
	TX-CYC	100	70a	start	0.605	1.534	0.401	0.656	13.609	9.716
				saturation	0.583	1.401	0.551	0.987	15.908	10.256
				consolidation	0.590	1.438	0.566	0.988	15.815	10.099
				end	0.590	1.438	0.566	0.988	15.815	10.099

	TX-CYC	100	70b	start	0.610	1.562	0.445	0.715	13.887	9.610
				saturation	0.606	1.536	0.608	0.993	15.608	9.708
				consolidation	0.605	1.529	0.605	0.993	15.624	9.736
				end	0.605	1.529	0.605	0.993	15.624	9.736
	TX-CYC	100	80	start	0.585	1.411	0.450	0.800	14.805	10.214
				saturation	0.567	1.311	0.501	0.960	15.999	10.656
				consolidation	0.571	1.329	0.509	0.961	15.950	10.571
				end	0.571	1.329	0.509	0.961	15.950	10.571
	TX-CYC	100	100	start	0.625	1.666	0.483	0.727	13.694	9.237
				saturation	0.599	1.493	0.576	0.968	15.565	9.876
				consolidation	0.589	1.434	0.553	0.967	15.705	10.114
				end	0.589	1.434	0.553	0.967	15.705	10.114

		σ_a (kPa)	Δq_{cyc} (kPa)		n	e	w	S_R	γ (kN/m^3)	γ_d (kN/m^3)
PARa	IC	100-300	-	start	0.623	1.651	0.658	1.000	15.398	9.289
				consolidation	0.542	1.328	0.529	1.000	17.254	11.283
				end	0.530	1.271	0.507	1.000	17.424	11.566
	TX-CIU	30	-	start	0.598	1.485	0.592	1.000	15.770	9.908
				consolidation	0.570	1.327	0.529	1.000	16.176	10.582
				end	0.570	1.327	0.529	1.000	16.176	10.582
	TX-CYC	100	80	start	0.602	1.509	0.601	1.000	15.713	9.812
				consolidation	0.570	1.325	0.528	1.000	16.169	10.583
				end	0.570	1.325	0.528	1.000	16.169	10.583
	TX-CYC	100	60	start	0.612	1.576	0.628	1.000	15.560	9.557
				consolidation	0.571	1.331	0.530	1.000	16.170	10.567
				end	0.571	1.331	0.530	1.000	16.170	10.567
	TX-CYC	100	50	start	0.594	1.464	0.583	1.000	15.822	9.994
				consolidation	0.568	1.315	0.524	1.000	16.190	10.625
				end	0.568	1.315	0.524	1.000	16.190	10.625
	TX-CYC	100	40	start	0.590	1.440	0.574	1.000	15.882	10.092
				consolidation	0.590	1.319	0.525	1.000	15.394	10.092
				end	0.590	1.319	0.525	1.000	15.394	10.092

		σ_a (kPa)	Δq_{cyc} (kPa)		n	e	w	S_R	γ (kPa/m^3)	γ_d (kPa/m^3)
PARb	IC	60-400	-	start	0.587	1.423	0.297	0.525	13.183	10.161
				saturation	0.576	1.359	0.533	0.985	16.006	10.439
				consolidation	0.559	1.265	0.496	0.984	16.262	10.869
				end	0.533	1.141	0.447	0.982	16.635	11.498
	IC	60-340	-	start	0.632	1.715	0.391	0.573	12.620	10.161
				saturation	0.567	1.307	0.507	0.974	16.089	10.439

				consolidation	0.564	1.295	0.503	0.974	16.123	10.869
				end	0.536	1.154	0.447	0.971	16.534	11.498
	TX-CYC	100	160	start	0.587	1.423	0.297	0.525	13.183	10.161
				saturation	0.576	1.359	0.533	0.985	16.006	10.439
				approaching	0.559	1.265	0.496	0.984	16.262	10.869
				consolidation	0.533	1.141	0.447	0.982	16.635	11.498
				end	0.533	1.141	0.447	0.982	16.635	11.498
	TX-CYC	100	120	start	0.632	1.715	0.391	0.573	12.620	9.070
				saturation	0.567	1.307	0.507	0.975	16.091	10.674
				approaching	0.564	1.294	0.502	0.974	16.125	10.732
				consolidation	0.536	1.154	0.447	0.971	16.536	11.431
				end	0.536	1.154	0.447	0.971	16.536	11.431
	TX-CYC	100	80	start	0.622	1.644	0.354	0.541	12.612	9.313
				saturation	0.604	1.523	0.598	0.986	15.595	9.758
				approaching	0.575	1.352	0.530	0.984	16.015	10.468
				consolidation	0.543	1.189	0.465	0.981	16.479	11.250
				end	0.543	1.189	0.465	0.981	16.479	11.250

PHYSICAL AND STATE PROPERTIES OF PCR.

		σ_a (kPa)	Δq_{cyc} (kPa)		n	e	w	S_R	γ (kN/m^3)	γ_d (kN/m^3)
PCR	IC	100-280	-	start	0.630	1.703	0.668	1.000	15.436	9.255
				consolidation	0.567	1.312	0.515	1.000	16.386	10.819
				end	0.556	1.254	0.492	1.000	16.557	11.100
	CIU	20	-	start	1.623	0.636	1.000	1.591	15.607	9.538
				consolidation	1.432	0.562	1.000	1.637	16.061	10.284
				end	1.432	0.562	1.000	1.637	16.062	10.285
	CIU	200	-	start	0.645	1.816	0.712	1.000	15.436	8.884
				consolidation	0.561	1.277	0.501	1.000	16.386	10.985
				end	0.561	1.277	0.501	1.000	16.557	10.985
	CIU	400	-	start	0.625	1.667	0.654	1.000	15.838	9.379
				consolidation	0.551	1.227	0.481	1.000	16.403	11.232
				end	0.551	1.227	0.481	1.000	16.403	11.232
	CIU	600	-	start	0.628	1.685	0.661	1.000	15.474	9.318
				consolidation	0.541	1.181	0.463	1.000	16.782	11.470
				end	0.541	1.181	0.463	1.000	16.782	11.470
	TC-CYC	100	50	start	0.619	1.623	0.634	1.000	15.644	9.573
				consolidation	0.565	1.297	0.507	1.000	16.473	10.934
				end	0.565	1.297	0.507	1.000	16.473	10.934
	TC-CYC	100	40	start	0.596	1.474	0.578	1.000	15.956	10.111
				consolidation	0.566	1.305	0.512	1.000	16.406	10.852

			end	0.566	1.305	0.512	1.000	16.406	10.852
TC-CYC	100	30	start	0.614	1.591	0.624	1.000	15.678	9.653
			consolidation	0.568	1.317	0.516	1.000	16.372	10.796
			end	0.568	1.317	0.516	1.000	16.372	10.796
TC-CYC	100	25	start	0.604	1.523	0.597	1.000	15.838	9.916
			consolidation	0.566	1.306	0.512	1.000	16.403	10.846
			end	0.566	1.306	0.512	1.000	16.403	10.846

PHYSICAL AND STATE PROPERTIES OF SAR.

		σ_a (kPa)	Δq_{cyc} (kPa)		n	e	w	S_R	γ (kN/m^3)	γ_d (kN/m^3)
	IC	100-600	-	start	0.529	1.124	0.424	1.000	17.431	12.240
				consolidation	0.465	0.870	0.328	1.000	18.465	13.900
				end	0.430	0.753	0.284	1.000	19.044	14.830
	CIU	30	-	start	0.480	0.923	0.348	1.000	18.228	13.520
				consolidation	0.466	0.874	0.330	1.000	18.447	13.871
				end	0.466	0.874	0.330	1.000	18.447	13.871
	CIU	200	-	start	0.485	0.941	0.355	1.000	18.150	13.395
				consolidation	0.449	0.814	0.307	1.000	18.732	14.330
				end	0.449	0.814	0.307	1.000	18.732	14.330
	CIU	400	-	start	0.488	0.951	0.359	1.000	18.105	13.322
				consolidation	0.423	0.732	0.276	1.000	19.155	15.008
				end	0.423	0.732	0.276	1.000	19.155	15.008
	CIU	600	-	start	0.500	1.002	0.378	1.000	17.896	12.987
SAR				consolidation	0.410	0.696	0.263	1.000	19.355	15.329
				end	0.411	0.697	0.263	1.000	19.350	15.322
	TC-CYC	100	50	start	0.549	1.218	0.460	1.000	17.109	11.722
				consolidation	0.481	0.928	0.350	1.000	18.205	13.483
				end	0.481	0.928	0.350	1.000	18.205	13.483
	TC-CYC	100	40	start	0.529	1.125	0.425	1.000	17.426	12.232
				consolidation	0.486	0.945	0.356	1.000	18.134	13.368
				end	0.486	0.945	0.356	1.000	18.134	13.368
	TC-CYC	100	30	start	0.527	1.113	0.420	1.000	17.469	12.300
				consolidation	0.483	0.935	0.353	1.000	18.174	13.434
				end	0.483	0.935	0.353	1.000	18.174	13.434
	TC-CYC	100	25	start	0.543	1.190	0.449	1.000	17.201	11.871
				consolidation	0.485	0.941	0.355	1.000	18.150	13.395
				end	0.485	0.941	0.355	1.000	18.150	13.395

Appendix 2

TABLE VI.3: PARAMETERS OF VERIFICATION WITH LITERATURE MSF

MSF - Idriss (1999)								
Modal	***Average***	***Fs-weighted***	***Max***	***PSHA-liq***	N_{SPT}	C_N	k_σ	$(N_1)_{60}$
0.133	0.139	0.142	0.330	0.060	52	0.951	0.839	49.432
0.115	0.120	0.123	0.286	0.051	25	0.917	0.971	22.932
0.114	0.119	0.122	0.287	0.051	31	0.918	0.961	28.464
0.117	0.122	0.125	0.294	0.052	40	0.931	0.938	37.224
0.116	0.121	0.123	0.291	0.052	35	0.924	0.948	32.335
0.111	0.116	0.118	0.282	0.050	21	0.894	0.971	18.776
0.108	0.113	0.115	0.279	0.048	24	0.884	0.968	21.210
Modal	***Average***	***Fs-weighted***	***Max***	***PSHA-liq***	q_c (Mpa)	C_q	k_σ	q_{c1N}
0.117	0.122	0.125	0.290	0.052	29	0.996	0.955	322.01
0.112	0.116	0.119	0.277	0.050	35	1.010	1.000	377.60
0.117	0.122	0.124	0.293	0.052	22	0.976	0.940	258.04
0.118	0.124	0.126	0.297	0.053	13	0.943	0.926	178.67
0.117	0.122	0.125	0.293	0.052	10	0.914	0.939	125.74
0.122	0.128	0.130	0.310	0.055	28	0.991	0.882	309.41
0.109	0.114	0.116	0.283	0.049	28	0.990	0.957	307.81
Modal	***Average***	***Fs-weighted***	***Max***	***PSHA-liq***	V_s (m/s)	C_v	k_σ	V_{S1} (m/s)
0.112	0.116	0.119	0.277	0.050	210	0.945	-	206.91
0.112	0.116	0.119	0.277	0.050	236	0.937	-	208.07
0.110	0.115	0.117	0.276	0.049	267	0.933	-	238.77
0.110	0.115	0.117	0.276	0.049	410	0.928	-	269.19
0.110	0.115	0.117	0.276	0.049	372	0.924	-	306.74
0.108	0.113	0.115	0.274	0.048	512	0.920	-	321.88
0.104	0.109	0.111	0.270	0.047	388	0.916	-	388.18
MSF - Andrus & Stokoe (1997)								
Modal	***Average***	***Fs-weighted***	***Max***	***PSHA-liq***	N_{SPT}	C_N	k_σ	$(N_1)_{60}$
0.074	0.089	0.081	0.324	0.060	52.000	0.951	0.839	49.432
0.064	0.077	0.070	0.280	0.051	25.000	0.917	0.971	22.932
0.064	0.077	0.070	0.281	0.051	31.000	0.918	0.961	28.464
0.065	0.079	0.071	0.288	0.052	40.000	0.931	0.938	37.224
0.065	0.078	0.071	0.285	0.052	35.000	0.924	0.948	32.335
0.062	0.075	0.068	0.276	0.050	21.000	0.894	0.971	18.776
0.060	0.073	0.066	0.274	0.048	24.000	0.884	0.968	21.210
Modal	***Average***	***Fs-weighted***	***Max***	***PSHA-liq***	q_c (Mpa)	C_q	k_σ	q_{c1N}
0.074	0.089	0.081	0.324	0.060	28.800	0.996	0.955	322.010
0.064	0.077	0.070	0.280	0.051	34.800	1.010	1.000	377.604
0.064	0.077	0.070	0.281	0.051	21.900	0.976	0.940	258.041
0.065	0.079	0.071	0.288	0.052	13.300	0.943	0.926	178.666

0.065	0.078	0.071	0.285	0.052	9.600	0.914	0.939	125.744
0.062	0.075	0.068	0.276	0.050	28.000	0.991	0.882	309.414
0.060	0.073	0.066	0.274	0.048	27.800	0.990	0.957	307.812
Modal	***Average***	***Fs-weighted***	***Max***	***PSHA-liq***	***V_s (m/s)***	***C_v***	***k_σ***	***V_{S1} (m/s)***
0.062	0.075	0.068	0.272	0.050	210.000	0.945	-	206.907
0.062	0.075	0.068	0.272	0.050	236.000	0.937	-	208.070
0.061	0.074	0.067	0.270	0.049	267.000	0.933	-	238.770
0.061	0.074	0.067	0.270	0.049	410.000	0.928	-	269.191
0.061	0.074	0.067	0.270	0.049	372.000	0.924	-	306.735
0.060	0.073	0.066	0.268	0.048	512.000	0.920	-	321.880
0.058	0.070	0.064	0.265	0.047	388.000	0.916	-	388.176
MSF - Cetin et al. (2004)								
Modal	***Average***	***Fs-weighted***	***Max***	***PSHA-liq***	***N_{SPT}***	***C_N***	***k_σ***	***$(N_1)_{60}$***
0.087	0.103	0.095	0.328	0.060	52	0.951	0.839	49.432
0.075	0.089	0.082	0.283	0.051	25	0.917	0.971	22.932
0.075	0.088	0.081	0.284	0.051	31	0.918	0.961	28.464
0.076	0.090	0.083	0.291	0.052	40	0.931	0.938	37.224
0.076	0.089	0.082	0.288	0.052	35	0.924	0.948	32.335
0.073	0.086	0.079	0.280	0.050	21	0.894	0.971	18.776
0.070	0.083	0.077	0.277	0.048	24	0.884	0.968	21.210
Modal	***Average***	***Fs-weighted***	***Max***	***PSHA-liq***	***q_c (Mpa)***	***C_q***	***k_σ***	***q_{c1N}***
0.076	0.090	0.083	0.288	0.052	29	0.996	0.955	322.010
0.073	0.086	0.080	0.275	0.050	35	1.010	1.000	377.604
0.076	0.090	0.083	0.290	0.052	22	0.976	0.940	258.041
0.077	0.091	0.084	0.295	0.053	13	0.943	0.926	178.666
0.076	0.090	0.083	0.291	0.052	10	0.914	0.939	125.744
0.080	0.094	0.087	0.308	0.055	28	0.991	0.882	309.414
0.071	0.084	0.078	0.280	0.049	28	0.990	0.957	307.812
Modal	***Average***	***Fs-weighted***	***Max***	***PSHA-liq***	***V_s (m/s)***	***C_v***	***k_σ***	***V_{S1} (m/s)***
0.073	0.086	0.080	0.275	0.050	210	0.945	-	206.907
0.073	0.086	0.080	0.275	0.050	236	0.937	-	208.070
0.072	0.085	0.078	0.273	0.049	267	0.933	-	238.770
0.072	0.085	0.078	0.273	0.049	410	0.928	-	269.191
0.072	0.085	0.078	0.273	0.049	372	0.924	-	306.735
0.070	0.083	0.077	0.271	0.048	512	0.920	-	321.880
0.068	0.081	0.074	0.268	0.047	388	0.916	-	388.176

TABLE VI.4: PARAMETERS OF VERIFICATION WITH POWER FUNCTION MSF

MSF - PW/ Seed et al. (1975)								
Modal	***Average***	***Fs-weighted***	***Max***	***PSHA-liq***	***N_{SPT}***	***C_N***	***k_σ***	***$(N_1)_{60}$***
0.209	0.219	0.219	0.347	0.060	52	0.951	0.839	49.432
0.181	0.189	0.189	0.300	0.051	25	0.917	0.971	22.932
0.180	0.188	0.188	0.301	0.051	31	0.918	0.961	28.464
0.184	0.193	0.192	0.308	0.052	40	0.931	0.938	37.224
0.182	0.191	0.190	0.305	0.052	35	0.924	0.948	32.335

0.175	0.183	0.183	0.296	0.050	21	0.894	0.971	18.776
0.169	0.178	0.177	0.293	0.048	24	0.884	0.968	21.210
Modal	***Average***	***Fs-weighted***	***Max***	***PSHA-liq***	***q_c (Mpa)***	***C_q***	***k_σ***	***q_{c1N}***
0.184	0.193	0.192	0.305	0.052	29	0.996	0.955	322.01
0.176	0.184	0.184	0.291	0.050	35	1.010	1.000	377.60
0.184	0.192	0.192	0.308	0.052	22	0.976	0.940	258.04
0.186	0.195	0.195	0.312	0.053	13	0.943	0.926	178.67
0.184	0.193	0.192	0.308	0.052	10	0.914	0.939	125.74
0.192	0.202	0.201	0.326	0.055	28	0.991	0.882	309.41
0.171	0.180	0.179	0.297	0.049	28	0.990	0.957	307.81
Modal	***Average***	***Fs-weighted***	***Max***	***PSHA-liq***	***V_s (m/s)***	***C_v***	***k_σ***	***V_{S1} (m/s)***
0.176	0.184	0.184	0.291	0.050	210	0.945	-	206.91
0.176	0.184	0.184	0.291	0.050	236	0.937	-	208.07
0.173	0.181	0.180	0.289	0.049	267	0.933	-	238.77
0.173	0.181	0.180	0.289	0.049	410	0.928	-	269.19
0.173	0.181	0.180	0.289	0.049	372	0.924	-	306.74
0.170	0.178	0.177	0.287	0.048	512	0.920	-	321.88
0.164	0.172	0.172	0.284	0.047	388	0.916	-	388.18
MSF - PW/ Haldar & Tang (1981)								
Modal	***Average***	***Fs-weighted***	***Max***	***PSHA-liq***	***N_{SPT}***	***C_N***	***k_σ***	***$(N_1)_{60}$***
0.215	0.225	0.224	0.348	0.060	52.000	0.951	0.839	49.432
0.186	0.194	0.194	0.300	0.051	25.000	0.917	0.971	22.932
0.184	0.193	0.192	0.302	0.051	31.000	0.918	0.961	28.464
0.189	0.198	0.197	0.309	0.052	40.000	0.931	0.938	37.224
0.187	0.196	0.195	0.306	0.052	35.000	0.924	0.948	32.335
0.179	0.188	0.187	0.297	0.050	21.000	0.894	0.971	18.776
0.173	0.182	0.182	0.294	0.048	24.000	0.884	0.968	21.210
Modal	***Average***	***Fs-weighted***	***Max***	***PSHA-liq***	***q_c (MPa)***	***C_q***	***k_σ***	***q_{c1N}***
0.215	0.225	0.224	0.348	0.060	28.800	0.996	0.955	322.010
0.186	0.194	0.194	0.300	0.051	34.800	1.010	1.000	377.604
0.184	0.193	0.192	0.302	0.051	21.900	0.976	0.940	258.041
0.189	0.198	0.197	0.309	0.052	13.300	0.943	0.926	178.666
0.187	0.196	0.195	0.306	0.052	9.600	0.914	0.939	125.744
0.179	0.188	0.187	0.297	0.050	28.000	0.991	0.882	309.414
0.173	0.182	0.182	0.294	0.048	27.800	0.990	0.957	307.812
Modal	***Average***	***Fs-weighted***	***Max***	***PSHA-liq***	***V_s (m/s)***	***C_v***	***k_σ***	***V_{S1} (m/s)***
0.180	0.189	0.188	0.292	0.050	210.000	0.945	-	206.907
0.180	0.189	0.188	0.292	0.050	236.000	0.937	-	208.070
0.177	0.186	0.185	0.290	0.049	267.000	0.933	-	238.770
0.177	0.186	0.185	0.290	0.049	410.000	0.928	-	269.191
0.177	0.186	0.185	0.290	0.049	372.000	0.924	-	306.735
0.174	0.182	0.182	0.288	0.048	512.000	0.920	-	321.880
0.168	0.177	0.176	0.285	0.047	388.000	0.916	-	388.176
MSF - PW/ Valera & Donovan (1977)								
Modal	***Average***	***Fs-weighted***	***Max***	***PSHA-liq***	***N_{SPT}***	***C_N***	***k_σ***	***$(N_1)_{60}$***

0.222	0.234	0.232	0.351	0.060	52	0.951	0.839	49.432
0.192	0.202	0.200	0.303	0.051	25	0.917	0.971	22.932
0.191	0.201	0.199	0.304	0.051	31	0.918	0.961	28.464
0.195	0.205	0.204	0.312	0.052	40	0.931	0.938	37.224
0.193	0.203	0.202	0.308	0.052	35	0.924	0.948	32.335
0.185	0.195	0.194	0.299	0.050	21	0.894	0.971	18.776
0.180	0.189	0.188	0.296	0.048	24	0.884	0.968	21.210
Modal	***Average***	***Fs-weighted***	***Max***	***PSHA-liq***	***q_c (MPa)***	***C_q***	***k_σ***	***q_{c1N}***
0.195	0.205	0.204	0.308	0.052	29	0.996	0.955	322.010
0.187	0.196	0.195	0.294	0.050	35	1.010	1.000	377.604
0.195	0.205	0.203	0.311	0.052	22	0.976	0.940	258.041
0.198	0.208	0.207	0.316	0.053	13	0.943	0.926	178.666
0.195	0.205	0.204	0.311	0.052	10	0.914	0.939	125.744
0.204	0.215	0.213	0.329	0.055	28	0.991	0.882	309.414
0.182	0.192	0.190	0.300	0.049	28	0.990	0.957	307.812
Modal	***Average***	***Fs-weighted***	***Max***	***PSHA-liq***	***V_s (m/s)***	***C_v***	***k_σ***	***V_{S1} (m/s)***
0.187	0.196	0.195	0.294	0.050	210	0.945	-	206.907
0.187	0.196	0.195	0.294	0.050	236	0.937	-	208.070
0.183	0.193	0.191	0.292	0.049	267	0.933	-	238.770
0.183	0.193	0.191	0.292	0.049	410	0.928	-	269.191
0.183	0.193	0.191	0.292	0.049	372	0.924	-	306.735
0.180	0.190	0.188	0.291	0.048	512	0.920	-	321.880
0.174	0.183	0.182	0.287	0.047	388	0.916	-	388.176

TABLE VI.5: PARAMETERS OF VERIFICATION WITH PARK & AHN (2003) MSF

MSF - P&A/ Seed et al. (1975)								
Modal	***Average***	***Fs-weighted***	***Max***	***PSHA-liq***	***N_{SPT}***	***C_N***	***k_σ***	***$(N_1)_{60}$***
0.119	0.124	0.126	0.326	0.060	52	0.951	0.839	49.432
0.103	0.107	0.109	0.282	0.051	25	0.917	0.971	22.932
0.102	0.106	0.108	0.283	0.051	31	0.918	0.961	28.464
0.104	0.109	0.111	0.290	0.052	40	0.931	0.938	37.224
0.103	0.108	0.109	0.287	0.052	35	0.924	0.948	32.335
0.099	0.104	0.105	0.279	0.050	21	0.894	0.971	18.776
0.096	0.101	0.102	0.276	0.048	24	0.884	0.968	21.210
Modal	***Average***	***Fs-weighted***	***Max***	***PSHA-liq***	***q_c (MPa)***	***C_q***	***k_σ***	***q_{c1N}***
0.104	0.109	0.110	0.287	0.052	29	0.996	0.955	322.01
0.100	0.104	0.105	0.274	0.050	35	1.010	1.000	377.60
0.104	0.109	0.110	0.289	0.052	22	0.976	0.940	258.04
0.106	0.110	0.112	0.294	0.053	13	0.943	0.926	178.67
0.104	0.109	0.110	0.290	0.052	10	0.914	0.939	125.74
0.109	0.114	0.116	0.307	0.055	28	0.991	0.882	309.41
0.097	0.102	0.103	0.279	0.049	28	0.990	0.957	307.81
Modal	***Average***	***Fs-weighted***	***Max***	***PSHA-liq***	***V_s (m/s)***	***C_v***	***k_σ***	***V_{S1} (m/s)***
0.100	0.104	0.105	0.274	0.050	210	0.945	-	206.91
0.100	0.104	0.105	0.274	0.050	236	0.937	-	208.07

0.098	0.102	0.104	0.272	0.049	267	0.933	-	238.77
0.098	0.102	0.104	0.272	0.049	410	0.928	-	269.19
0.098	0.102	0.104	0.272	0.049	372	0.924	-	306.74
0.096	0.101	0.102	0.271	0.048	512	0.920	-	321.88
0.093	0.097	0.099	0.267	0.047	388	0.916	-	388.18

MSF - P&A/ Haldar & Tang (1981)

Modal	***Average***	***Fs-weighted***	***Max***	***PSHA-liq***	N_{SPT}	C_N	k_σ	$(N_1)_{60}$
0.175	0.183	0.184	0.343	0.060	52.000	0.951	0.839	49.432
0.152	0.158	0.159	0.296	0.051	25.000	0.917	0.971	22.932
0.150	0.157	0.158	0.297	0.051	31.000	0.918	0.961	28.464
0.154	0.161	0.162	0.305	0.052	40.000	0.931	0.938	37.224
0.152	0.159	0.160	0.301	0.052	35.000	0.924	0.948	32.335
0.146	0.153	0.154	0.292	0.050	21.000	0.894	0.971	18.776
0.142	0.148	0.149	0.289	0.048	24.000	0.884	0.968	21.210
Modal	***Average***	***Fs-weighted***	***Max***	***PSHA-liq***	q_c (MPa)	C_q	k_σ	q_{c1N}
0.175	0.183	0.184	0.343	0.060	28.800	0.996	0.955	322.010
0.152	0.158	0.159	0.296	0.051	34.800	1.010	1.000	377.604
0.150	0.157	0.158	0.297	0.051	21.900	0.976	0.940	258.041
0.154	0.161	0.162	0.305	0.052	13.300	0.943	0.926	178.666
0.152	0.159	0.160	0.301	0.052	9.600	0.914	0.939	125.744
0.146	0.153	0.154	0.292	0.050	28.000	0.991	0.882	309.414
0.142	0.148	0.149	0.289	0.048	27.800	0.990	0.957	307.812
Modal	***Average***	***Fs-weighted***	***Max***	***PSHA-liq***	V_s (m/s)	C_v	k_σ	V_{S1} (m/s)
0.147	0.153	0.154	0.287	0.050	210.000	0.945	-	206.907
0.147	0.153	0.154	0.287	0.050	236.000	0.937	-	208.070
0.145	0.151	0.152	0.286	0.049	267.000	0.933	-	238.770
0.145	0.151	0.152	0.286	0.049	410.000	0.928	-	269.191
0.145	0.151	0.152	0.286	0.049	372.000	0.924	-	306.735
0.142	0.148	0.149	0.284	0.048	512.000	0.920	-	321.880
0.137	0.144	0.144	0.280	0.047	388.000	0.916	-	388.176

MSF - P&A/ Valera & Donovan (1977)

Modal	***Average***	***Fs-weighted***	***Max***	***PSHA-liq***	N_{SPT}	C_N	k_σ	$(N_1)_{60}$
0.163	0.171	0.173	0.334	0.060	52	0.951	0.839	49.432
0.141	0.148	0.149	0.288	0.051	25	0.917	0.971	22.932
0.140	0.147	0.148	0.290	0.051	31	0.918	0.961	28.464
0.143	0.150	0.152	0.297	0.052	40	0.931	0.938	37.224
0.141	0.149	0.150	0.293	0.052	35	0.924	0.948	32.335
0.136	0.143	0.144	0.285	0.050	21	0.894	0.971	18.776
0.131	0.139	0.140	0.282	0.048	24	0.884	0.968	21.210
Modal	***Average***	***Fs-weighted***	***Max***	***PSHA-liq***	q_c (MPa)	C_q	k_σ	q_{c1N}
0.143	0.150	0.152	0.293	0.052	29	0.996	0.955	322.010
0.137	0.143	0.145	0.280	0.050	35	1.010	1.000	377.604
0.143	0.150	0.152	0.296	0.052	22	0.976	0.940	258.041
0.145	0.152	0.154	0.300	0.053	13	0.943	0.926	178.666
0.143	0.150	0.152	0.296	0.052	10	0.914	0.939	125.744

0.149	0.157	0.159	0.313	0.055	28	0.991	0.882	309.414
0.133	0.140	0.142	0.285	0.049	28	0.990	0.957	307.812
Modal	***Average***	***Fs-weighted***	***Max***	***PSHA-liq***	***V_s (m/s)***	***C_v***	***k_σ***	***V_{S1} (m/s)***
0.137	0.143	0.145	0.280	0.050	210	0.945	-	206.907
0.137	0.143	0.145	0.280	0.050	236	0.937	-	208.070
0.134	0.141	0.143	0.278	0.049	267	0.933	-	238.770
0.134	0.141	0.143	0.278	0.049	410	0.928	-	269.191
0.134	0.141	0.143	0.278	0.049	372	0.924	-	306.735
0.132	0.139	0.140	0.277	0.048	512	0.920	-	321.880
0.127	0.134	0.136	0.273	0.047	388	0.916	-	388.176

Bibliography

Ambraseys N. (1988). Engineering seismology, Earthquake Engineering and Structural Dynamics, 17, 1-105.

Andrus R. D., Stokoe K.L. (1997). Liquefaction resistance based on shear wave velocity. Proc. NCEER Workshop on Evaluation of Liquefaction resistance of Soils. Nat. Ctr. For Earthquake Engrg. Res., State Univ. of NY, Buffalo, 89-128.

Andrus, R.D., Stokoe, K.H. (2000). Liquefaction resistance of soils from shear-wave velocity. Journal of Geotechnical and Geoenvironmental Engrg., ASCE, 126(11), 1015-1025.

Andrus, R.D., Stokoe, K.H., II, Chung, R.M., Juang, C.H. (2003) Guidelines for evaluating liquefaction resistance using shear wave velocity measurements and simplified procedures. NIST GCR 03-854, National Institute of Standards and Technology, Gaithersburg, MD.

Annaki M., Lee K. L. (1977). Equivalent uniform cycle concept for soil dynamics. Journal of the Geotechnical Engineering Division, ASCE; 103 (GT6): 549-564.

Arango I. (1996). "Magnitude scaling factors for soil liquefaction evaluations", Journal of Geotechnical Engineering, 122, 929-936.

ASTM-4015 (2003). Standard Test Methods for Modulus and Damping of Soils by the Resonant-Column Method.

Atkinson J.H. Bransby P.L. (1978). The mechanics of soils. Mc-Graw-Hill, London.

Aversa S., Vinale F. (1995). Improvement to a stress-path triaxial cell. Technical Note, ASTM Geotechnical Testing Journal. 116-120.

Been K. & Jefferies M. G. (1986). Discussion on a state parameter for sands. Geotechnique 36, No. 1, 127- 132.

Biondi G. (2002). Instabilità sismica dei pendii sabbiosi causata da incrementi di pressione interstiziale. PhD Thesis in Geotechnical Engineering, University of Catania, Italy.

Biondi G., Cascone E., Di Filippo G.(2012). Affidabilità di alcune correlazioni empiriche per la stime del numero di cicli di carico equivalente. Italian Geotechnical Journal; 2: 11-41.

Bishop A.W., Wesley L.D. (1975). A hydraulic triaxial apparatus for stress path testing. Geotechnique, 25,4, 657-670.

Casini F., Viggiani G.M.B. (2011). Evoluzione della granulometria di un materiale artificiale a grani frantumabili per diversi percorsi di sollecitazione. Incontro Annuale dei Ricercatori di Geotecnica 2011 - IARG 2011 Torino, 4-6 Luglio 2011.

Castro, G. (1975). Liquefaction and cyclic mobility of saturated sand. J. Geotech. Engng, ASCE 101, No. GT6, 551-569.

Castro G., Poulos, S. J. (1977). Factors affecting liquefaction and cyclic mobility. J. Geotech. Engng, ASCE 103, No. GT6, 501-516.

Cetin K.O. (2004). SPT-based probabilistic and deterministic assessment of seismic soil liquefaction potential. J. Geotech. Geoenvirom. Eng., 130,1314-1340.

Chiaradonna A., Tropeano G., d'Onofrio A., Silvestri F., Park D. (2015). Application of a simplified model for the prediction of pore pressure build-up in sandy soils subjected to seismic loading. 6th International Conference on Earthquake Geotechnical Engineering. 1-4 November 2015, Christchurch, New Zeland. (In press).

de Silva F., Ceroni F, Sica S, Pecce M R, Silvestri F. (2015). Effects of soil-foundation-structure interaction on the seismic behaviour of monumental towers: the case study of the Carmine Bell

Tower in Naples. Rivista Ital. di Geotecnica, special edition "Il ruolo della geotecnica nella salvaguardia dei monumenti e dei siti storici" (In press).

d'Onofrio A. (1996). Comportamento meccanico dell'argilla di Vallericca in condizioni lontane dalla rottura. PhD thesis, Consortium of Univerisity of Rome 'La Sapienza' and Naples 'Federico II'.

Evangelista L. (2006). Suscettibilità alla liquefazione dinamica dei depositi sabbiosi in falda della città di Napoli. Tesi di laurea, Università degli Studi di Napoli Federico II.

Finn W.D.L., Wightman A. (2007). Logical Evaluation of liquefaction potential using NBCC 2005 Probabilistic Ground Accelerations. Proc. IX Canadian Conference on Earthquake Engineering, Ottawa 1984-1993.

Ghionna, V. Porcino, D. (2006). Liquefaction Resistance of Undisturbed and Reconstituted Samples of a Natural Coarse Sand from Undrained Cyclic Triaxial Tests. J. Geotech. Geoenviron. Eng., 132(2), 194–202.

*Green RA, Terri GA. (2005). Number of equivalent cycles concept for liquefaction evaluations-Revisited. Journal of Geotechnical and Geoenvironmental Engineering, ASCE. **131** (4): 477-488.*

Gruppo di lavoro MPS (2004). Redazione della mappa di pericolosità sismica prevista dall'Ordinanza PCM 3274 del 20 marzo 2003. Rapporto conclusivo per il dipartimento di Protezione Civile, INGV, Milano – Roma, aprile 2004, 65 pp.

Haldar A., Tang W. H. (1981). Statistical study on uniform cycles in earthquake. Journal of Geotechnical Engineering Division, ASCE, 107, 577-589.

Hardin, B. O. and Drnevich, V. P. (1970). Shear Modulus and Damping in Soils: I.Measurement and Parameter Effects, Journal of Soil Mechanics and Foundation Division,ASCE, 98:6, 603-624.

Hight D.W. (1982). A simple piezometer probe for the routine measurement of pore pressure in triaxial tests on saturated soils. Geotechnique Vol. 32, No. 3,396-40.

Hyodo M., Hyde A. F. L., Aramaki N. Liquefaction of crushable soils (1998). Géotechnique, Volume 48, Issue 4, 01 August , pages 527 –543.

Idriss, I.M., Boulanger, R. W. (2004). Semi-Empirical Procedures for Evaluating Liquefaction Potential During Earthquake. Proceedings of the 11th ICSDEE & 3rd ICEGE, (Doolin et al. Eds.), Berkeley, CA, USA, 1, 32-56.

Iervolino I., Galasso C., Cosenza E., (2009). REXEL: computer aided record selection for code-based seismic structural analysis. Bulletin of Earthquake Engineering, 8, 339-362.

Ishihara K. (1996). Soil behavior in earthquake geotechnics. Claredon press.

Ishihara K., and Koseki J. (1989). Cyclic Shear Strength of Fines-Containing Sands. Earthquake and Geotechnical. Engrg., Japanese Society of Soil Mechanics and Foundation Engineering, Tokyo, 101-106.

Ishihara K., Tatsuoka, F. & Yasuda, S. (1975). Undrained deformation and liquefaction of sand under cyclic stress. Soils Fdns 15, No. 1, 29-44.

Kramer S.L. (1996). Geotechnical Earthquake Engineering, Prentice Hall Publishing, Upper Saddle River, NJ, 653pp.

Ladd R., Dobry R., Dutko P., Yokel F., Chung R. (1989). Pore-water pressure buildup in clean sands because of cyclic straining. Geotechnical Testing Journal;12(1):77–86.

L'amante D., Flora A., Russo G., Viggiani C. (2012). Displacements induced by the installation of diaphragm panels. Acta Geotech. 7:203-218.

Liao C., Whitman. R. V. (1986). Overburden correction factors for SPT in sand." Journal of Geotechnical Engineering, ASCE, 112(3), 373-377.

Mayne P.W. (1991). Tentative method for estimating r0 h0 from qc data in sands. In: Proceedings of the 1st international symposium on calibration chamber testing, Potsdam, NY, Elsevier, pp 249–256.

Mayne PW, Kulhawy FH (1982). K_0-OCR relationship in soil. J Geotech Eng Div Am Soc Civ Eng 106(6):851–872 13.

Marchetti S, Monaco P, Totani G, Calabrese M (2001). The DMT in soil investigations, a report by the ISSMGE committee TC16, p 41.

Matasovic N, Vucetic M. (1993). Cyclic characterization of liquefiable sands. Journal of Geotechnical Engineering, ASCE; 119 (11): 1805-1822.

Martin, G. R. (1975). Fundamentals of Liquefaction Under Cyclic Loading, J. Geotech., Div. ASCE, 101:5, 423-438.

Miner M. A. (1945). Cumulative damage in fatigue. Trans. ASME 67, A159-A164.

Miura N. & Yamanouchi T. (1971), "Drained shear characterisics of Toyoura sand under high confining stress." Proc. of Japanese Society of Civil Engineers. 260: 69-79.

Mominul H. M., Alam M.J., Ansary A., Karim E. (2013). Dynamic properties and liquefaction potential of a sandy soil containing silt. Proceedings of the 18th Conference on Soil Mechanics and Geotechnical Engineering, Paris

Mulilis J.P., Seed H.B., Chan C.K., Mitchell J.K. (1977). "The effects of method of sample preparation on the cyclic stress-strain behaviour of sands", Report no. EERC 75-18, Earthquake Engineering Research Center, University of California, Berkeley.

Nicotera M. V. (1998). Effetti del grado di saturazione sul comportamento mecccanico di una pozzolana del napoletano. PhD thesis.

Olivares L., Damiano E., Greco R., Zeni L., Picarelli L., Minardo A., Guida A., Bernini R (2009). An instrumented flume to investigate the mechanics of rainfall-induced landslides in unsaturated granular soils. Geotechnical Testing Journal, Vol. 32, No.2.

Olivares, L., Picarelli, L. 2001. Susceptibility of loose pyroclastic soils to static liquefaction: some preliminary data. Proc. Int. Conf. Landslides – Causes, Impacts and Countermeasures, Davos

Olsen R. S. (1997). Cyclic liquefaction based on the cone penetrometer test," Proc., NCEER Workshop on Evaluation of Liquefaction Resistance of Soils, National Center for Earthquake Engineering Research, State University of New York at Buffalo, Report No. NCEER-97-0022, 225-276.

Orense, R.P., Pender, M.J. and Tai, A. (2012). Undrained cyclic shear behaviour of pumice sand, Proc., Australia-New Zealand Conference on Geomechanics, 6pp.

Orense R, Hyodo M, Kaneko T. (2012). Dynamic deformation characteristics of pumice sand, New Zealand society for earthquake engineering (2012 NZSEE) conference. University of Canterbury; Christchurch, NZ.

Orense R. P., Pender M. J. (2013). Liquefaction characteristics of crushable pumice sand. Proceedings of the 18th international Conference on Soil Mechanicsand Geotechnical Egineering, Paris.

Palmgren A. (1924). Die lebensdauer von kugella geru. ZVDI, 68(14), 39-341.

Park T, Ahn JK. (2013). Accumulated stress based model for prediction of residual pore pressure. Proceedings of the 18th International Conference on Soil Mechanics and Geotechnical Engineering, Paris, France.

Penta F., Croce A., Esu F. (1961). Caratteristiche geotecniche dei terreni vulcanici. V Convegno Nazionale di geotecnica.

Phillips C., Hashash Y.M.A. (2009). Damping formulation for non linear 1D site response analyses. Soil Dynamics and Earthquake Engineerin; 29 (7): 1143-1158.

Polito C. P. (1999). The Effects Of Non-Plastic and Plastic Fines On The Liquefaction Of Sandy Soils. PhD Thesis.

Poulos, S. J., Castro, G. & France, J. W. (1985). Liquefaction evaluation procedure. J. Geotech. Engng, ASCE 111, No. GT6, 772-792.

Prakash S., Puri V. (2003). Liquefaction of silts and silt-clay mixtures. Us Taiwan Workshop.

Prakash S. and Puri V. K. (2010). Recent advances in liquefaction of fine grained soils, Fifth International Conference on Recent Advances in Geotechnical Earthquake Engineering and Soil Dynamics on May 24-29 2010, San Diego, California, Paper No 4.17a.

Prakash, S. and V.K. Puri. (2012). Developments in geotechnical earthquake engineering in recent years – 2012. Invitation Jai Krishna 100th Anniversary Volume, Oct-2012.

Robertson P. K., Wride C. E. (1997). Cyclic Liquefaction and its Evaluation Based on SPT and CPT," Proc., NCEER Workshop on Evaluation of Liquefaction Resistance of Soils, National Center for Earthquake Engineering Research, State University of New York at Buffalo, Technical Report No. NCEER-97-0022, December, pp 41 – 88.

Robertson P. K. and Cabal K. L. (2010). Guide to Cone Penetration Testing for Geotechnical Engineering. Gregg Drilling & Testing Inc., California, 4th Edition.

Rollins K, Evans M, Diehl N, Daily W. (1998). Shear modulus and damping relation- ships for gravels. Journal of Geotechnical and Environmental Engineering;124(5):396–405.

Rosi M., Sbrana A., (1987). The Plegrean Fields. CNR Quad. Ric. Sci., 114(9):1-175.

Santucci de Magristis F. (1992).Una cella triassiale a stress path controllato: messa a punto e primi risultati sperimentali. Degree Thesys. University of Naples "Federico II".

Santucci de Magristis F. (1996). Comportamento di un limo sabbioso ed argilloso costipato ed addizionato con bentonite. Phd Thesys. Consortium University of Rome "La Sapienza" and Naples "Federico II".

Seed H.B., Idriss M. (1971). Simplified procedure for evaluating soil liquefaction potential, J. Soil Mech. Found. Div., 97, 1249-1273.

Seed H.B., Idriss M., Makdisi F., Banerjee N. (1975). Representation of irregular stress time histories by equivalent uniform stress series in liquefaction analysis. Report EERC 75-29, Earthquake Engineering Research Center, University of California, Berkley.

Seed H. B., Mori K., Chan C. K. (1975a). Influence of Seismic History on the Liquefaction Characteristics of Sands. Report No. EERC 75-25, Earthquake Engineering Research Center, University of California, Berkeley, August.

Seed, H. B., Idriss, I. M. (1970). Soil Moduli and Damping Factores for Dynamic Response Analyses, Report EERC 70-10, Earthquake Engineering Research Center, University of California, Berkeley, CA.

Seed H.B., Idriss M. (1982). Ground motions and soil liquefaction during earthquakes, Earthquake Engineering Research Institute Monograph, Oakland, California.

Seed H.B. (1983). Earthquake resistant design of earth dams. Proc., Symposium on Seismic Design of Embankments and Caverns, Pennsylvania, ASCE, N.Y., pp. 41-64, 1983.

Seed R. B., Cetin K. O., Moss R. E. S., Kammerer A., Pestana J. Wu, J., Riemer M., Sancio R. B., Bray J. D., Kayen R. E., Faris A. (2003). Recent advances in soil liquefaction engineering: A unified and consistent framework." Keynote presentation, 26th Annual ASCE Los Angeles Geotechnical Spring Seminar, Long Beach, CA.

Seed, H.B., Martin, P.P., Lysmer, J. (1976). Pore-water pressure changes during soil liquefaction, J Geotech Engng Div, ASCE ;102:4, 323–46.

Senetakis K, (2011). Dynamic properties of granular soils and mixtures of typical sands and gravels with recycled synthetic materials. PhD dissertation. Department of civil engineering: Aristotle University of Thessaloniki; Greece.

Senetakis K., Anastasiadis A., Pitilakis K. (2012). The small-strain shear modulus and damping ratio of quartz and volcanic sands. Geotechnical Testing Journal; 35(6) (ISSN: 1945–7545).

Shibata T., Teparaksa W. (1988). Evaluation of liquefaction potentials of soils using cone penetration tests," Soils and Foundations, Tokyo, Japan, 28(2), pp 49-60

Silver M., Seed H. (1971). Volume changes in sands during cyclic loading. Journal of Soil Mechanics and Foundations, ASCE 97(9):1171–82.

Silvestri F. (1991). Analisi del comportamento dei terreni naturali in prove cicliche e dinamiche di taglio torsionale. PhD thesis.

Silvestri F. (2001). Looking for objective criteria in the interpretation of laboratory stress-strain tests. Pre-failure Deformation Characteristics of Geomaterials. Swets & Zeitlinger; 1305-1315.

Silvestri F., d' Onofrio A. (2014). RISPOSTA SISMICA E STABILITÀ DI CENTRI ABITATI E INFRASTRUTTURE. Relazione generale, XXV Convegno Nazionale di Geotecnica, Baveno.

Stark F. Olson S. M. (1995). Liquefaction Resistance Using CPT and Field Case Histories. Journal of Geotechnical Engineering, ASCE, 121(12), 856-869.

Sun, J. I., Golesorkhi, R. and Seed, H. B. (1988) "Dynamic Moduli and Damping Ratios for Cohesive Soils," Report No. UCB/EERC-88/15, Earthquake Engineering Research Center, University of California, Berkeley, 42p.

Suzuki Y., Koyamada K., Tokimatsu K. (1997). Prediction of Liquefaction Resistance Based on CPT Tip Resistance and Sleeve Friction," Proceedings, 14th International Conference on Soil Mechanics and Foundation Engineering, Hamburg, Germany, Vol. 1, pp 603 – 606.

Suzuki M., Yamamoto T. (2004). Liquefaction characteristic of undisturbed volcanic soil in cyclic triaxial tests. 13th World Conference on Earthquake Engineering Vancouver, B.C., Canada August 1-6, 2004 Paper No. 465.

Sze H. Y., Yang J. (2013). Cyclic loading behavior of saturated sand with different fabrics. Proceedings of the 18th international Conference on Soil Mechanicsand Geotechnical Egineering, Paris.

Tatsuoka, F., Toki, S., Miura, S., Kato, H., Okamoto, M., Yamada, S., Yasuda, S., and Tanizawa, F. (1986) Some Factors Affecting Cyclic Undrained Triaxial Strength of Sand,. Soils and Foundations, Vol. 26, No. 3, pp. 99-116.

Tatsuoka F. (1988). Some recent developments in triaxial testing system for choesionless soils. ASTM STP 977. (Donaghe, Chaney & Silver eds.) 6-67.

Toki S., Miura S., Yamashita S. (1986). Effect of pore pressure coefficient-B on undrained cyclic triaxial strength of saturated sand. Proceeding, 21st Japan National Conference on SMFE,vol. 1, pp. 565-568.

Tropeano G, Ausilio A Costanzo A. (2011). Non-linear coupled approach for the evaluation of seismic slope displacement. Proceedings of the 5th International Conference on Earthquake Geotechnical Engineering, Santiago, Chile.

Tsuchida H. (1970). Prediction and countermeasure against liquefaction in sand deposits. Abstract of the Seminar of the Port and Harbour Research Institute, Ministry of Transport, Yokosuka, Japan, 3, 1-33.

Vaid, Y. P. & Chern, J. C. (1985). Cyclic and monotonic undrained response of saturated sand. Advances in the Art of Testing Soils under Cyclic Conditions, ASCE Convention, Detroit, 120±147.

Vaid, Y. P., Chung, E. K. F. & Kuerbis, R. H. (1989). Preshearing and undrained response of sand. Soils Fdns 29, No. 1, 49±61.

Valera J.E., Donovan N.C. (1977). Soil liquefaction procedures- A review, Journal of Geotechnical Engineering Division, ASCE, 103, 607-625.

Vucetic M. Cyclic threshold shear strains in soils. (1994). Journal of Geotechnical Engineering, ASCE; 120 (12):2208–28.

Vucetic, M. and Dobry, R. (1991). Effect of Soil Plasticity on Cyclic Response, Journal of Geotechnical Engineering, ASCE, 117:1, 89-107.

Yamamoto, Y., Hyodo, M. & Orense, R. (2009). Liquefaction resistance of sandy soils under partially drained condition. Journal of Geotechnical and Geoenvironmental Engineering, ASCE, Vol. 135, No. 8, 1032-1043.

Youd LT. Compaction of sands by repeated shear straining. (1972). Journal of Soil Mechanics and Foundations, ASCE: 98(7): 709–25.

Youd T. L., Idriss I .M, Andrus R. D., Arango I., Castro G., Christian J. T, Dobry R., Finn W. D. L., Harder L. F. Jr, Hynes M. E., Ishihara K., Koester J. P., Liao S. S. C., Marcuson W. F III, Martin G. R., Mitchell J. K., Moriwaki Y., Power M. S., Robertson P. K., Seed R. B., Stokoe II K. H.(2001). Liquefaction resistance of soils: Summary report from the 1996 NCEER and 1998 NCEER/NSF workshops on evaluation of liquefaction resistance of soils. Journal of Geotechnical and Geoenvironmental Engineering 127 (10), 817–833.

Zhou (1980). Evaluation of the Liquefaction of Sand by Static Cone penetration Test. Proceedings, 7th World Conference on Earthquake Engineering, Istanbul, Turkey, Vol. 3.